

MASARYK UNIVERSITY
FACULTY OF SCIENCE

Ph.D. Dissertation

BRNO 2019

MILAN PRVÁK



MASARYK UNIVERSITY
FACULTY OF SCIENCE

DEPARTMENT OF THEORETICAL PHYSICS AND ASTROPHYSICS



The nature of the variability of chemically peculiar stars

Ph.D. Dissertation

Milan Prvák

Supervisor: Prof. Mgr. Jiří Krtička, Ph.D.

Brno 2019

Bibliographic Entry

Author: Milan Prvák
Faculty of Science, Masaryk University
Department of Theoretical Physics and Astrophysics

Title of Thesis: The nature of the variability of chemically peculiar stars

Degree Programme: Physics

Field of Study: Theoretical Physics and Astrophysics

Supervisor: Prof. Mgr. Jiří Krtička, Ph.D.
Faculty of Science, Masaryk University
Department of Theoretical Physics and Astrophysics

Academic Year: 2018/2019

Number of Pages: 115

Keywords: stars: chemically peculiar – stars: variables – stars: atmospheres

Bibliografický záznam

Autor:	Milan Prvák Přírodovědecká fakulta, Masarykova univerzita Ústav teoretické fyziky a astrofyziky
Název práce:	Příčiny proměnnosti chemicky pekuliárních hvězd
Studijní program:	Fyzika
Studijní obor:	Teoretická fyzika a astrofyzika
Vedoucí práce:	Prof. Mgr. Jiří Krtička, Ph.D. Přírodovědecká fakulta, Masarykova univerzita Ústav teoretické fyziky a astrofyziky
Akademický rok:	2018/2019
Počet stran:	115
Klíčová slova:	hvězdy: chemicky pekuliární – hvězdy: proměnné – hvězdy: atmosféry

Abstract

Context: Chemically peculiar (CP) stars are upper main sequence stars with spectra showing unusual features compared with other stars of comparable mass, age, and effective temperature. The current theory explains these phenomena by abnormal chemical composition of the surface layers of the stars. These stars commonly exhibit photometric and spectroscopic variability. This is usually described using the model of *oblique rotator* or the model of rigidly rotating magnetosphere. A lot of progress in the study of these stars has been made since they were first discovered. Methods have been developed to derive surface abundance distribution from spectroscopy and photometry. It is assumed that the internal structure of the CP stars does not differ from that of normal stars of comparable spectral class. The study of these relatively rare objects can therefore prove extremely useful in providing insight and in extending our understanding of the stellar physics.

Aims: In the present work we aim to provide a general overview of the current state of the CP stars research. We show several methods employed in the analysis of the CP stars to derive surface abundance structures, to model, explain, and interpret their photometric and spectroscopic variability, and to identify the process responsible for the unusual behaviour of these objects.

Methods: We employ the code INVERS12 to derive abundance maps of the star V824 Cen from the spectral line profile variations observed in high-dispersion spectroscopy. Using a grid of ATLAS12 and TLUSTY model atmospheres and SYNSPEC synthetic spectra, we predict photometric variability of the Ap star φ Dra and the HgMn star φ Phe. We also develop our own code to derive light intensity maps from observed photometric variability. We apply this code to explain the variability of several objects exhibiting CP star-like behavior.

Results: We give an illustratory example of usage of the Doppler imaging technique, deriving preliminary abundance maps of several elements of the star V824 Cen. The synthetic light curve of φ Dra in the visible part of the spectrum is in good agreement with the photometric observations of the star, whereas the predicted variability of φ Phe qualitatively matches the observed behavior. Our code succeeds in explaining the general character of the light variability of most of the studied objects, although some minor features cannot be satisfactorily described by rotation-modulated variability of a star with photospheric spots.

Conclusions: We conclude that the photometric changes of the star φ Dra are caused by spectral energy redistribution mainly due to bound–bound transitions of iron and bound–free transitions of silicon. The variability of φ Phe is caused by absorption on lines of yttrium and titanium. We show that the variability of the white dwarf GALEX J014636+323615 can be explained by inhomogeneous surface distribution of light intensity and rotation of the star. In case of the main-sequence star KIC 11560273 and the suspected subdwarf HD 144941, the model explains the general appearance of the light curve, but mechanisms other than the photospheric spots must be responsible for some minor features of the variability. Our code turns out to be a handy tool for explaining the photometric variability of CP stars, but doesn't compare to the reliability of the Doppler imaging in deriving the correct distribution of abundances in latitude.

Abstrakt

Kontext: Chemicky pekuliární (CP) hvězdy jsou hvězdy hlavní posloupnosti se spektry vykazujícími neobvyklé vlastnosti ve srovnání s ostatními hvězdami srovnatelné hmotnosti, věku a efektivní teploty. Současná teorie tyto jevy vysvětluje abnormálním chemickým složením jejich povrchových vrstev. Tyto hvězdy běžně vykazují fotometrickou a spektroskopickou proměnnost. Ta je většinou popisována modelem *skloněného rotátoru* nebo modelem pevně rotující magnetosféry. Studium těchto hvězd zaznamenalo od jejich objevení velký pokrok. Byly vyvinuty metody odvození povrchového rozložení abundancí ze spektroskopie i z fotometrie. Předpokládá se, že se vnitřní stavba CP hvězd neliší od běžných hvězd srovnatelné spektrální třídy. Studium těchto poměrně vzácných objektů proto může pomoci prohloubit naše porozumění hvězdné fyzice.

Cíle: V této práci se snažíme poskytnout obecný přehled o současném stavu výzkumu CP hvězd. Uvádíme několik metod používaných při rozboru CP hvězd k odvození abundančních obrazců, vysvětlení a výkladu jejich fotometrické a spektroskopické proměnnosti a určení jevů zodpovědných za jejich neobvyklé chování.

Metody: K odvození abundančních map hvězdy V824 Cen ze změn profilu čar pozorovaných ve spektroskopii s vysokou disperzí používáme program INVERS12. Pomocí sítě modelů atmosfér vytvořených programy ATLAS12 a TLUSTY a umělých spekter vytvořených programem SYN-SPEC předpovídáme fotometrickou proměnnost hvězdy typu Ap φ Dra a rtuťově manganové hvězdy φ Phe. Také vyvíjíme vlastní kód pro odvození rozložení intenzity světla z pozorované fotometrické proměnnosti. Tímto programem se snažíme vysvětlit proměnnost několika objektů vykazujících pekuliární chování.

Výsledky: Uvádíme ilustrační příklad použití metody dopplerovského mapování, jímž odvozujeme předběžné mapy povrchového rozložení několika prvků hvězdy V824 Cen. Umělá světelná křivka φ Dra se dobře shoduje s fotometrickými pozorováními, zatímco předpovězená proměnnost φ Phe vystihuje pozorované chování alespoň kvalitativně. Náš kód úspěšně vysvětluje obecnou povahu světelných změn většiny studovaných objektů, ačkoliv některé detaily proměnnosti nejsme schopni uspokojivě vysvětlit rotačně modulované proměnnosti hvězdy s fotosférickými skvrnami.

Závěry: Docházíme k závěru, že fotometrické změny hvězdy φ Dra jsou způsobeny přerozdělením energie ve spektru způsobeným zejména vázaně–vázanými přechody železa a vázaně–volnými přechody křemíku. Proměnnost φ Phe je způsobena absorbcí v čarách yttria a titanu. Ukazujeme, že proměnnost bílého trpaslíka GALEX J014636+323615 je možné vysvětlit nerovnoměrným povrchovým rozložením intenzity světla a rotací hvězdy. V případě hvězdy hlavní posloupnosti KIC 11560273 a pravděpodobného podtrpaslíka HD 144941 vysvětluje model v obecných rysech vzhled světelné křivky, avšak drobné detaily proměnnosti musejí být způsobeny jiným mechanismem než fotosférickými skvrnami. Ukazuje se, že náš program je užitečným nástrojem pro vysvětlení fotometrické proměnnosti CP hvězd, co do spolehlivosti určení šířek se ovšem nevyrovná dopplerovskému mapování.

Acknowledgements

I would like to thank my supervisor Prof. Mgr. Jiří Krtička for valuable advice and guidance throughout my Ph.D. studies, as well as Prof. RNDr. Zdeněk Mikulášek, CSc. for occasional comments and consultations. I am also very grateful to Dr. Theresa Lüftinger for teaching me the secrets of the Doppler imaging. Finally, I would like to thank anyone brave enough to read this work.

Contents

Introduction	xvii
Chapter 1. Stellar Atmospheres	1
1.1 Quantities describing the radiation field	1
1.2 Absorption and emission of radiation	2
1.3 Radiative transfer equation	3
1.4 Structural equations	4
1.5 Thermodynamic equilibrium	4
1.6 Local thermodynamic equilibrium	5
1.7 Non-LTE	5
1.8 Line profiles	6
1.9 Model atmospheres	7
Chapter 2. Chemically peculiar stars	9
2.1 History and classification	9
2.2 Properties of CP stars	11
2.2.1 Rotational velocities	12
2.2.2 Magnetic fields	12
2.2.3 Variability of CP stars	14
2.2.4 Causes of peculiarity	15
Chapter 3. Doppler Imaging	17
3.1 The oblique rotator	17
3.2 The inverse problem	19
3.3 V824 Cen	20
3.3.1 Fixing the stellar parameters	21
3.3.2 Mapping other lines	29
3.4 Conclusions	31
Chapter 4. Synthesizing light curves from abundance maps	35
4.1 φ Draconis	37
4.1.1 Abundance maps	38
4.1.2 The model	38
4.1.3 Influence of the chemical elements	40
4.1.4 Variability of φ Dra	42
4.1.5 Photometric observations	45
4.1.6 Comparison of the synthetic light curves with observations	47

4.1.7 Discussion	47
4.2 φ Phoenicis	49
4.2.1 Abundance maps	49
4.2.2 The model	51
4.2.3 Effect of chemical composition	51
4.2.4 Light variations of φ Phe	54
4.2.5 Comparison with observations	56
4.2.6 Discussion	57
4.3 Conclusions	57
Chapter 5. Obtaining brightness maps from photometry	59
5.1 Numeric solution	63
5.2 Testing the code	65
5.3 KIC 11560273	76
5.4 GALEX J014636+323615	76
5.5 HD 144941	76
5.6 Conclusions	79
Conclusions	81
References	83
List of publications	92
Appendix A. List of spectra used for abundance mapping of V824 Cen	95

Introduction

Decades ago, astronomers used to think the world of stars was relatively simple and consistent. The properties and structure of a star, as well as its evolution, was determined by its initial mass, chemical composition, and angular momentum. The stars would sit on the main sequence, nicely ordered by their effective temperature, their respective spectra forming a continuous sequence showing lines closely related to the corresponding spectral class.

The discovery and research of chemically peculiar (CP) stars opened for us a completely different picture of the stellar universe. A universe of great diversity, where no two stars are exactly like each other. We encounter chemical spots in the photospheres of the stars, varying greatly in shape and position. We find magnetic fields of various field strengths and geometries, stellar magnetospheres filled with particles of the stellar wind, forming fascinating structures co-rotating with stars. Chemically peculiar stars incessantly present us with new challenges, forcing us to come up with newer, more detailed models to describe their properties and variability. Our aim is to explain photometric variability, line profile variations, variable-strength emission lines, radio and X-ray emission, or alternating polarity of the observed magnetic field. Each time our observational techniques become more advanced, more accurate, the obtained measurements reward us with even more questions for our effort. Studying these fascinating objects, it does not seem like we are going to run out of questions any time soon. In the following chapters, we are going to discuss some of the problems currently encountered in the physics of CP stars. In Chapter 1, we will briefly list the basic equations and physical considerations necessary to describe the structure of the stellar photospheres and the state of the particles and radiation field. In Chapter 2, we will review the known properties of the CP stars, the history of their research, and the important discoveries in the field. In Chapter 3, we will discuss the problem of obtaining the surface distribution of chemical abundances from the line profile variations. We will give an example of using the Doppler imaging technique, which is currently a very popular and successful method of CP star surface analysis. In Chapter 4, we will show how the abundance maps obtained from spectroscopy can be used to reconstruct the photometric variability of CP stars. Finally, in Chapter 5, we will consider the possibility of deriving the surface distribution of light intensities from observed photometry. To this end, we will develop our own code, and we will test its reliability and usefulness on a couple of examples, both real and artificial.

Chapter 1

Stellar Atmospheres

Astronomy is one of the oldest natural sciences. Stars have drawn humans' attention since the most ancient times of our history, despite the fact that they are so distant and unreachable. Unlike other fields of science, astronomers cannot touch the object of their interest, place it in the laboratory and dissect it to see what it's made of. The only piece of information we have at our disposal when studying stars is the light that reaches us. As our observational capabilities improve, telescopes grow in size, as our understanding of theoretical and experimental physics advances, we can also reach a better and better understanding of the structure of the stars, and the physical phenomena that occur in them.

The vast majority of the light that we can observe comes from a relatively thin layer of the star, which we call the stellar atmosphere. The light radiated from the layers below the stellar atmosphere is typically absorbed or scattered away before it can reach us, whereas the layers above the atmosphere produce too little radiation to affect the nature of the observed electromagnetic spectrum significantly. For this reason, the significance of studying the stellar atmospheres is very high, even though they only constitute a relatively small fraction of the total mass of the star.

In the following text, we are going to give a brief description of the stellar atmospheres. For a more in-depth discussion, see e.g. Hubeny & Mihalas (2014); Jefferies (1968). The following text is based on the two books.

1.1 Quantities describing the radiation field

To describe the radiation at spatial coordinates \vec{r} and time t , travelling in the direction of a unit vector \vec{n} , into a solid angle $d\Omega$, in an interval of frequencies $(\nu, \nu + d\nu)$, we define specific intensity $I(\vec{r}, t, \vec{n}, \nu)$ in such a way that an amount of radiative energy $d\mathcal{E}$, passing through an oriented surface $d\vec{S}$ in a time interval dt is equal to

$$d\mathcal{E} = I(\vec{r}, t, \vec{n}, \nu) \vec{n} d\vec{S} d\Omega d\nu dt, \quad (1.1)$$

as seen in Fig 1.1. Unless necessary to avoid ambiguity, we will not explicitly mention the dependence on \vec{r} and t , and only denote the specific intensity by $I_\nu(\vec{n})$ in the following text. This quantity is extremely useful, especially because it is constant along a ray of the light, as long as there is no radiating or absorbing matter present along this ray.

By averaging the specific intensity over all solid angles, we can obtain Eddington's mean intensity:

$$J_\nu = \frac{1}{4\pi} \oint I_\nu(\vec{n}) d\Omega = \frac{1}{4\pi} \int_0^{2\pi} d\Phi \int_{-1}^1 I_\nu(\mu, \Phi) d\mu, \quad (1.2)$$

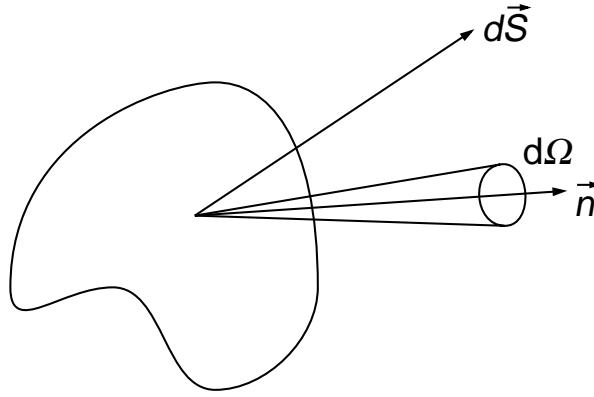


Figure 1.1: Specific intensity

where $\mu = \frac{\vec{n} \cdot d\vec{S}}{|d\vec{S}|}$ is the cosine of the angle between the direction of light propagation and the normal vector $d\vec{S}$.

Considering a small volume element dV , the energy of the radiation contained in this element coming from $d\Omega$ at frequency ν is

$$d\mathcal{E}_\nu = \frac{1}{c} I_\nu(\vec{n}) d\nu d\Omega dV, \quad (1.3)$$

where c is the speed of light. By integrating over the volume V and all the solid angles we can obtain the total energy in this volume:

$$d\mathcal{E}_\nu = \frac{1}{c} \int_V dV \oint I_\nu(\vec{n}) d\nu d\Omega. \quad (1.4)$$

If the volume in question is sufficiently small, so that the specific intensity does not depend on location, the integration over V and Ω can be performed separately, and we can get the *monochromatic radiation energy density* E_ν as

$$E_\nu = \frac{1}{c} \oint I_\nu(\vec{n}) d\Omega = \frac{4\pi}{c} J_\nu. \quad (1.5)$$

The rate of energy flow through a surface element $d\vec{S}$ can be expressed using the *monochromatic radiation flux* \vec{F}_ν . Integrated over any surface, it yields the net flow of radiative energy in the frequency interval $(\nu, \nu + d\nu)$ flowing through this surface per unit of time:

$$\vec{F}_\nu = \oint I_\nu(\vec{n}) \vec{n} d\Omega. \quad (1.6)$$

Sometimes, *Eddington flux* is also used, defined as

$$\vec{H}_\nu = \frac{\vec{F}_\nu}{4\pi}. \quad (1.7)$$

1.2 Absorption and emission of radiation

As the radiation spreads through the star, it interacts with the particles of stellar matter. The physical properties of this matter strongly affect the spectrum of the radiation ultimately emerging from the stellar surface by means of absorption, emission, and scattering of photons. Absorption is a

process, during which a photon is destroyed and its energy is transferred to the internal energy of the absorbing matter. For example, an atom is excited to a higher energy state (bound–bound transition) or, an atom can be ionized (photoionization, bound–free transition). The photon can also increase the kinetic energy of an electron in an electric field of an atom (free–free transition) which is then transferred to other particles through collisions. Photons can also be scattered, meaning an atom is ionized or excited by a photon, and consequently re-radiated in a (possibly) different direction. Light scattering on free electrons and Rayleigh scattering are also important processes. Let us define *absorption coefficient (opacity)* $\chi_\nu(\vec{n})$ in such a way, that a ray of radiation of intensity $I_\nu(\vec{n})$ and frequency interval $(\nu, \nu + d\nu)$, travelling in a direction \vec{n} into a solid angle $d\Omega$, incident on a small surface area $d\vec{S}$ of a volume element of thickness ds will lose energy dE after traversing through the element:

$$d\mathcal{E} = \chi_\nu(\vec{n}) I_\nu(\vec{n}) dS ds d\Omega d\nu dt. \quad (1.8)$$

This coefficient describes the effects of absorption and scattering by particles on the radiation field. The mean free path of a photon in the medium is then $1/\chi(\vec{r}, \vec{n}, \nu, t)$.

To all the absorption processes, there are also corresponding inverse processes; an excited atom transits into a lower state by emitting a photon, an atom recombines with an electron, and the excess energy is emitted in a form of a photon, an electron may lose some of its kinetic energy in an electric field of an atom and emit a photon, or a photon may be scattered into the line of sight. The energy emitted by a small volume element with a surface area $d\vec{S}$ and thickness ds in a direction \vec{n} into a solid angle $d\Omega$ in a time interval dt at frequency interval $(\nu, \nu + d\nu)$ is expressed using the *emission coefficient (emissivity)* $\eta_\nu(\vec{n})$ as follows:

$$d\mathcal{E} = \eta_\nu(\vec{n}) dS ds d\Omega d\nu dt. \quad (1.9)$$

For the purposes of the present work, we are going to only consider cases where the opacity χ_ν and emissivity η_ν do not depend on direction.

The emissivity and opacity at any specific frequency are given by the state of the matter contained in the considered volume and the nature and probabilities of the individual microscopical processes responsible for emission, absorption, and scattering of radiation. The actual values of absorption and emission coefficients, as well as the cross-sections, can be determined either experimentally or computed from quantum-mechanical considerations.

1.3 Radiative transfer equation

When a beam of radiation of intensity I_ν and frequency ν travels at point \vec{r} in a direction \vec{n} into a solid angle $d\Omega$ through and traverses a volume element of area dS and thickness $d\vec{r}$, some portion of energy will be removed from it due to absorption and out-scattering, while some amount of energy will be added to it due to emission by particles present in the volume. The net difference in specific intensity will then be

$$dI_\nu = (-\chi_\nu I_\nu(\vec{n}) + \eta_\nu) dr. \quad (1.10)$$

In the context of stellar atmospheres, it is reasonable to assume that the intensity of the radiation, as well as other quantities describing the problem, are symmetric around the normal to the stellar surface. Therefore, the specific intensity does not depend on the azimuthal angle Φ and is only a function of the angle θ between the normal to the stellar surface and the direction \vec{n} of propagation of radiation, or, more conveniently, its cosine $\mu = \cos \theta$. For a plane-parallel atmosphere, introducing a spatial coordinate $dz = -dr/\mu$, where dr is an infinitesimal length element along the direction of the light propagation, in such a way that it is zero at the top of the atmosphere, we can write the

equation of radiative transfer in the following way:

$$\mu \frac{dI_\nu}{dz} = \chi_\nu I_\nu - \eta_\nu. \quad (1.11)$$

It is customary (and convenient) to define *optical depth* as

$$\tau_\nu(z) = \int_0^z \chi_\nu dz'. \quad (1.12)$$

This allows us to write the equation of transfer in the form

$$\mu \frac{dI_\nu}{d\tau_\nu} = I_\nu - S_\nu, \quad (1.13)$$

where $S_\nu = \eta_\nu/\chi_\nu$ is the *source function*.

1.4 Structural equations

In the static case, the photosphere is assumed to be in a state of radiative equilibrium. That means that the energy emitted by any volume element in a specific time interval is equal to the amount of energy absorbed by this volume. In an environment without convection, we can write:

$$\int_0^\infty (\eta_\nu - \chi_\nu J_\nu) d\nu = 0.$$

A state of hydrostatic equilibrium is also assumed. This means that the net force acting on each volume element is zero; the atmosphere does not expand or collapse:

$$dp/dz = -f_z + \rho g,$$

where f_z is the z component of the radiative force density acting on the volume element.

1.5 Thermodynamic equilibrium

Any system contained in a fixed volume and isolated from the external environment will, due to the interactions of its particles, eventually evolve into a state of thermodynamic equilibrium. It is the most probable macrostate, the state with the highest entropy, and all processes occurring in the system are balanced by the corresponding inverse processes.

Photons are bosons, so they obey Bose–Einstein statistics. The spectral distribution of electromagnetic radiation in a state of thermodynamic equilibrium is therefore given by the Planck function

$$B_\nu(T) = \frac{2h\nu^3}{c^2} \frac{1}{e^{\frac{h\nu}{kT}} - 1}, \quad (1.14)$$

where T is the temperature, h is Planck's constant and k is Boltzmann's constant. The distribution of atoms, ions and electrons, on the other hand, follows Maxwellian distribution

$$f(v)dv = (m/2\pi kT)^{3/2} e^{-\frac{mv^2}{2kT}} 4\pi v^2 dv. \quad (1.15)$$

Excitation state of the matter is governed by the Boltzmann's excitation equation, so the ration between the population n_i of level i and the population n_0 of the ground state is

$$\frac{n_i}{n_0} = \frac{g_i}{g_0} e^{-\frac{\epsilon_i}{kT}}, \quad (1.16)$$

where g_i and g_0 are the corresponding statistical weights of the two states and \mathcal{E}_i is the excitation energy of the state i . Similarly, the ionization state is described by Saha's ionization equation. The ratio between number of j and $j+1$ times ionized atoms, n_j and n_{j+1} is

$$\frac{n_j}{n_{j+1}} = n_e \frac{U_j(T)}{U_{j+1}(T)} C_1 T^{-3/2} e^{-\frac{\mathcal{E}_j}{kT}}, \quad (1.17)$$

where \mathcal{E}_j is the ionization energy, $C_1 = \frac{1}{2} \left(\frac{h^2}{2\pi m_e k} \right)^{3/2}$ and U_j and U_{j+1} are the *partition functions* corresponding to ionization levels i and j .

1.6 Local thermodynamic equilibrium

In the physical conditions inside stars, the matter is not in the state of thermodynamic equilibrium. Energy flows from the stellar core outwards, the radiation field is anisotropic, the temperature gradient is non zero. Under some circumstances, we can afford to assume that the temperature and pressure are high enough for the frequent collisions between particles to keep the distribution of particles close to equilibrium, so that the physical conditions can be considered constant on the scale of the mean path of photons and the idealized model of thermodynamic equilibrium assuming a local value of temperature at each individual point in space gives a reasonably good description of the system. The distribution of velocities, ionization, and excitation states still obey the Maxwell, Saha, and Boltzmann equations. However, due to the non-zero temperature gradient, the radiation, flowing through a certain point in the atmosphere, originating at a different point with slightly different temperature, is therefore not in perfect equilibrium and its distribution can no longer be satisfactorily described by the Planck function. It has to be derived from the equation of transfer, typically under the assumption that the source function $S_\nu = B_\nu$. This description is generally referred to as the *local thermodynamic equilibrium (LTE)*. This assumption holds quite well in the stellar interiors, but not so well in stellar atmospheres, where particles are sparse, there is a significant temperature, pressure and density gradient, the radiation field is strongly anisotropic, and photons and particles can escape from the system at the surface of the star. On the other hand, the computational complexity and costs of solving the system of equations for the general non-equilibrium case is relatively high, forcing us to seek various approximations and simplifications when modelling stellar atmospheres.

1.7 Non-LTE

The term *non-LTE (NLTE)* refers to situations, where the LTE approximation cannot be used. It is a more correct and precise solution compared to LTE but is also significantly more computation-expensive. In NLTE the Maxwell distribution for particles is still assumed, but the population of ionization and excitation states no longer obeys Saha and Boltzmann equations. Instead, a system of equations of statistical equilibrium has to be solved. We assume the macroscopic state of the system to be constant, i.e., the populations of the energy levels do not evolve with time, but the detailed balance (that is, each process being exactly balanced by a counter-process) no longer holds. For each state $l, l = 1, \dots, NL$, the total rate of the collisional transitions C_{lu} and radiative transitions R_{lu} from the state l to all possible other states u is equal to the sum of all collisional transition rates C_{ul} and radiative transition rates R_{ul} from all the other states u to the state l .

$$n_l \sum_u (R_{lu} + C_{lu}) - \sum_u n_u (R_{ul} + C_{ul}) = 0, \quad (1.18)$$

where n_l and n_u are the number of particles in states l and u , respectively. This system needs to be added one more equation to be complete, for example the expression for the total number of particles:

$$\sum_k \sum_j N_{jk} = N_N.$$

The radiation in case of NLTE is solved through the equation of transfer, assuming a general, frequency-dependent source function S_ν .

1.8 Line profiles

Because the stellar atmosphere is not in perfect thermodynamic equilibrium, the light emitted in hotter layers of the atmosphere passes through colder layers (through matter with lower S_ν) before it escapes the star and reaches the observer. That results in the presence of dark absorption lines in the observed spectrum. Each such line corresponds to a single bound-bound transition (radiative excitation) of one of the many kinds of atoms (or molecules) present in the stellar atmospheres. Analogically, in cases where radiation emitted in colder environment passes through hotter material (higher S_ν), or when radiation from a hot source is in-scattered into the line of sight in colder, non-emitting material (e.g., in the circumstellar matter), we can observe bright emission spectral lines. Each such line is associated with a specific frequency ν corresponding to the difference between the energy E_u of the upper state and E_l of the lower state of the transition through the Planck–Einstein relation $h\nu_0 = E_u - E_l$. However, the observed spectral lines have a non-zero width, and the shape of the line profile is determined by many factors.

Natural width of the line profile follows from the Heisenberg's uncertainty principle due to the finite life-time Δt of the excited state:

$$\Delta E \Delta t \approx h/2\pi,$$

where $h \doteq 6.62607 \times 10^{-34} \text{ m}^2 \text{ kg s}^{-1}$ is the Planck constant. The frequency of the emitted or absorbed radiation can be further affected by the presence of nearby particles. This perturbation results in the *pressure (collisional) broadening*. The natural and pressure broadening both cause a Lorentz shape of the spectral line:

$$\Delta I(\nu) \propto \frac{\delta/\pi}{(\nu - \nu_0)^2 + \delta^2},$$

where ν_0 is the central frequency of the line and δ is the damping constant.

Thermal Doppler broadening of a line is broadening due to the random thermal motion of particles. The frequency of radiation absorbed or emitted by an atom moving with a radial velocity u relative to the observer is then shifted due to the Doppler effect:

$$\nu = \nu_0 \left(1 - \frac{u}{c}\right).$$

Assuming Maxwell distribution for the velocities of particles, the probability distribution $W(u)$ of radial velocity of the particle is determined by the Gaussian function:

$$W(u) = \frac{1}{u_0 \sqrt{\pi}} e^{-(u/u_0)^2},$$

where $u_0 = \sqrt{2kT/m}$ is the most probable velocity.

Convoluting the Lorentz and the Gauss functions, we combine the influence of the pressure and thermal broadening together, obtaining a Voigt profile:

$$\Delta I(\nu) \propto \frac{a}{\pi} \int_{-\infty}^{\infty} \frac{e^{-y^2} dy}{(x-y)^2 + a^2}, \quad (1.19)$$

where $a = \frac{\delta c}{u_0 \nu_0}$.

Rotation of the star also causes broadening of the spectral lines due to the Doppler effect, because different parts of the stellar disc move with different radial velocities relative to the observer. The resulting line profile is then given by integrating the local line profiles across the stellar disc, taking into account the respective local radial velocities and limb darkening. This problem will be discussed in more detail in later chapters.

1.9 Model atmospheres

Because the real situation in the stellar atmospheres is a complex problem to which an analytical solution cannot be found, it is usually solved numerically. That means the problem needs to be discretized. The photosphere is subdivided into small intervals; the radiation spectrum is discretized in both the frequency and direction. The model of the photosphere is typically one-dimensional. As for the geometry of the problem, there are two common approximations: plane parallel atmospheres and spherically symmetric atmospheres. In both cases, the quantities describing the particles depend only on one dimension, z or r , whereas the radiation field is a function of one spatial coordinate and the angle between z or r -axis and the direction of light propagation.

A model atmosphere usually depends on a few input parameters, such as mass M of the star, the effective temperature T_{eff} , the surface gravity $\log g$, macro- and microturbulent velocities and the chemical composition of the photosphere. The output of the model is a set of quantities describing the state of the stellar matter, such as the temperature, density, electron density, pressure, and level populations as functions of the position in the photosphere (typically expressed in terms of spatial coordinate, optical depth, or mass column density) and direction. The model atmospheres are usually used as a basis for computing synthetic spectra.

There are two different approaches to handle line opacities. First is the opacity sampling (OS), which solves the equation of transfer for several chosen wavelengths in the spectrum. The other approach is based on the opacity distribution functions (ODF), which involves rearranging the spectra in the order of the opacity values in order to get smoother, simpler functions, which can then be approximated by a smaller number of points.

Currently there are several model atmosphere codes available. ATLAS (Kurucz 1996) is an LTE model atmospheres program. Version 9 of the code was based on the ODF method, while the later ATLAS12 uses the OS technique (Castelli 2005). LLModels is an LTE code, taking into account vertical stratification of elements and the effects of magnetic field, which is significant for field strengths higher than 10 kG (Khan & Shulyak 2007). TLUSTY (Lanz & Hubeny 2007) is a plane-parallel atmosphere code supporting both the LTE and NLTE computations. PoWR (Gräfener et al. 2002) is an NLTE code for expanding atmospheres. ATA (Kubát 2003) is a plane-parallel or spherically symmetric code capable of producing NLTE models of stellar photospheres.

Chapter 2

Chemically peculiar stars

2.1 History and classification

Since the dawn of stellar spectroscopy, astronomers occasionally encountered stars, whose spectra could not quite fit the standard classification scheme. For example, Maury & Pickering (1897), conducting a spectral classification of stars, noticed the star α^2 CVn, noting its extremely faint line K, and unusually strong lines 4181.4 Å and 4128.5 Å, attributing this phenomenon to the known duplicity of the star.

Belopolsky (1913) discovered periodic variability of the spectral lines of Si II in the same star, corresponding to the period of radial velocity variations. He explained this behavior by rotation of the star and inhomogeneous surface distribution of the element. Guthnick & Prager (1914) discovered photometric variability with the same period.

Morgan (1933) noticed a correlation between the predominant type of the peculiarity and the effective surface temperature of the star. He defined five distinct types of chemically peculiar (CP) stars:

- manganese stars, corresponding to the spectral classes B8–A0,
- stars with strong line λ 4200 (B9–A0),
- europium stars (B9–F0),
- chromium stars (A0–F0),
- strontium stars (A2–F0).

Titus & Morgan (1940), performing a spectral classification of the Hyades cluster, noticed a group of six stars, showing a systematic shift in the relation between the luminosity class and spectral features. Trying to determine the spectral class from the strength of the Ca II K line, the stars would be A class. However, the metallic lines were too strong for an A star; their strength corresponded to F class stars. These stars became prototypes of what was later referred to as Am and Fm stars. In these stars, we usually find high overabundances of iron peak elements, rare-earth elements, lead, and zirconium, as well as deficiencies of carbon, nitrogen, oxygen, calcium, and scandium (Smith 1996).

Morgan et al. (1943) describes the spectrum of the star λ Boo, the first star of a class of peculiar objects typical by a decreased surface abundance of refractory elements by one to two dex, a weak line Mg 4481 Å, while the abundance of carbon, nitrogen, oxygen, and sulfur is approximately solar (Gray 1988). λ Boo stars cover the spectral ranges from late B to early F. The abnormalities

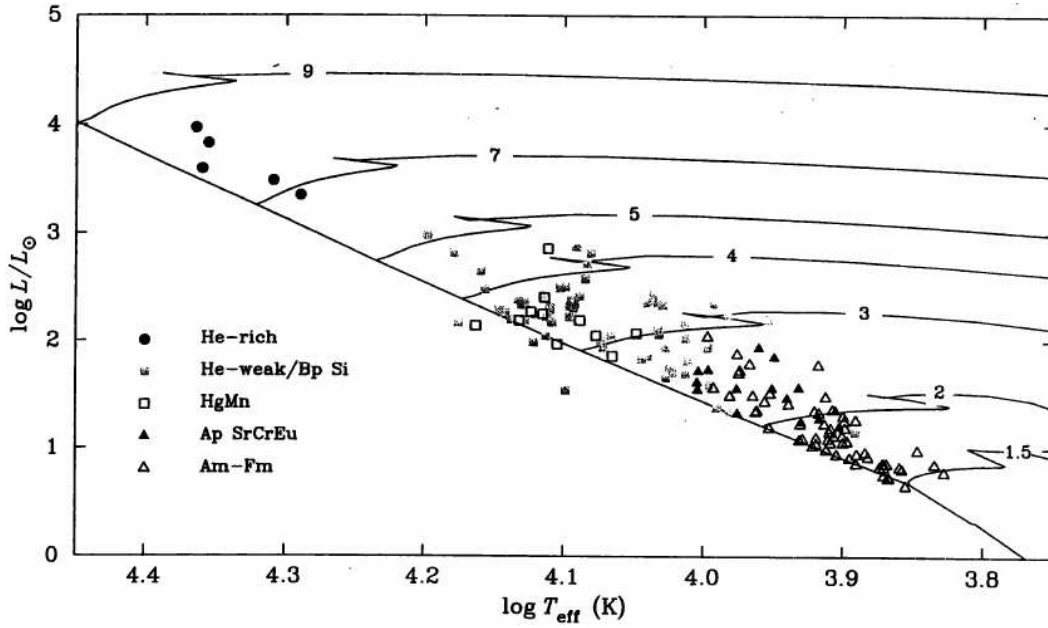


Figure 2.1: Position of CP stars found in open clusters in Hertzsprung–Russel diagram. Black symbols denote magnetic stars; open symbols denote non-magnetic stars. Solid lines show evolutionary tracks corresponding to stars with solar composition and different masses. Figure taken from Smith (1996) is based on data from North (1993), and the evolutionary tracks are taken from Schaller et al. (1992).

encountered in these stars are currently believed to be caused by the accretion of matter, either from interstellar medium (Kamp & Paunzen 2002) or from a circumstellar disc (Venn & Lambert 1990).

Babcock (1947) discovered a global dipolar magnetic field in the star 78 Virginis via measuring the Zeeman effect using a differential circular analyzer. That was the first discovery of a magnetic field in a star other than the Sun and a breakthrough in the physics of (not only) the upper main sequence stars.

The star Maia (20 Tauri) has also been noted for its unusual spectrum. The spectral lines are very sharp, meaning the star is either a very slow rotator or is seen pole-on (Struve 1945). Moreover, the Mg II 4481 Å line is quite weak, corresponding to a B3 or a B5 star. On the other hand, He I lines are also weak (hence the stars exhibiting similar spectral features are called helium-weak), more typical of a late B class. The strong Fe II lines imply even lower temperature (Struve 1951). Struve (1945) explains these features by fast-rotation of the star seen pole-on, with very different effective temperatures around the poles and the equator. However, this idea was later disputed by, e.g., Sargent & Searle (1966) and Hardorp & Scholz (1971), arguing that the weakening of the He I 4471 Å line due to gravitational darkening, that is typical for fast-rotating stars, would have to be significantly stronger to be consistent with the hypothesis of fast rotation. Abundance analyses performed by Molnar (1972), Vilhu et al. (1976), Mon et al. (1981), and others generally found decreased abundance of helium.

A discovery of unusually strong helium lines in the star σ Ori E (Greenstein & Wallerstein 1958) added a new type of peculiar objects to the list – the He-rich stars. Osmer & Peterson (1974) investigated spectra of several He-rich stars to estimate their evolutionary status. Arguing that these stars' surface gravity corresponds to main sequence stars, and that they are typically found near the galactic plane, they concluded that these stars are relatively young objects with a high abundance of helium and a normal abundance of C, Mg, Si, and Al. Plotting the surface gravity

versus effective temperature, they recognized the He-rich stars as a high-temperature extension of the Bp phenomenon.

As astronomy and its observational capabilities advanced, the number of newly found peculiar objects increased as well as their variety and diversity. Jaschek & Jaschek (1958) divided CP stars into 6 groups: λ 4200-Si, Mn, Si, SiCrEu, EuCrSr, and Sr. However, there was considerable overlap between the classes. Osawa (1965) went even further – he introduced 16 subclasses to classify the CP stars. The classification of CP stars was therefore later revised by Preston (1974). An improved scheme was devised, based on the chemical nature of the peculiarities, rather than merely superficial spectral features.

- *CP1 stars*, or Am stars, are metallic stars, with weak lines of Ca and enhanced lines of heavy metals. Typical temperatures range between 7 000 and 10 000 K.
- *CP2*, or magnetic Ap stars generally feature enhanced abundances of elements such as Si, Cr, Sr, or Eu. Typical temperatures are 8 000–15 000 K. These stars also usually have relatively strong magnetic fields – 10^3 – 10^4 G (Babcock 1958), which show periodic variations.
- *CP3*, or HgMn stars feature a strong Hg II λ 3984 line and significant lines of Mn II. Typical temperatures range from 10 000 to 15 000 K.
- *CP4 (He-weak)* stars are stars with temperatures 13 000–20 000 K. The He I lines in these stars are unusually weak for the spectral class inferred from photometry (Jaschek et al. 1969). They can be thought of as a high-temperature extension of the Ap and Bp stars (Ciatti et al. 1978).

Maitzen (1984) proposed an extension of the Preston system, classifying only the magnetic He-weak stars as CP4, while the non-magnetic CP4 stars would be referred to as CP5, the magnetic He-strong stars as CP6 and the non-magnetic ones as CP7, thus forming two alternating series, the odd classes CP1, CP3, CP5, and CP7 being the non-magnetic CP stars, in the order of increasing effective temperature, and the even classes CP2, CP4, and CP6 being the magnetic peculiar stars.

Fig. 2.1 shows the position of some CP stars found in open clusters in the Hertzsprung–Russell diagram. Kodaira (1969) noticed flux depressions at wavelengths 4200, 5200, and 6300 Å in the spectrum of the star HD 221568 caused by line blanketing effect by absorption lines of silicon, iron, and chromium. Maitzen (1976) proposed to use this phenomenon as a measure to quantitatively express the degree of the peculiarity of a star. To achieve this, he defined a new photometric index, $\Delta a = a - a_0$, where $a = g_2 - (g_1 + y)/2$, where y is the Strömgren y filter, g_1 and g_2 are two specific intermediate photometric filters and a_0 is the value of a for a non-peculiar of a corresponding $b - y$ color index. That is a very useful tool because it allows us to identify peculiar stars from photometric measurements, rather than requiring the detailed spectroscopy.

2.2 Properties of CP stars

Chemically peculiar stars comprise a significant part of the upper main sequence. Some authors estimate that up to about 25 % of stars ranging from spectral classes B2 to F4 are peculiar, the highest frequency being the spectral class A6, where the ratio of peculiar stars reaches over 50 % (Smith 1996).

Am (frequency 55 %) and HgMn stars (frequency 23 %) occur in spectroscopic binaries significantly more often than non-peculiar stars. Ap and Bp stars, on the other hand, are found in binary systems much less often (frequency 15 %, Seggewiss 1993).

The immediate cause of the peculiarity of CP stars is the abnormal chemical composition of the stellar atmosphere. The chemical abundances can differ from the solar composition by as much as 6 dex (Preston 1974). This abnormality, however, only affects a thin surface layer of the star. It is assumed that the mean, overall chemical composition of these stars is normal. There are several arguments to support this statement. First, the chemically peculiar stars are frequently found in close binaries or stellar clusters accompanied by stars with standard composition. It would be hard to justify a claim that the stars of common origin would have such a vastly different chemical composition. Also, if the overall composition of CP stars were different from normal stars, it would be very difficult to explain the correlation between effective temperature of the star and the type of the peculiarity (Sargent & Searle 1967). Moreover, if the internal parts of the stars had the peculiar composition, they would have to lie above the main sequence in the Hertzsprung–Russell diagram (Schwarzschild 1958), which is not observed (Sargent & Strittmatter 1966). That is a very important fact. It means that any general conclusions about the stellar physics that we draw from studying the chemically peculiar stars are also valid for normal stars. The vertical stratification of the chemical elements in the photosphere was also studied in detail (see e.g., Nesvacil et al. 2013; Khalack & LeBlanc 2015; Ndiaye et al. 2018).

2.2.1 Rotational velocities

CP stars tend to have relatively low rotational velocities compared to normal stars. On the other hand, there are very few slow rotators, amongst the A stars, which are not peculiar (e.g., Wolff & Wolff 1974; Smith 1996). In some cases the rotational period can be extremely long, e.g. the star HD 94660 (2700 days, Bailey et al. 2015), HD 18078 (1360 days, Mathys et al. 2016), or HD 50169 (29 years Mathys et al. 2019). Assuming that the rotational axes are distributed randomly in space, it seems there is very little overlap between the distribution of rotational velocities of peculiar and non-peculiar A stars, implying that the slow rotation is a condition not only necessary but also sufficient for the development of the chemical peculiarity in these stars (Abt & Morrell 1995). The same conclusion cannot be made about B stars, though, since there are known slow-rotating non-peculiar stars (Wolff & Preston 1978). The rotational velocities in He-rich and λ Boo stars seem to correspond to the rotational velocities of normal stars. In some of the CP stars, the rotational period has been shown to gradually decrease due to magnetic rotational braking (see, e.g., Ud-Doula et al. 2009). An extreme example of this effect is the star σ Ori E (Townsend et al. 2010). Possibly periodic changes in the rotational period on a time scale of decades have also been observed in some CP stars, such as the stars CU Vir or HD 37776 (Mikulášek et al. 2008b, 2011).

2.2.2 Magnetic fields

While not all CP stars possess a measurable magnetic field, all A and B stars with an observed magnetic field are peculiar (Landstreet 1982). The magnetic fields of CP stars are usually global, stable, and are close to dipolar. The strength of the magnetic field is typically in the order of 10^2 Gauss, but in some cases, it may be as high as 10^4 Gauss. The intermediate-mass stars seem to show a sort of a dichotomy; practically all of them either have quite strong magnetic fields (more than 300 Gauss) or no magnetic field whatsoever (Aurière et al. 2007), although this has been disputed by Fossati et al. (2015). A very weak magnetic field has also been detected in Vega, Sirius (Lignières et al. 2009; Petit et al. 2011; Braithwaite 2014), ρ Pup (Neiner et al. 2017), β UMa and θ Leo (Blazère et al. 2016b), and Alhena (Blazère et al. 2016a). The observed longitudinal component usually exhibits roughly sinusoidal variations with the period corresponding to the rotational period of the star. These changes have been explained by the model of the *oblique rotator* by Stibbs (1950). According to the model, a stable, dipolar magnetic field, tilted by some

fixed angle relative to the rotational axis is “frozen” into the surface of the star and rotates together with the star, causing the apparent changes of the magnetic field intensity projection.

Magnetic fields (as well as surface chemical peculiarities) have also been observed in pre-main sequence Ae / Be Herbig stars (see e.g., Bychkov et al. 2013; Alecian et al. 2013; Netopil et al. 2014), suggesting that these stars are the progenitors of the magnetic Ap / Bp stars (Alecian et al. 2009).

The strongest magnetic fields are typically observed in He-rich stars (Landstreet & Borra 1978). Often there is an area around the star, where the centrifugal force in the co-rotating frame of reference is greater than the gravitational force, while, at the same time, the magnetic field is still strong enough to prevent the electrically charged particles of the stellar wind from moving freely in directions other than along the magnetic field lines. The effective potential, determined by the gravitational, centrifugal, and magnetic forces on the particles along each individual field line, has a local minimum at some point above the surface of the star. That means the electrically charged plasma of the stellar wind emerging from the stellar surface can settle in a stationary state inside these potential minima, forming a thin disc-like structure around the star, co-rotating with the star as a rigid body (Landstreet & Borra 1978; Nakajima 1985; Smith & Groote 2001). The shape of this disc depends on the angle between the magnetic axis relative to the rotational axis, and also on the geometry of the magnetic field of the star, which usually differs somewhat from an ideal dipole. The rotation of the system leads to periodic occultations of the star by the circumstellar matter, resulting in an observed photometric variability with several sharp, narrow minima. The corresponding light curves often closely resemble eclipsing binaries. This model of a rigidly-rotating magnetosphere (RRM) was introduced by Townsend & Owocki (2005) to explain photometric variations of the star σ Ori E. While this model succeeds in predicting the two photometric minima observed in the star, it fails in explaining the light variations at some other rotational phases. The variability of the star was later assumed to be a combination of the effects of the RRM variability and photospheric spots. Abundance maps were therefore obtained using the magnetic Doppler imaging by Oksala et al. (2012, 2015). Generalizing the model to allow arbitrary (i.e., non-dipolar) magnetic field geometry, new models were made. Nevertheless, a satisfactory agreement with the observations was still not achieved. The authors attributed the discrepancy to scattering by the circumstellar matter, which was not taken into account in their model. Radio emission was also observed in some Bp stars (see e.g., George & Stevens 2012; Leto et al. 2017a, 2018). This phenomenon is usually explained by gyrosynchrotron emission (Drake et al. 1987). Similarly, X-ray emission was detected (Robrade 2016; Robrade et al. 2018). It is assumed to be caused by impacts of fast electrons in the magnetosphere into the photosphere of the star (Leto et al. 2017b).

The exact origin of the magnetic field is still not completely understood (Mestel 2003). Some authors favor a concept of “fossil” magnetic fields. According to this hypothesis, the star’s magnetic field is a remnant from an earlier stage of its evolution, “frozen” into the stellar plasma. It may have originated either in the interstellar matter in which the star once formed (“*strong fossil field hypothesis*”, Mestel 1966). Alternatively, the magnetic field may have been formed by a dynamo during a pre-main sequence stage or by a merger involving a star with a radiative envelope later on (“*weak fossil field hypothesis*”, Ferrario et al. 2009). The main challenge of the fossil field theory is to explain how the magnetic field can survive the convection during the Hayashi phase. Tayler (1987) proposed a mechanism, where the magnetic field is compressed into thin “ropes”, in which the strong field locally prevents the free flow of the stellar plasma, thus allowing (part of) the magnetic field to be preserved. An MHD simulation of a fossil magnetic field was done by Braithwaite & Spruit (2004).

An alternative to fossil fields is a magnetic field supported by a contemporary dynamo in the stellar core, as an analogy to the mechanism responsible for magnetism in lower-main sequence

stars. This theory, however, has serious difficulties explaining the lack of correlation between magnetic field strengths and rotational velocities, as well as explaining the rather large variety of observed field geometries of magnetic Ap / Bp stars (Moss 2001).

Strong magnetic fields have also been observed in white dwarfs, the first one by Kemp et al. (1970). The strength of these magnetic fields typically reaches up to 10^9 Gauss (Schmidt et al. 2003). It has long been speculated, that the magnetic white dwarfs are the evolutionary descendants of magnetic Ap and Bp stars (see, e.g., Woltjer 1960; Tout et al. 2004). The fossil magnetic field, “frozen” into the stellar plasma, persists through the evolutionary stages of the star, while the magnetic flux at the stellar surface is conserved. This idea has been questioned by, e.g., Liebert et al. (2005, 2015), arguing that, while about 25 % of known magnetic stars are found in binaries paired with main-sequence stars, there is practically no known magnetic white dwarf discovered in such a binary system. As an alternative to this theory, Tout et al. (2008) suggests the magnetic field in white dwarfs is a result of two white dwarfs merging during a common envelope phase. Potter & Tout (2010) then proposed a model, where a magnetic field is maintained by a dynamo generated by differential rotation of the envelope.

2.2.3 Variability of CP stars

A common phenomenon encountered in peculiar stars is spectral variations. For example, a survey of spectra of Ap and Bp stars conducted by Bonsack (1974) discovered variations in approximately one-half of the studied stars. These changes are typically explained by the oblique rotator model and inhomogeneous distribution of the various chemical elements across the stellar surface and rotation of the star. The detailed discussion of these spectroscopic variations and their interpretation will be the subject of the next chapter.

In many cases, especially among Ap stars, the inhomogeneous distribution of abundances also leads to photometric variability due to spectral energy redistribution (see, e.g., Peterson 1970; Molnar 1973; Lanz et al. 1996). That is typically explained by spectral energy redistribution due to the line-blocking and backwarming effect. While the total bolometric flux of the star remains unchanged due to the energy conservation considerations, the energy redistribution dependent on the local physical and chemical properties of the stellar photosphere will cause flux variations in individual spectral regions. This effect can be augmented by Zeeman splitting of the lines due to the presence of a strong magnetic field, but the difference is not significant except for extremely strong magnetic fields (Kochukhov et al. 2005; Khan & Shulyak 2006). This variability is usually relatively simple, and in most cases, it can be satisfactorily described by a simple, second or third degree harmonic function (Mikulášek et al. 2008a). In the following chapters, we will provide a more in-depth analysis of these photometric variations.

Long-term evolution of chemical abundances was studied on a sample of Ap / Bp stars in open clusters by Bailey et al. (2014), who found a correlation between the age of the stars and abundances of some elements. A slow decay in the strength of the magnetic fields has been observed by Fossati et al. (2016).

There is also a group of Ap stars, which lie in the area of the Hertzsprung–Russell diagram, in which the instability strip intersects the main sequence (Kurtz 1982). These stars exhibit fast non-radial p-mode oscillations. For that reason, they are usually referred to as “*rapidly oscillating Ap (roAp) stars*”. These stars are typically described using the oblique pulsator model, assuming non-radial pulsations along the magnetic axis. That suggests that the magnetic field plays an essential role in the oscillations of these stars. The photometric variability of these stars can then be explained as a result of the oscillation and photometric spots. The first roAp star to have its surface spots derived by the Doppler imaging technique was HD 24712 (Lüftinger et al. 2007, 2010a). The

abundance analysis revealed a strong, approximately dipolar magnetic field, a high and variable abundance of neodymium and iron, distributed in anticorrelation.

In the cases involving circumstellar matter such as the star σ Ori E, variable emission spectral lines, such as $H\alpha$ (Walborn 1973), and photometric changes can also be observed. These can be caused by reflection and scattering on the circumstellar disc, as well as absorption by the circumstellar matter when it occults the star.

2.2.4 Causes of peculiarity

There have been several hypotheses trying to explain the reason for the unusual chemical composition of the atmospheres of CP stars. Burbidge & Burbidge (1955) and Fowler et al. (1955) tried to explain the phenomenon, speculating that, under special conditions of the peculiar atmospheres, surface nucleosynthesis is possible. The authors looked for the possible processes, accelerating the particles to energies sufficient for such reactions to take place, suggesting the Swann betatron mechanism, according to which particles are accelerated by strong magnetic fields, but also acknowledging other possible phenomena, such as acceleration by magnetic shockwaves or neutral-point acceleration theories.

Fowler et al. (1965) suggested another idea. He assumed CP stars to be post-giant stage stars, possessing degenerate cores. The heavier elements are produced by internal nucleosynthesis; later they get to the stellar surface during the transition to a near-main sequence stage of their evolution. Guthrie (1967), however, points out the CP stars are actually at a much earlier evolutionary stage, as indicated by the frequent membership of these stars in very young stellar clusters and associations. The authors suggested the contamination of the stellar atmosphere by a supernova companion.

The most widely accepted explanation of the abnormal composition of the surface layers is currently the theory of radiative diffusion (Michaud 1970; Vauclair et al. 1991; Michaud et al. 2011; Alecian et al. 2011; Alecian & Stift 2019). The radiation flowing towards the outer layers of the star exerts a force on the particles present in the stellar plasma. In the continuum, this includes photoionization (the energy of the photon is transferred partially to the ion and partially to the freed electron) and free–free transitions. In lines, it is due to the bound–bound transitions (excitations). The radiation force is different for different chemical elements, and also depends on the ionization and excitation state.

The competition of gravity with the radiative force then leads to a very slow, gradual process of the selective transport of the particles with greater cross-section towards the outer layer of the star, whereas the atoms with small cross-sections settle down in the deeper layers of the star. In time scales as short as 10^4 years, this process can lead to significant chemical stratification of the stellar photosphere (Michaud 1970).

This theory is qualitatively consistent with the observed overabundances of Fe-peak, rare earth and lanthanide elements, underabundance of Ca, Sc, C, and He in Am stars, the unusual observed isotopic ratios of various elements (Kurtz & Martinez 2000). This process, of course, requires that the layers involved are very stable and calm, i.e., there is no convection occurring in the surface and sub-surface layers of the star. A strong, stable magnetic field plays a vital role in helping to satisfy this condition. Any mixing of matter within the photosphere would destroy any such elemental stratification. Similarly, fast rotation in such stars would lead to meridional circulation currents, with the same effect. Additionally, any massive mass loss from the star (stellar wind) would carry away the chemically enhanced layers of the photosphere (see, e.g., Landstreet et al. 1998; Unglaub & Bues 2001; Michaud et al. 2011). That is consistent with the fact that chemical peculiarities have never been observed in the late-type stars or hot O class main-sequence stars and why the vast majority of CP stars are slow rotators.

Contrary to expectations, it turns out that the abundance structures in magnetic CP stars do not strictly follow the magnetic field topology (Silvester et al. 2014; Rusomarov et al. 2016; Jagelka et al. 2019). The reason for this lack of correlation is not yet understood.

Chapter 3

Doppler Imaging

When a star exhibits periodic variations with a period of the light variability corresponding to its rotational period, this variability is typically explained by “*spots*”, i.e. inhomogeneous surface distribution of emergent radiation flux (Stibbs 1950). In areas of the stellar surface with increased abundance of heavier elements, presence of a large number of strong absorption lines, typically in the far ultra-violet part of the spectrum (“*line blanketing*”), as well as absorption in continuum due to bound–free processes, causes some portion of the radiative energy to be absorbed. Since the law of conservation of energy applies to stellar atmospheres, this energy has to be re-radiated; otherwise, it would accumulate indefinitely. Due to this absorbed energy, the temperature, and temperature gradient inside the atmosphere increases (“*backwarming effect*”), so that the energy is re-emitted as thermal radiation in continuum and the energy balance is maintained.

Therefore, the effects of the enhanced chemical composition of the stellar atmosphere can be detected both photometrically (the radiative flux observed from the parts of the atmosphere with a higher abundance of heavier elements will be reduced in spectral regions dominated by line absorption, while the flux from the areas with lower abundance will be higher in comparison) as well as spectroscopically (the line profiles belonging to elements with inhomogeneous surface distribution will differ in shape from the usual line profiles of elements distributed evenly across the stellar surface).

3.1 The oblique rotator

As the star rotates, the areas of its atmosphere with different chemical composition appear on the “western” side of the star, traverse the visible stellar disc, and disappear on the other side. Due to the Doppler effect, the light coming from the parts of the surface that are coming towards us (the western part of the disc) is shifted in frequency towards the blue end of the spectrum, whereas the light from the parts of the star going away from us (the eastern side of the disc) is shifted towards the red end of the spectrum. This leads to the line profile showing periodic variations in shape; the period of the variations being the same as the rotational period of the star.

Fig. 3.1 shows typical line profile variation in an idealized artificial star with inclination $i = 40^\circ$ and a single small spot with strongly increased abundance on an otherwise homogeneous surface. The individual panels show the different cases of the spot being located at different positions on the surface of the star – near the north pole (the left panel), on the northern hemisphere near the equator (the middle panel), and the southern hemisphere (the right panel). When the spot appears on the east side of the disc, a small “bump” shows in the blue wing of the line profile, slowly moving towards the red wing and varying in intensity as the spot moves to the east side of the disc.

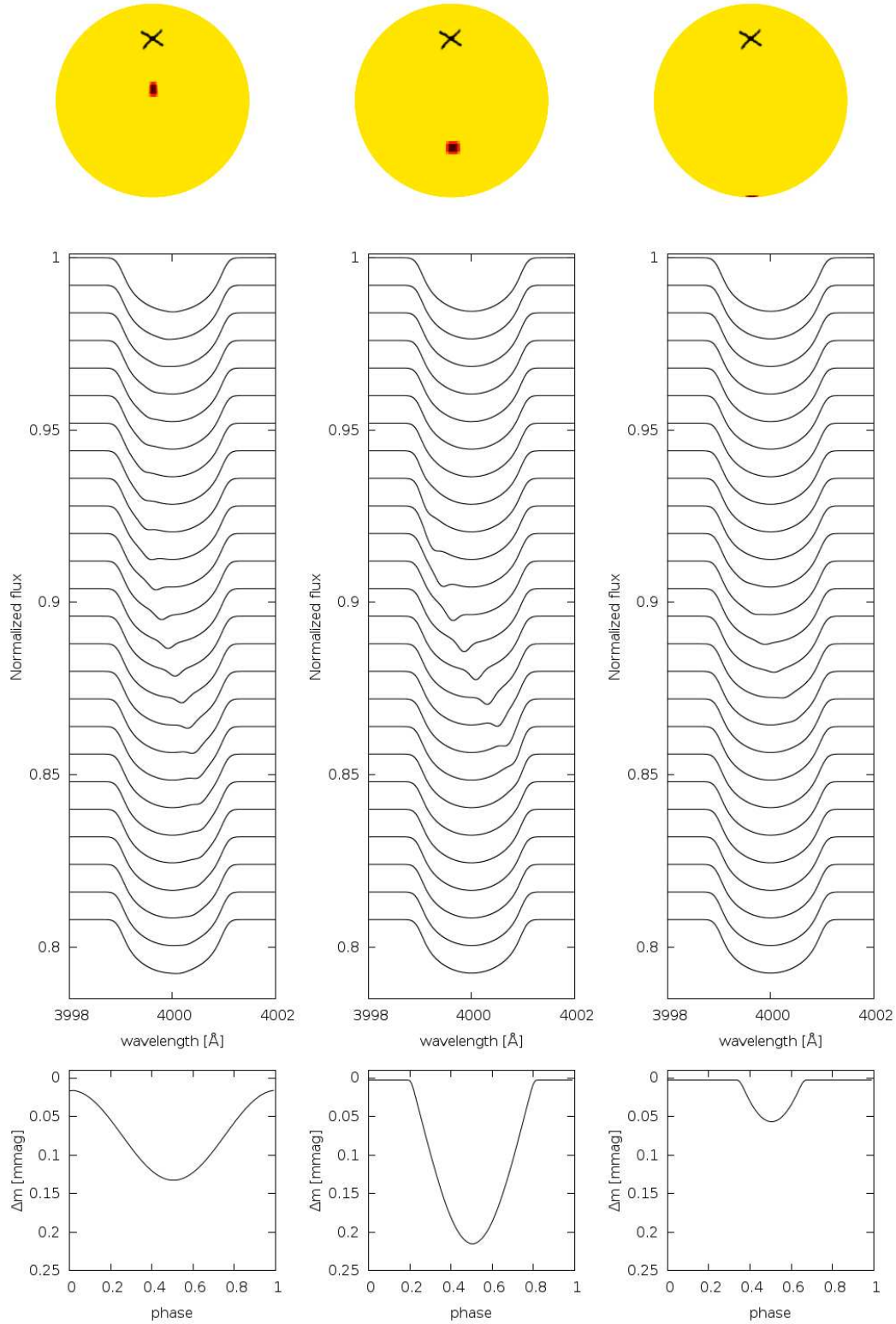


Figure 3.1: Stellar disc as seen by the observer (*top panel*), the corresponding line profile variations (*middle panel*), and light curves (*lower panel*) caused by a single small dark spot on the surface, depending on the astrographical latitude: 60° (*left panel*), 23° (*middle panel*), and -30° (*right panel*). Rotational phase in the profile plots is growing from the top towards the bottom from 0 to 1 in increments of 0.04.

The position of the spot on the surface influences the exact phases at which the spot becomes visible to the observer, as well as the wavelengths at which the “bump” appears in the line profile, and the intensity of this bump. When the spot is near the northern pole, it is visible for the entire rotational period. If the inclination of the star is low (we see the star “pole-on”), the contribution of the area containing the spot to the overall line profile is more significant. However, being very close to the rotational axis, its velocity relative to the observer only varies weakly, so the contribution of the spot to the line profile variability is rather small.

When the spot is near the equator, the velocity of the spot relative to the observer shows the greatest variations. The spot is visible to the observer for about one-half of the rotational period. The significance of the spot to the line profile variations will depend on the inclination of the star – it will be most pronounced when the inclination is high so that the spot will pass the visible stellar surface very close to the apparent center of the disc. The area near the equator plays an important role in explaining the variations in the wings of the line profile.

Spots on the southern hemisphere of the star are only visible for a short part of the rotational period. For this reason, the areas on the southern hemisphere are useful in explaining fast, short term variations. However, the spots in this area will also never get very close to the center of the stellar disc, so their contribution to the total line profile will be rather small, due to the small projection of the surface as well as the limb darkening.

3.2 The inverse problem

If we know the distribution of the heavier elements around the surface of the star, it is relatively straightforward to predict the line profile variations. That raises the question – if we know the line profile variations, can we derive the surface distribution of various chemical elements? The question is not easy to answer. The reconstruction of surface abundance is a classic example of an ill-posed problem – a one-dimensional spectrum line profile does not contain sufficient information to get a single unique solution. In order to derive the surface maps, other assumptions and constraints on the solutions must be imposed.

The inverse problem itself can be formulated in the following way (see, e.g., Rice et al. 1989): The observed line profile at any given phase is given by the integration of the local line profiles over the entire visible disc of the star. The local line profiles $R[M, \theta, \lambda + \Delta\lambda_D]$ at each point M on the stellar disc vary with the local chemical composition and physical conditions, and they are shifted in wavelength by $\Delta\lambda_D$, depending on their position on the disc due to the Doppler effect. In order to get the chemical composition at each area of the stellar surface, we need to solve, for each phase and wavelength, an integral equation of the form

$$R^*(\lambda, \varphi) = \frac{\iint I(M, \theta) R[M, \theta, \lambda + \Delta\lambda_D(M, \varphi)] \cos \theta dM}{\iint I(M, \theta) \cos \theta dM}, \quad (3.1)$$

where $R^*(\lambda, \varphi)$ is the depth of the line profile at phase φ and wavelength λ , $I(M, \theta)$ is the intensity in the continuum and θ is the angle between normal to the stellar surface and the line of sight.

The basic concepts of this *inverse problem* were discussed by Deutsch, who published a mathematical method of analyzing the line profile variations and reconstructing the surface element distribution using harmonic analysis to compute abundance maps of the star HD 125248 (Deutsch 1958, 1970). The surface abundances were determined using the variations of the line profiles’ equivalent width, radial velocities, and variations of the observed magnetic field strength. Much of the information contained in the line profiles was therefore not used.

Goncharskii et al. (1977) suggested a method based on Tikhonov regularization (Tikhonov 1963). Tikhonov's method is based on maximization of the functional

$$M^\alpha(\tau) = \Phi(\tau) + a_R S(\tau), \quad (3.2)$$

where $\Phi(\tau)$ is the *discrepancy functional*, i.e. an integration over wavelength and time of the discrepancy between observed and computed line profiles, and S is *entropy*, defined to be

$$S = - \iint f(\tau(M)) dM, \quad (3.3)$$

where f is a “*suitable defined function*”. For example, Rice et al. (1989) used

$$f(M) = \left(\frac{\partial \tau}{\partial l} \right)^2 + \left(\frac{\partial \tau}{\partial b} \right)^2, \quad (3.4)$$

where l and b are the stellar longitude and latitude. This makes the code favor smooth, simple solutions over overly complex ones.

During the computations, the surface of the star is split into small elements, inside which the parameters of the local atmosphere are assumed to be constant. There are two approaches to subdividing the stellar surface; either assuming elements of constant area (e.g., Vogt et al. 1987), or using elements with fixed step in latitude and longitudes. That, of course, means the elements vary in size, which has to be taken into account when computing the regularization, to get a reasonable abundance distribution around the rotational pole. The latter approach has been used in, e.g., Piskunov (1990).

Modeling the line profile variations to fit the observed line profiles as closely as possible is an important aspect of the inversion. Falk & Wehlau (1974) proposed a method assuming Gaussian shape for the local line profiles. However, this assumption is quite an unreasonable constraint, as in the areas with an increased abundance of the heavier elements, the absorption lines are often quite saturated, and the profile shapes differ from the Gaussian profile significantly. Goncharskii et al. (1982) approximated the local line profiles using the Minnaert formula (Minnaert 1935). That was not very accurate, but the algebraic expression describing the line profiles was convenient for the computations. Later codes (e.g., Piskunov & Rice 1993) used a precomputed look-up table of the model atmosphere based intensities computed by numerically integrating the radiative transfer equation for different values of wavelength, abundance, and $\cos \theta$.

The method has seen much improvement over the years and has been used many times to derive abundance distributions of various CP stars. For example, Pyper (1969) computed abundance maps of α^2 CVn. Similarly, Rice (1970) obtained maps of HD 173650. Piskunov & Kochukhov (2002) improved the method by including polarimetric measurements in the computation, simultaneously deriving the distribution of chemical abundances and the geometry of the magnetic field at the surface of the star α^2 CVn. Lüftinger et al. (2010b) presented abundance maps of sixteen chemical elements of the roAp star HD 24712.

3.3 V824 Cen

We are going to use the DI technique to derive abundance maps of the star V824 Cen (= HD 114365 = HIP 64320). The object is an A0p silicon star with an abnormal spectral line Eu II $\lambda 3930$ Å (Jaschek & Jaschek 1959). The magnetic field is very weak $\langle B_z \rangle = 8(100)$ G (Kochukhov & Bagnulo 2006). Manfroid & Renson (1983) determined rotational period $P = 1.273$ d. Catalano & Leone (1993) obtained new photometric data, which allowed them to refine the period

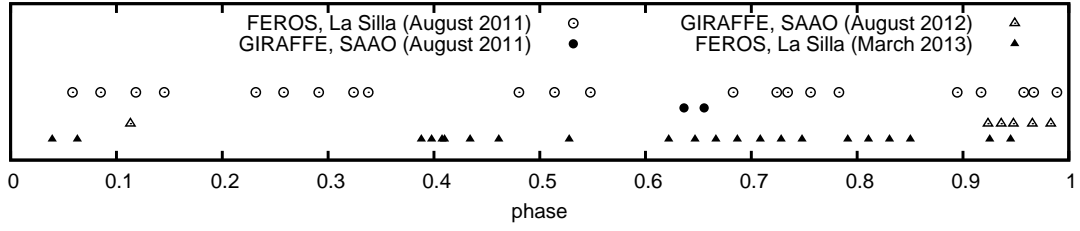


Figure 3.2: Phase coverage of spectroscopic observations of the star HD 114365 used for the Doppler imaging. Each symbol in the plot represents a single observation.

to $P = 1.271925(15)$. Using photometry from the ASAS and HIPPARCOS missions, we were able to further improve the rotational period, establishing a linear ephemeris $MJD = 55775.12658 + 1.2717042(14)$ (Mikulášek, private communication).

The spectroscopy we are going to use for mapping consists of four series of observations. 24 spectra were obtained using the GIRAFFE spectrograph with resolution $R = 40000$ at the South African Astronomical Observatory (SAAO) during two observing runs in August 2011 (2 spectra) and March 2013 (22 spectra), and 28 were observed with the FEROS spectrograph ($R = 48000$) at La Silla, Chile in August 2011 (22 spectra) and August 2012 (6 spectra). The coverage of the rotational period is shown in Fig. 3.2. One of the spectra obtained by FEROS, at the rotational phase 0.58 is plotted in Fig. 3.3. All the spectra were reduced and corrected for radial velocity by Dr. Jan Janík.

3.3.1 Fixing the stellar parameters

Table 3.1: Parameters of the spectral lines taken into account for modeling the Si 5055 Å line profile variations.

Element	Ion	Wavelength λ	Excitation energy E	$\log gf$	Damping parameters		
		[Å]			Rad.	Stark	Waals
Si	II	5055.9840	10.0740	0.593	9.040	-4.780	0.000
Ni	II	5056.1940	12.2940	0.500	8.956	-5.383	-7.769
Si	II	5056.3170	10.0740	-0.359	9.030	-4.780	0.000

After comparing the spectra with a set of synthetic spectra produced using the LLModelsSE (Shulyak et al. 2004) and Synth3 (Kochukhov 2007) programs, we decided to adopt the values $T_{\text{eff}} = 13200$ K and $\log g = 3.5$ for our models. The mapping itself was performed by the code INVERS12 (Kochukhov et al. 2004; Kochukhov 2017). The code supports non-magnetic inversion of several spectral intervals and two chemical elements simultaneously and computes the line profiles on the fly. The computation of the radiative transfer is parallelized using the Message Passing Interface (MPI). The atomic data were taken from the Vienna Atomic Line Database (VALD) (Piskunov et al. 1995; Ryabchikova et al. 1997; Kupka et al. 1999, 2000).

The technique requires high-resolution spectra with good signal to noise. The spectra need to be well reduced; a poor continuum fit may introduce non-existent variability into the computation, resulting in incorrect abundance maps. A relatively high rotational velocity projection is desired in the studied star so that the rotational broadening is the dominant factor affecting the width and the shape of the line profiles.

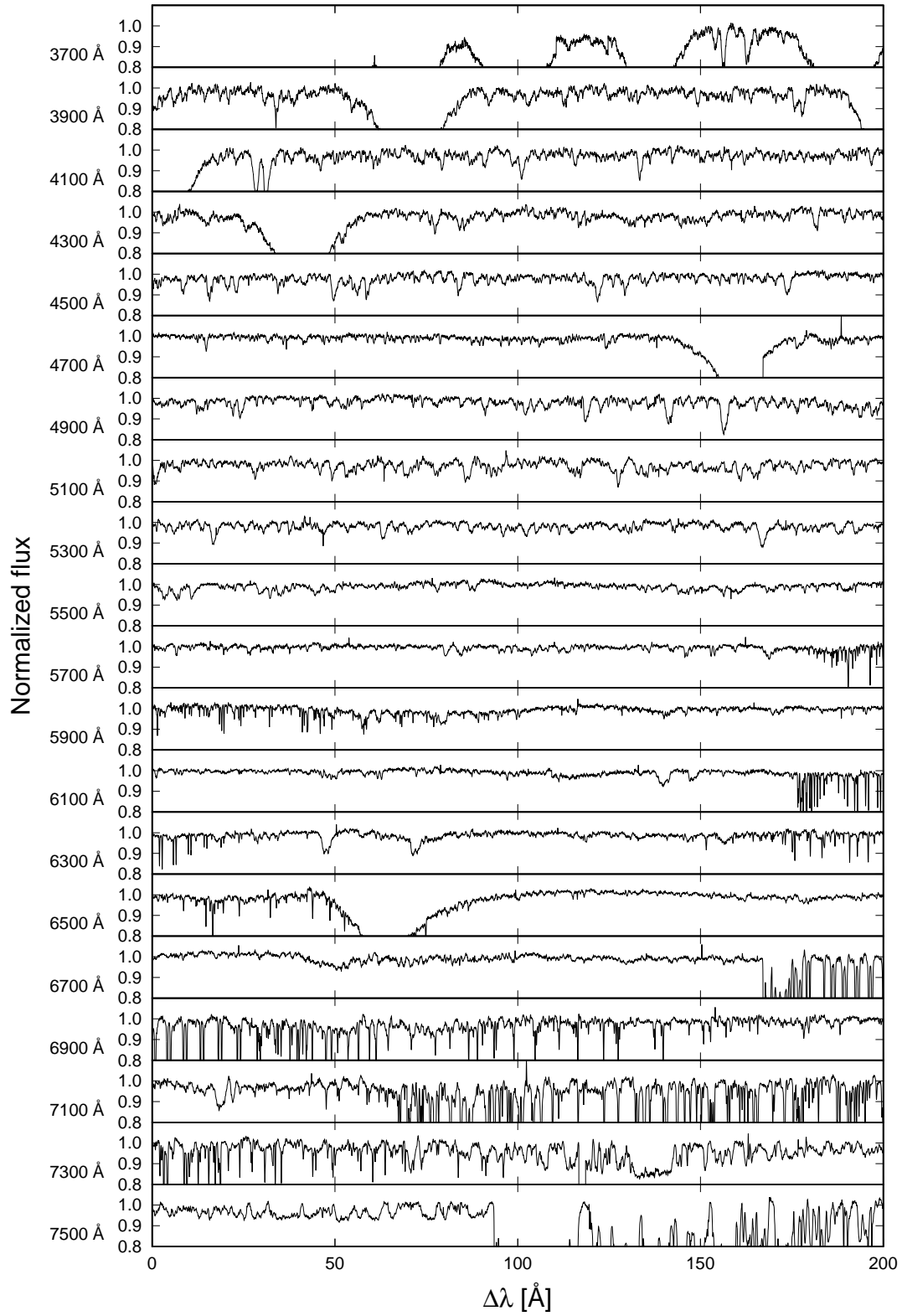


Figure 3.3: A spectrum of the star HD 114365 at rotational phase $\varphi = 0.58$ (FEROS, La Silla, Chile). The numbers along the left hand side denote the wavelength at the start of each plot.

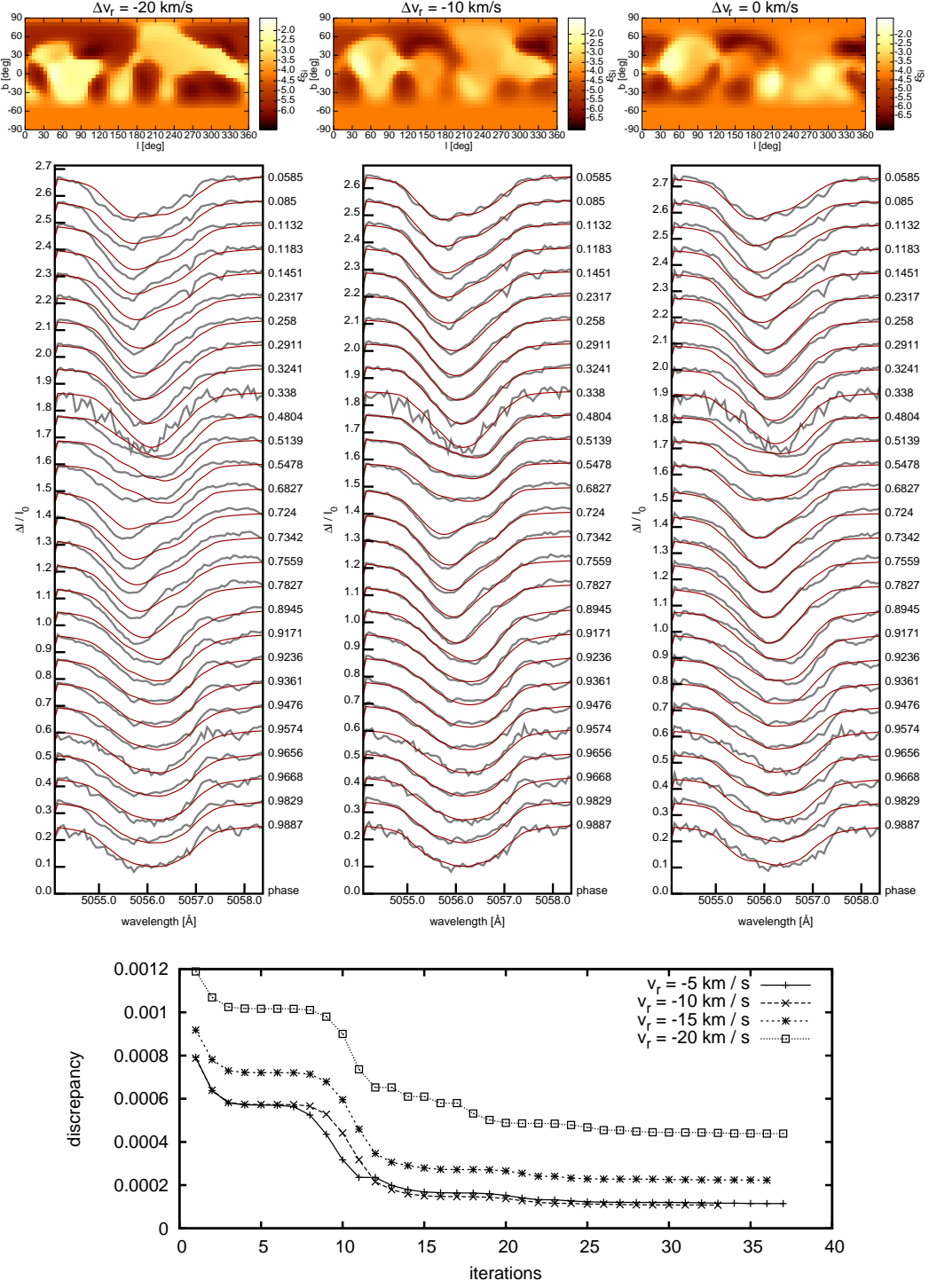


Figure 3.4: Abundance maps (*top panels*) of silicon derived from the profile variation of the silicon line at 5055 \AA in the FEROS spectra for inclination $i = 50^\circ$, $v \sin i = 60 \text{ km/s}$, regularization parameter $a_R = 0.015$, and different values of radial velocity correction Δv_r : -20 km/s (left), -10 km/s (middle), and 0 km/s (right), along with the corresponding line profile fits *middle panels*. The bottom panel shows the average discrepancy between the observed and the modeled line profiles plotted versus the number of iterations. The gray lines in the profile plots show the observed spectra; the red line shows the INVERS12 fits.

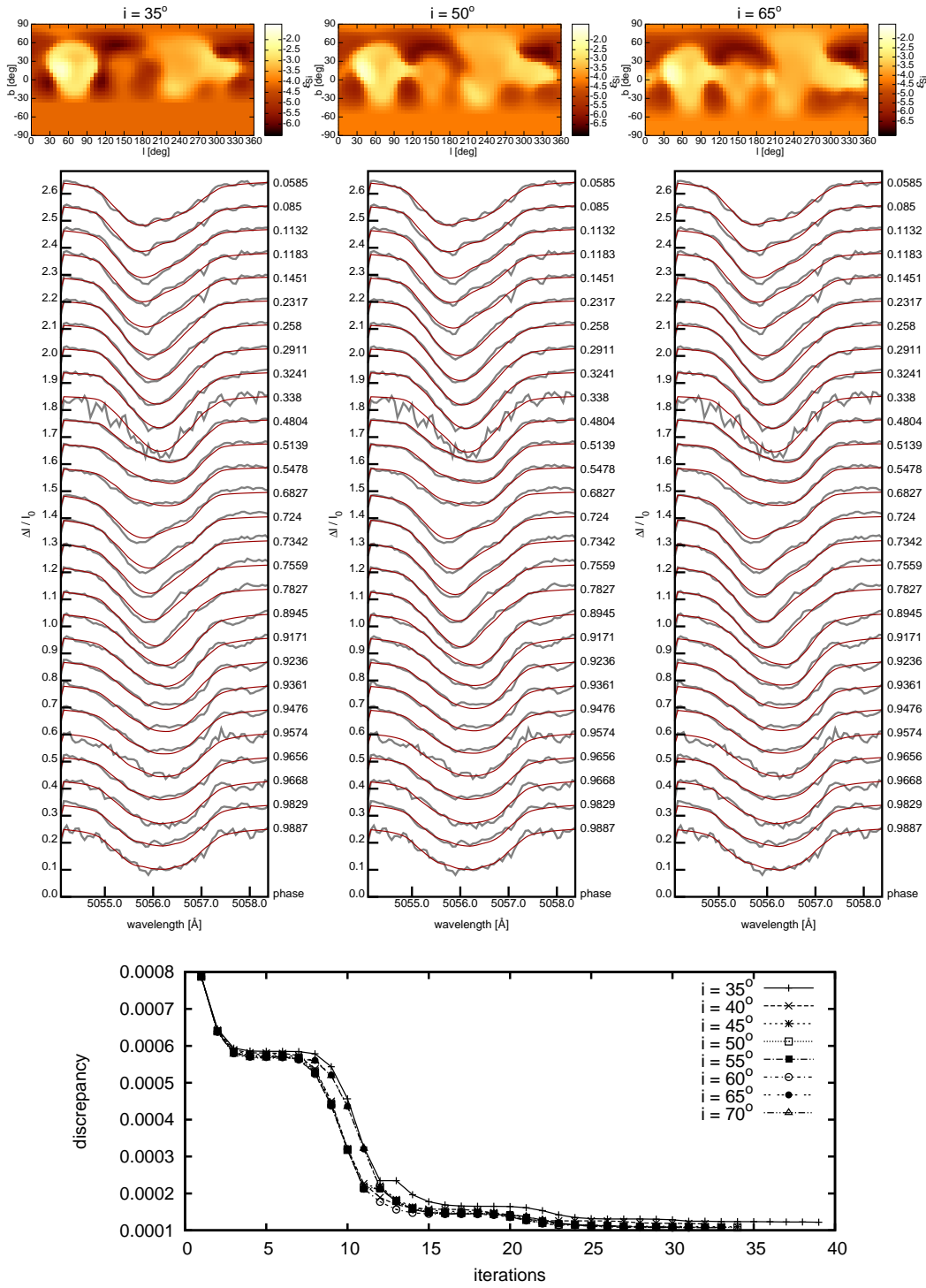


Figure 3.5: Abundance maps (*top panels*) of silicon derived from the profile variation of the silicon line at 5055 Å in the FEROS spectra for $v \sin i = 60$ km/s, regularization parameter $a_R = 0.015$, and different values of inclination i : 35° (left), 50° (middle), and 65° (right), along with the corresponding line profile fits (*middle panels*). The bottom panel shows the average discrepancy between the observed and the modeled line profiles plotted versus the number of iterations. The gray lines in the profile plots show the observed spectra; the red line shows the INVERS12 fits.

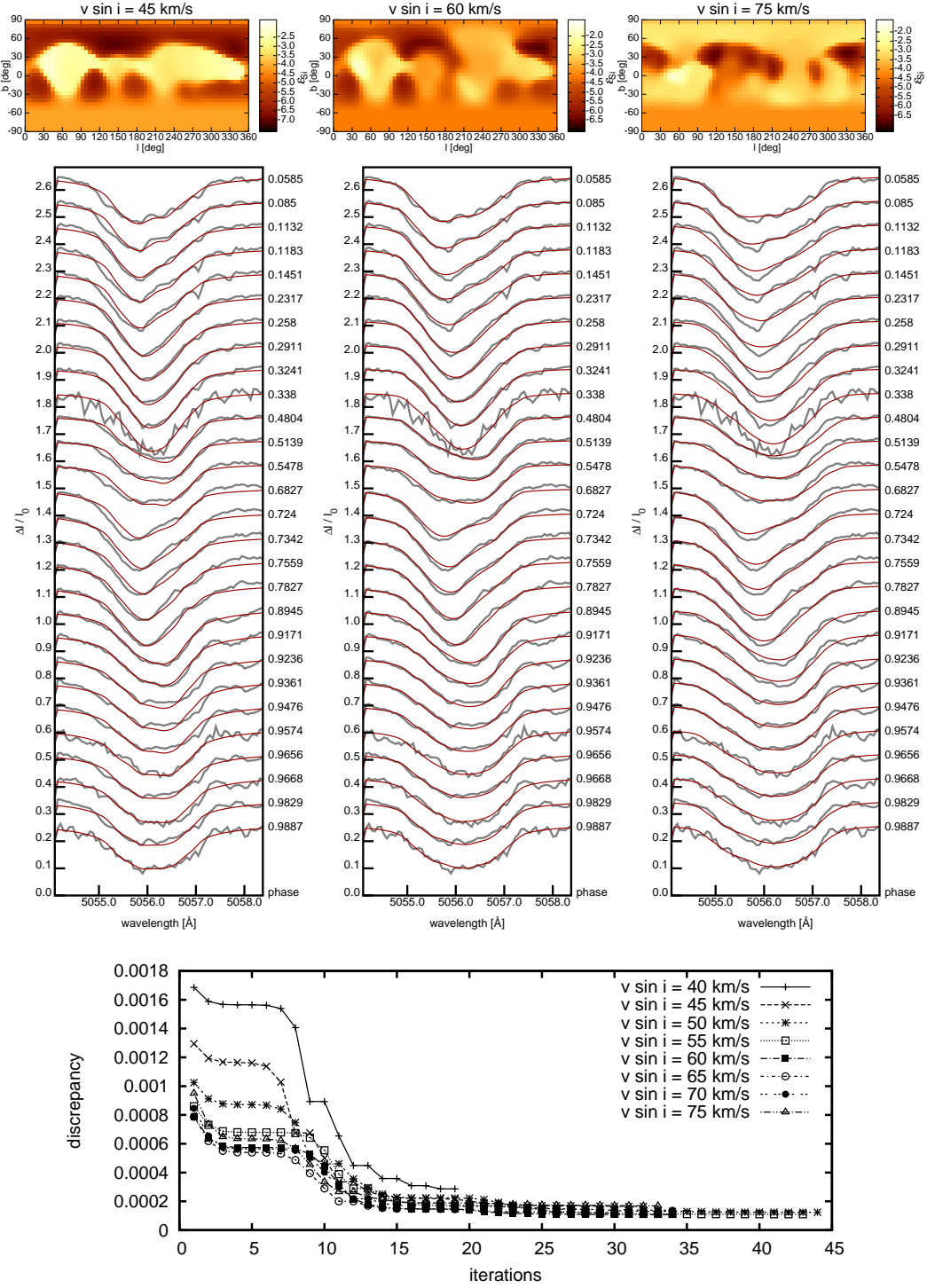


Figure 3.6: Abundance maps (*top panels*) of silicon derived from the profile variation of the silicon line at 5055 Å in the FEROS spectra for inclination $i = 50^\circ$, regularization parameter $a_R = 0.015$, and different values of $v \sin i$: 45 km/s (left), 60 km/s (middle), and 75 km/s (right), along with the corresponding line profile fits (*middle panels*). The bottom panel shows the average discrepancy between the observed and the modeled line profiles plotted versus the number of iterations. The gray lines in the profile plots show the observed spectra; the red line shows the INVERS12 fits.

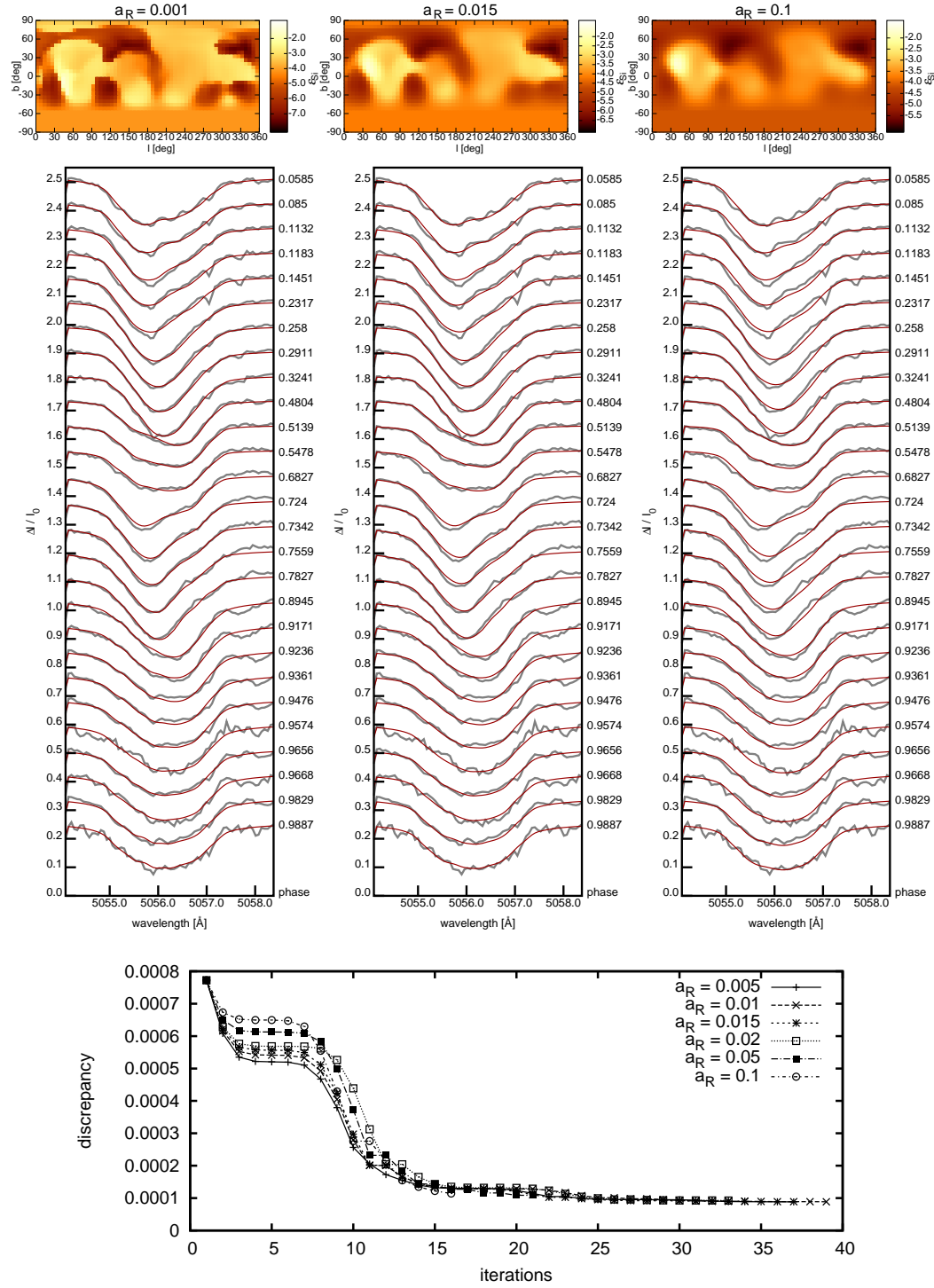


Figure 3.7: Abundance maps (*top panels*) of silicon derived from the profile variation of the silicon line at 5055 Å in the FEROS spectra for inclination $i = 50^\circ$, $v \sin i = 60$ km/s, and different values of the regularization parameter a_R : 0.001 (left), 0.015 (middle), and 0.1 (right), along with the corresponding line profile fits (*middle panels*). The bottom panel shows the average discrepancy between the observed and the modeled line profiles plotted versus the number of iterations. The gray lines in the profile plots show the observed spectra; the red line shows the INVERS12 fits.

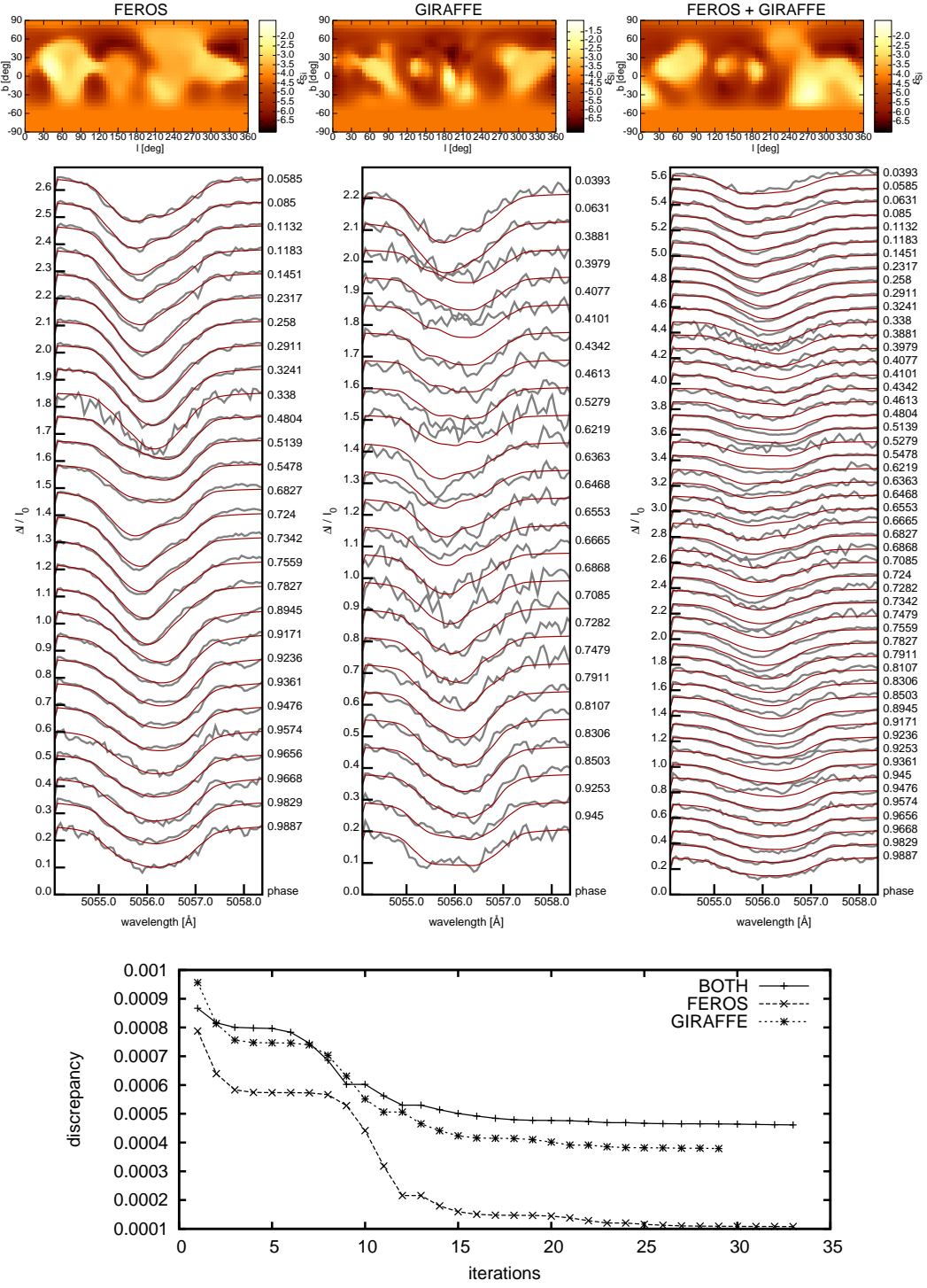


Figure 3.8: Abundance maps (*top panels*) of silicon derived from the profile variation of the silicon line at 5055 Å for inclination $i = 50^\circ$, $v \sin i = 60$ km/s, and regularization parameter $a_R = 0.015$, derived from the FEROS spectra (left), GIRAFFE spectra (middle), and all spectra together (right), along with the corresponding line profile fits (*middle panels*). The bottom panel shows the average discrepancy between the observed and the modeled line profiles plotted versus the number of iterations. The gray lines in the profile plots show the observed spectra; the red line shows the INVERS12 fits.

We inspect the spectra carefully, searching for spectral lines suitable for mapping. We prefer stronger lines with well-pronounced profile variations and as little noise as possible. At first, we avoid blended lines, where more than one chemical element contributes to the variability. Eventually, as the abundance maps of the other variable elements involved are derived, we may process the blended lines of two chemical elements, using the already known abundance distribution of one of the two elements as input for the code, to derive the abundance map of the other element. For now, we will only map a single line at a time, but the code supports the mapping of up to three individual contiguous wavelength ranges simultaneously, so eventually, we will want to derive the maps using multiple spectral lines at the same time whenever possible, to obtain better maps.

For each line we map, a narrow range of the spectra surrounding the mapped line is extracted, corrected for radial velocity and merged into a single input file. Correction of the continuum fit for this short wavelength interval can be made during the extraction. The INVERS12 program, which is currently not publicly available, comes with a suite of tools written in the Interactive Data Language (IDL), which can be used to process the spectra and prepare the input files as mentioned above, and also to process the output files and generate corresponding postscript plots that can be viewed with common software. However, in the end, we found it more convenient to implement our own set of tools.

The GIRAFFE and FEROS spectra were obtained using instruments of different qualities and at different times. Before we make sure that the two sets are compatible, we are going to use them separately. After a test run of the code, there seems to be a systematic shift in wavelengths of the observed spectra relative to the models. We assumed the cause of this to be an incorrectly determined value of the radial velocity of the star. Therefore, we produce a set of abundance maps with different values of the radial velocity corrections. The results for the line Si 5055 Å are shown in Fig. 3.4. The plots show the resulting abundance maps of silicon, with abundance defined as $\varepsilon_{\text{el}} = \log(N_{\text{el}}/N_{\text{tot}})$, as well as the corresponding line profile fits and a dependence on number of iterations of the average discrepancy defined as

$$\sigma = \frac{1}{n_{\lambda}n_{\varphi}} \sum_{\lambda} \sum_{\varphi} (I_{\text{mod}} - I_{\text{obs}})^2,$$

where n_{λ} is the number of wavelengths in the range of the spectrum considered in the computation and n_{φ} is the number of spectra. The spectral lines and their parameters that were assumed during the computation are listed in Table 3.1. As the result indicates, correcting the radial velocity by value $\Delta v_r = -10$ km/s fixes the discrepancy and gives the best agreement between the models and the observations. Performing the same procedure for several other spectral lines, for both the FEROS and the GIRAFFE spectra, yields the same result. We are therefore going to use the correction by -10 km/s and use the new value of the radial velocity from now on. The change in radial velocity causes minor changes in the resulting maps.

The inclination of the star is not known. We tested several different values of i in the interval between 35° and 70° and assumed the value of $i = 50^\circ$, which produced the best convergence, to be the correct value and adopted it for the following computations. The plot showing the results of the mapping for the different values of the inclination is given in Fig. 3.5. The value of the inclination affects the distribution of abundances in latitude.

Using similar reasoning, we determine the value of the rotational velocity $v \sin i$. If $v \sin i$ is set too high, the modeled line profile will be too wide, and the code will not be able to achieve a satisfactory agreement with the observations. If, on the other hand, the assumed value of $v \sin i$ is too low, the modeled profiles will be too narrow, and the code will not be able to model variations in the wings of the observed line profiles. Special care must be taken not to confuse changes in the wings of the line caused by inconsistently reduced data for real spectral profile variations. A

set of maps and line profile fits computed with different values of $v \sin i$ is shown in Fig. 3.6. The value $v \sin i = 60$ km/s will be used in this work from now on. The value of the rotational velocity projection has quite a strong impact on the distribution of abundances in the resulting maps.

We also investigate the significance of the regularization parameter a_R . The maps derived with different values of this parameter are given in Fig. 3.7. The higher value of the regularization parameter results in smoother maps, but the fit of the observed line profiles is not as good. When a_R is too low, the code generally reaches much better convergence, but the resulting map is much less smooth, and the abundance structures are more complex. We need to find a suitable value for the regularization parameter, to obtain a reasonably good agreement with the observed spectral line profiles while avoiding the pitfall of overfitting the solution and deriving unrealistic abundance maps. In our case, we decided to pick the value $a_R = 1.5 \times 10^{-2}$ and use it for further mapping.

Finally, let's take a closer look at the two sets of spectra obtained with the two individual instruments. Fig. 3.8 shows the mapping attempts with the two sets used separately and then combining them. It is evident that the quality of the FEROS spectra is vastly superior to that of the spectra observed by GIRAFFE. The code reaches the best convergence when using only the FEROS dataset. Combining the two sets together results in some discrepancies. For example, the line profile between the rotational phases 0.66 and 0.8 are significantly deeper in the FEROS spectra than in their GIRAFFE counterparts, and consequently, the code has serious trouble fitting the alternating FEROS and GIRAFFE spectra. The discrepancy, when using both sets of spectra together, is greater than the discrepancy resulting from deriving the maps using each of the datasets separately. That implies there is something wrong with the spectra. The resulting abundance maps in the three cases also differ significantly. The reason for these discrepancies is not yet clear, but before these problems are settled, we can not successfully merge the two sets. Due to the better signal to noise ratio of the FEROS spectra, we will only use these in the following computations.

3.3.2 Mapping other lines

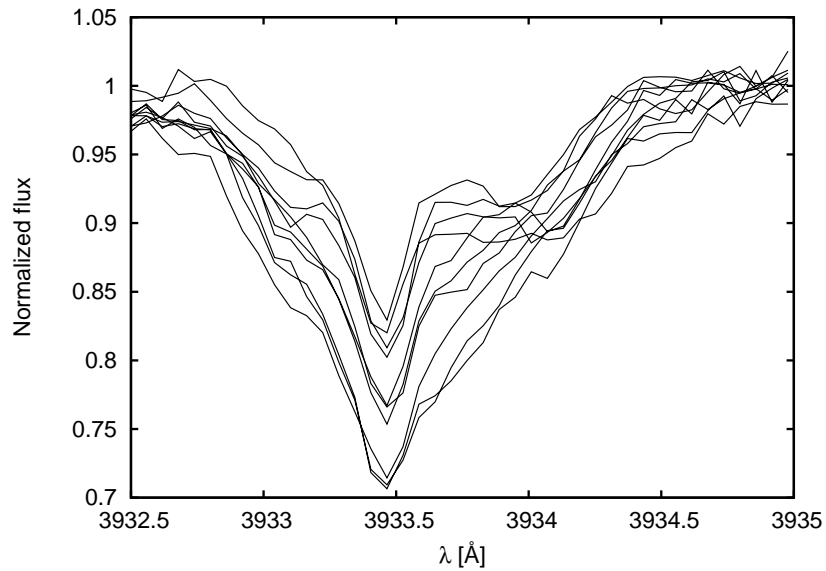


Figure 3.9: The profile of the spectral line Ca 3933 Å in FEROS spectra. The narrow peak in the middle of the profile originates in the interstellar medium.

Table 3.2: Parameters of the spectral lines taken into account for modeling the Mg 4481 Å line profile variations.

Element	Ion	Wavelength λ	Excitation energy E	$\log gf$	Damping parameters		
		[Å]	[eV]		Rad.	Stark	Waals
Al	III	4479.8850	20.7810	0.900	0.000	0.000	0.000
Al	III	4479.9710	20.7820	1.020	0.000	0.000	0.000
Fe	II	4480.6880	6.2260	-2.561	8.600	-6.520	-7.863
Mg	II	4481.1260	8.8640	0.740	0.000	0.000	0.000
Mg	II	4481.1500	8.8640	-0.560	0.000	0.000	0.000
Mg	II	4481.3250	8.8640	0.590	0.000	0.000	0.000

Table 3.3: Parameters of the spectral lines taken into account for modeling the Fe 4924 Å line profile variations.

Element	Ion	Wavelength λ	Excitation energy E	$\log gf$	Damping parameters		
		[Å]	[eV]		Rad.	Stark	Waals
Fe	II	4923.9270	2.8910	-1.504	8.520	-6.500	-7.884
S	II	4924.1100	13.6170	-0.059	8.860	0.000	0.000
S	II	4925.3430	13.5840	-0.235	8.860	0.000	0.000

Now that we have fixed the required parameters, we can attempt to map a few other lines. There is a very nice calcium line at 3933.663 Å (see Fig. 3.9). At first sight, it looks suitable for mapping; there is relatively little noise, it shows well pronounced variations, and no other element contributes significantly to the variability. However, the sharp peak in the middle of the line originates in the interstellar medium (ISM). The Ca 4233.663 Å, a strong, well known ISM line (see e.g., Cox 2000), is distorting the line profile. Until we find a way to eliminate the influence of the ISM line, we cannot use this line for mapping.

The next candidate is the magnesium line at 4481 Å. It is a very strong unblended line. The few other relatively weak lines contributing to the line profile will be regarded as non-variable during the mapping. The list of these lines and their parameters is given in Table 3.2. The resulting map and the line profile fits are shown in Fig. 3.10. The map contains a few bright spots; abundances range between -7.5 and -3.4 .

The iron line at 4924 Å can be used to derive the abundance map of iron. The lines involved in the computation are listed in Table 3.3. Model atmospheres indicate a helium line nearby, which

Table 3.4: Parameters of the spectral lines taken into account for modeling the Si 5041 Å line profile variations.

Element	Ion	Wavelength λ	Excitation energy E	$\log gf$	Damping parameters		
		[Å]	[eV]		Rad.	Stark	Waals
Ni	II	5039.8470	12.2800	0.032	9.328	-5.563	-7.770
Ni	II	5040.3450	12.2710	0.574	8.949	-5.455	-7.770
Fe	II	5040.7590	10.3600	-0.637	8.990	-4.900	-7.570
Si	II	5041.0240	10.0670	0.291	9.030	-4.780	0.000
Ni	II	5042.4300	12.5680	0.574	8.956	-5.397	-7.769

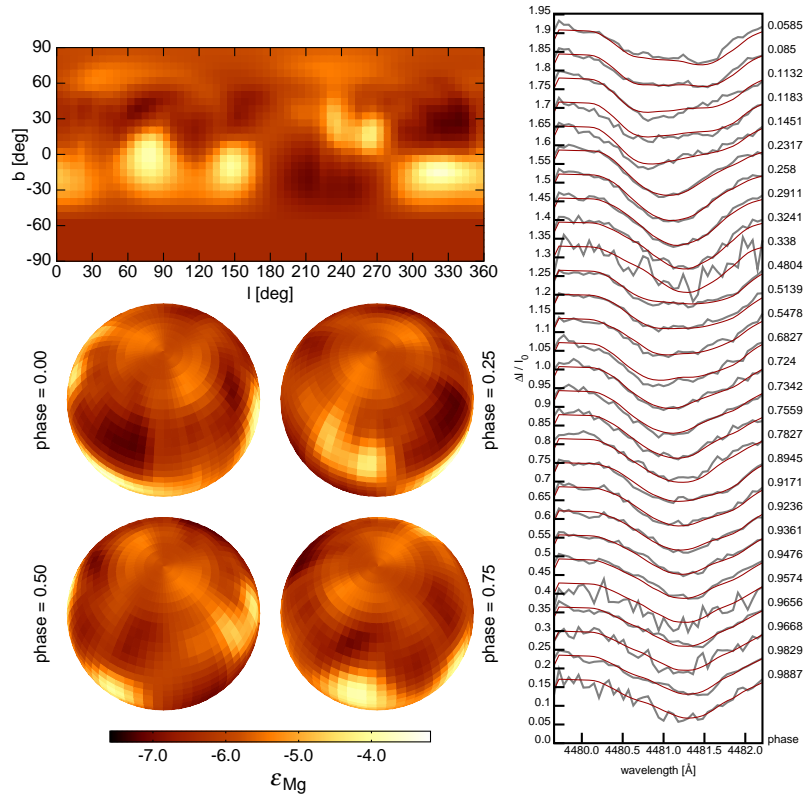


Figure 3.10: Abundance map (*left panel*) of magnesium derived from the profile variations of the magnesium line at 4481 Å in the FEROS spectra and the corresponding line profile fits (*right panel*). The gray lines in the profile plots show the observed spectra, the red line shows the INVERS12 fits.

could interfere with the blue wing of the line profile, but due to the low abundance of helium in this star, the helium line is barely visible in the observed spectra. The resulting map is shown in Fig. 3.11. It features a large, lengthy structure of increased abundance, spanning from 220 degrees to 90 degrees in longitude. The abundance ranges from -6.5 to -1.0.

Another silicon line suitable for mapping is at 5041 Å. The map derived from this line is presented in Fig. 3.12, the corresponding line information is summarized in Table 3.4. It agrees in general features with the silicon map derived from the line Si 5055 Å, but minor differences are noticeable.

3.4 Conclusions

We have discussed the technique of Doppler imaging. We have shown how it can be used to obtain valuable information about the surface distribution of chemical elements in CP stars. The technique is a very powerful and useful tool allowing us to perform a detailed surface abundance analysis of CP stars. Usage of the complete information contained in the high-resolution optical spectra gives much more reliable results than any attempts to derive the abundance maps using only radial velocities or equivalent line widths. However, the solution is still not unique, and the information about the distribution of abundances in latitude cannot be derived with absolute certainty. This can be partially fixed by also including the information hidden in spectropolarimetric measurements, as in e.g., Piskunov & Kochukhov (2002) or Lüftinger et al. (2010b).

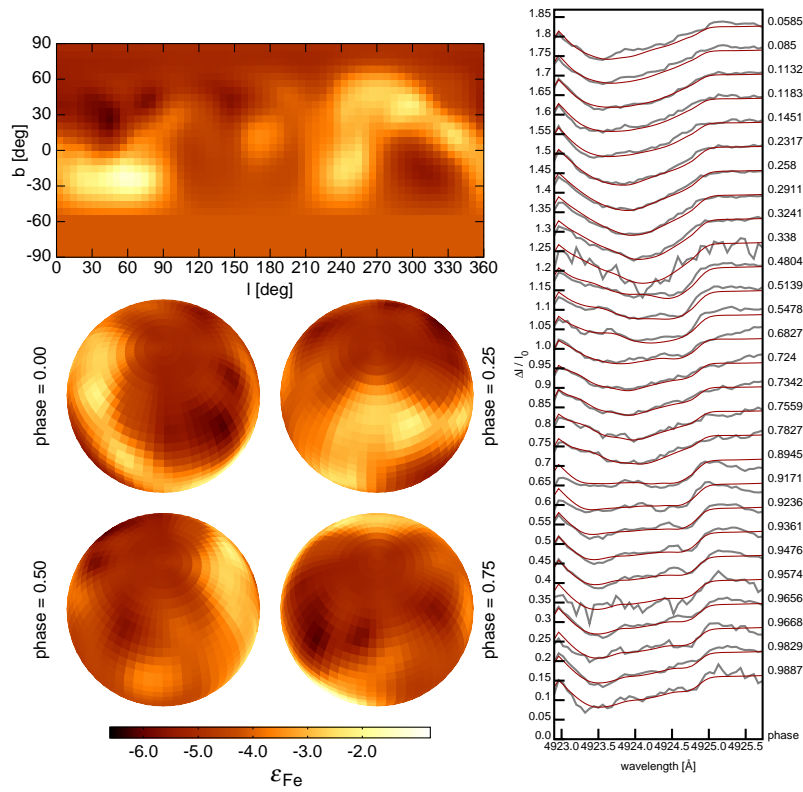


Figure 3.11: Abundance map (*left panel*) of iron derived from the profile variations of the iron line at 4924 Å in the FEROS spectra and the corresponding line profile fits (*right panel*). The gray lines in the profile plots show the observed spectra, the red line shows the INVERS12 fits.

There are also many pitfalls involved in the procedure; being careless, one can easily end up with incorrect results. In order to successfully derive the abundance structures, we need to know many parameters of the star such as the effective temperature, surface gravity, inclination, radial velocity, rotational velocity projection. Many of these are quite challenging to determine reliably, especially for CP stars, whose spectra and spectral energy distribution often differ significantly from common stars of the corresponding spectral class. If these parameters are not known beforehand, they need to be obtained from mapping, usually assuming, in good faith, that the best fit implies the correct value of the parameter.

We have shown how the various parameters affect the quality and appearance of the abundance maps and the line profile fits. We have demonstrated the process of Doppler imaging, using the star V824 Cen as an example. We derived abundance maps of several chemical elements, namely silicon, iron, and magnesium. However, the mapping of this star is still a work in progress, and much work remains to be done. The abundance maps shown in this chapter were presented here as an illustration of the technique and should by no means be regarded as final results.

The good and complete knowledge of the chemical composition of the stellar atmosphere is desirable for the mapping because many spectral lines are blended, and the overall shape of the line profiles is affected by multiple spectral lines, often belonging to different chemical elements. So, in order to derive a good abundance map of one element, we need to know the abundance of another element, and so on. Ideally, when the abundances are updated, the model atmosphere should be recomputed with the new parameters. The lines in the observed spectra are often hard to identify, especially considering the high overabundance of many quite uncommon chemical

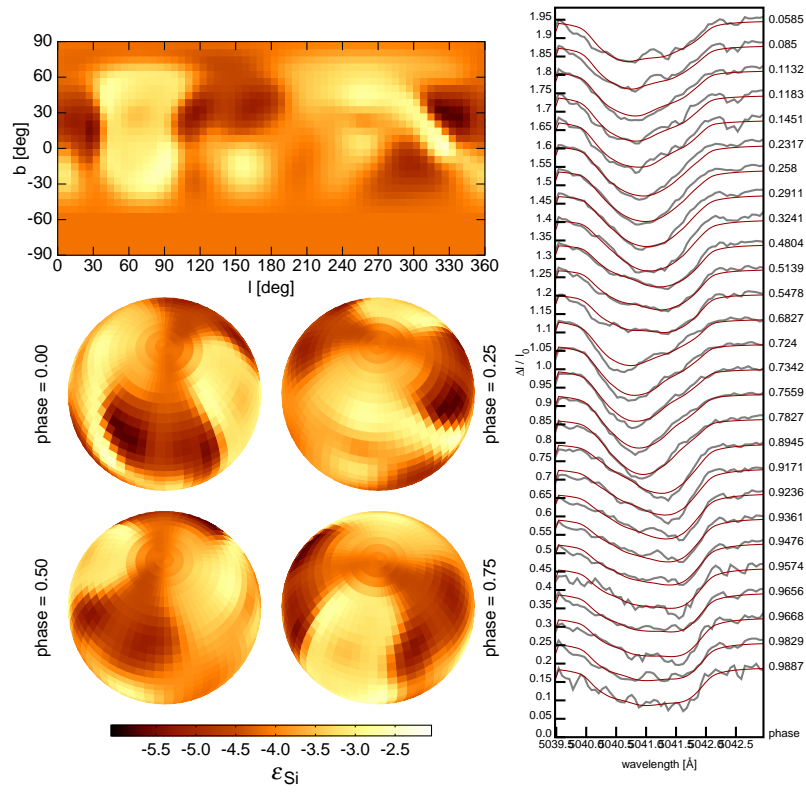


Figure 3.12: Abundance map (*left panel*) of silicon derived from the profile variations of the silicon line at 5041 Å in the FEROS spectra and the corresponding line profile fits (*right panel*). The gray lines in the profile plots show the observed spectra, the red line shows the INVERS12 fits.

elements. Spectral lines of the interstellar medium, as well as (generally in the red part of the spectrum) the molecular lines originating in the Earth's atmosphere, interfere with the spectrum of the star, often appearing in the middle of the line profiles we want to use for mapping. That all makes the DI a rather lengthy, iterative process requiring much patience and experience. However, the valuable results that are obtained from the procedure make the effort worthwhile.

Chapter 4

Synthesizing light curves from abundance maps

If the abundance maps of a star are available, predicting the photometric variability is a relatively straight-forward task. Computing synthetic light curves and comparing them with the observed photometric variability of the star can be a useful verification of the accuracy of the map, correctness of the underlying physics, the atomic data, the concept of the oblique rotator, and our understanding of the processes taking place inside stellar atmospheres. Of course, an agreement of the synthesized light curve with the observation does not prove conclusively that the maps and the model are correct, but it helps increasing the level of credibility. Discrepancies between the model and the observations, on the other hand, can help us find imperfections of our model, identify sources of absorption we didn't notice before, and improve the accuracy of the atomic data. Additionally, it helps us understand, which physical processes and which chemical elements contribute to the photometric variability of the star.

The flowchart in Fig. 4.1 shows the basic idea of the stellar surface analysis. The star provides us with two kinds of input – the spectrum and the photometric information. Doppler imaging uses the former to derive the abundance maps. With the level of understanding of the physics of stellar atmospheres and precision of the atomic data available to us in the 21st century, it is now possible to predict the photometric variability of the star caused by the inhomogeneous distribution of the chemical elements from the abundance maps of these elements. The result can then be compared with the observed photometry of the star. The method has been used with success in the past to explain light variations of various stars. Krivoseina et al. (1980) derived surface distribution of silicon at the surface of the star CU Vir using the variations of the equivalent widths and radial velocities of spectral lines in the observed spectra. They used the maps to compute the photometric variability. The resulting light curves nicely agree with observations (see Fig. 4.2).

Krtićka et al. (2007) studied the photometric variability of the star HD 37776. HD 37776 is a hot ($T_{\text{eff}} = 22000$ K) helium-strong CP star with a strong and relatively complex magnetic field (Kochukhov et al. 2011). It's spectroscopic variability had been attributed to inhomogeneous surface distribution of heavier elements. Using abundance maps for He and Si derived by Khokhlova et al. (2000), light curves were synthesized in Strömgren u , b , v , and y filters, which agree nicely with the observed variability of the star. Authors concluded the variability is caused mainly by bound-free transitions of silicon and helium.

Krtićka et al. (2009) used abundance maps derived by Lehmann et al. (2007) to model light variability of the A0p star ($T_{\text{eff}} = 14500$ K) HR 7224. Besides showing the observed photometric variability is caused by bound-free transitions of iron and absorption in lines of iron, they improved the ephemeris of the star.

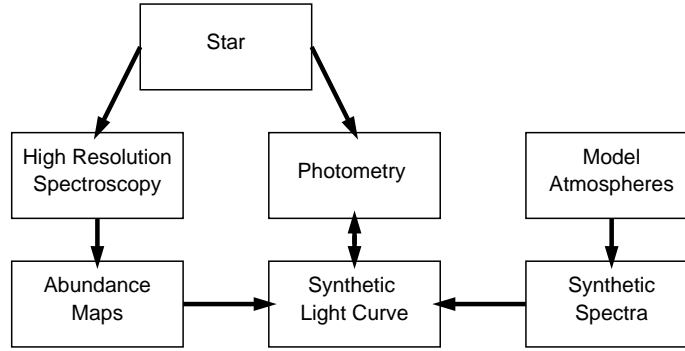


Figure 4.1: Flowchart illustrating the basic idea of the abundance mapping and verification by synthesis of the photometric variability (taken from Prvák et al. 2018).

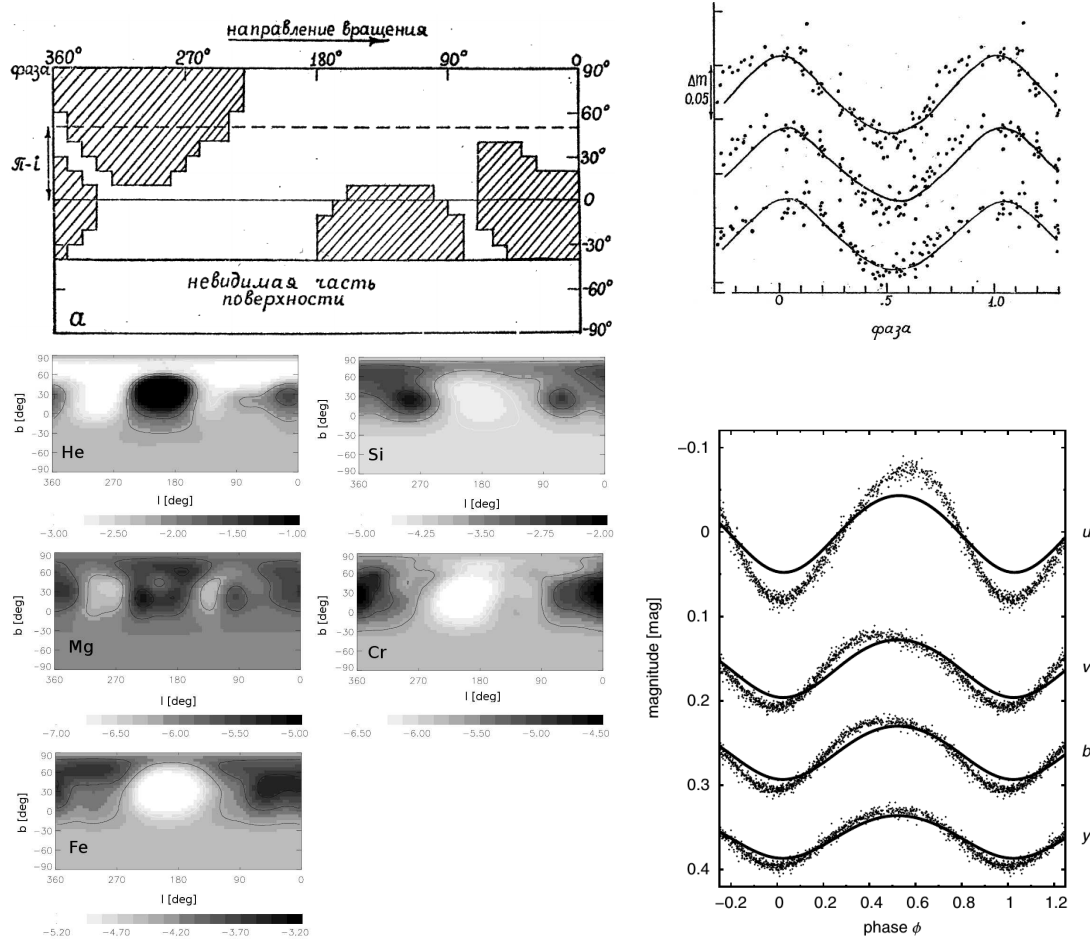
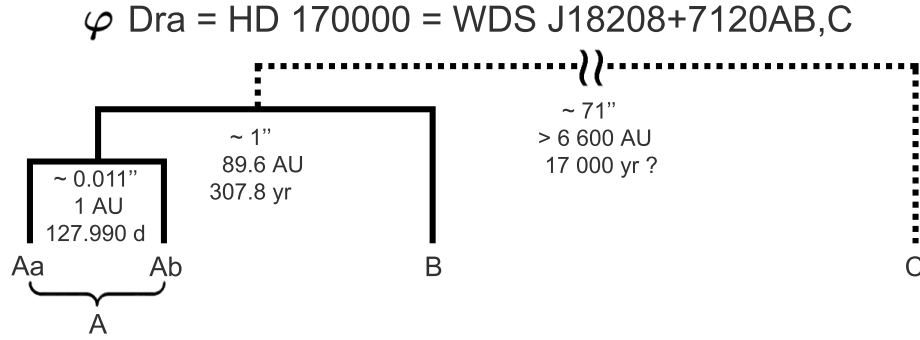


Figure 4.2: Mapping and light curve synthesis for CU Vir. *Top*: abundance map of silicon (left) and the corresponding light curves (right) plotted against observations, both taken from Krivoseina et al. (1980). The *Bottom left*: abundance maps derived by Kuschnig et al. (1999). The abundances are given as $\log(N/N_{\text{H}})$. *Bottom right*: light curves computed by Krtićka et al. (2012) plotted against observations by Pyper et al. (1998).

Figure 4.3: Structure of the multiple stellar system of φ Draconis (taken from Liška 2016).Table 4.1: Parameters of φ Dra from spectroscopy (Kuschnig 1998), including ranges of surface chemical abundances given as $\log N/N_{\text{H}}$ (solar abundance for each element adopted from Grevesse & Sauval (1998) is given in parentheses).

Effective temperature T_{eff}	12 500 K
Surface gravity $\log g$ (cgs)	4.0
Inclination i	60°
Apparent magnitude V	4.22 mag
Rotational velocity projection $v_{\text{rot}} \sin i$	95 km s^{-1}
Helium abundance	$-2.7 < \varepsilon_{\text{He}} < -2.1$ (−1.00)
Silicon abundance	$-4.4 < \varepsilon_{\text{Si}} < -3.1$ (−4.45)
Titanium abundance	$-7.1 < \varepsilon_{\text{Ti}} < -6.5$ (−6.98)
Chromium abundance	$-6.5 < \varepsilon_{\text{Cr}} < -5.2$ (−6.33)
Iron abundance	$-4.9 < \varepsilon_{\text{Fe}} < -3.6$ (−4.50)

Shulyak et al. (2010) explained the photometric variability of ϵ UMa by uneven surface distribution of heavier elements using the maps of Ca, Cr, Fe, Mg, Mn, Sr, and Ti computed by Lüftinger et al. (2003).

Krtićka et al. (2012) attempted to explain the light variation of CU Vir again using abundance maps computed by Kuschnig et al. (1999). They showed the photometric variability is caused by spots of He, Si, Cr, Mg, and Fe. Modeled light curves fit the observed photometry relatively well, except in the Strömgren u band, where it can only explain a part of the observed changes. The authors conclude the discrepancy is caused by an unidentified source of variability contributing to the light variation in this spectral range. Fig 4.2 compares the abundance maps and the resulting light curves with the previous work of Krivoseina et al. (1980).

4.1 φ Draconis

We will illustrate the synthesis of the light curve on an example of one of the brightest known chemically peculiar stars φ Dra (HD 170000 = HR 6920). The work was published in Prvák et al. (2015). The following text is a rephrased version of the paper. The peculiar character of this star was mentioned in Maury & Pickering (1897). It is a typical Ap star with photometric spots with

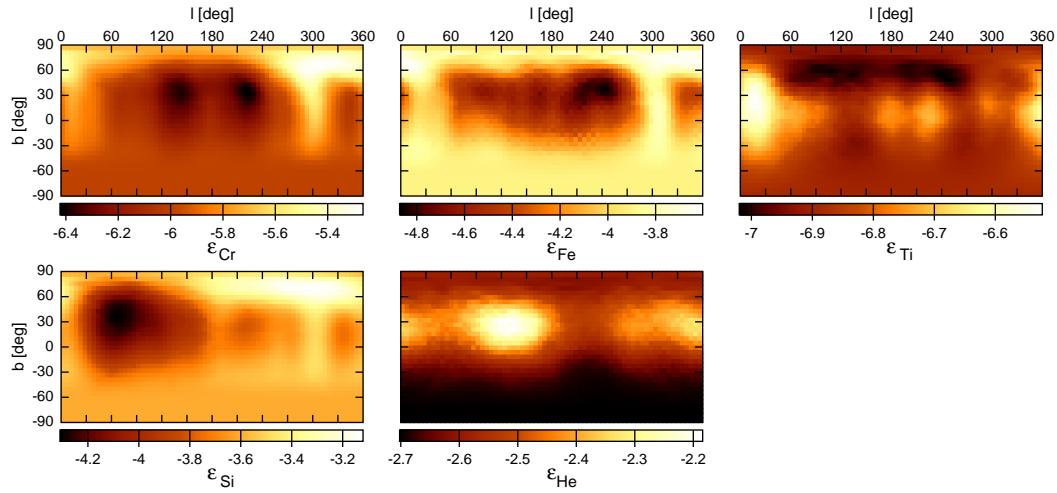


Figure 4.4: Maps showing chromium, iron, silicon, helium and titanium abundance in the photosphere of φ Draconis (source of the abundance maps: Kuschnig 1998).

increased abundance of several chemical elements, most notably silicon and iron. The magnetic field is of moderate strength – about 3 kG (Landstreet & Borra 1977).

φ Phe is not a single star, but a fairly complex multiple system (e.g., Tokovinin 2008). The exact structure of this system was thoroughly re-analyzed by Liška (2016). The result of the study is a system composed of a close binary Aa, Ab, accompanied by a more distant component B, with a possible distant component C. The analysis couldn't conclusively prove presence of a gravitational bond between the C component and the rest of the system, concluding the C component is most likely a separate object. The structure of the system is illustrated in Fig. 4.3. The work has also fixed the previously incorrectly measured value of the orbital period of the inner system Aab. The important physical characteristics of the star are listed in Table 4.1, along with the ranges of abundances for the mapped chemical elements, expressed as $\epsilon_{\text{el}} = \log(N_{\text{el}}/N_{\text{H}})$.

4.1.1 Abundance maps

Our input data for this work will be the abundance maps of helium, silicon, titanium, chromium and iron taken from Kuschnig (1998). The spectra on which the maps are based were obtained at Observatoire de Haute-Provence using the AURÉLIE spectrograph. The resolution in longitude and latitude of the maps is 68×33 surface elements. The maps are shown in Fig 4.4. Fig. 4.5 shows the distribution of the abundances of the individual elements as histograms. The maps indicate a strong underabundance of helium – even in the areas with the highest concentration the abundance is more than one dex lower compared with the solar photosphere. Silicon and iron both show quite strong variation in abundance. Chromium abundance also varies significantly, but the overall abundance is very low as well as the abundance of titanium. These two elements are therefore not likely to contribute significantly to the photometric variability of the star.

4.1.2 The model

To assess the emergent flux from any place at the surface of the star, we computed a grid of model atmospheres with different chemical composition. The list of abundances of the individual elements is shown in Table 4.2. Solar abundances are used for other chemical elements. Due to the

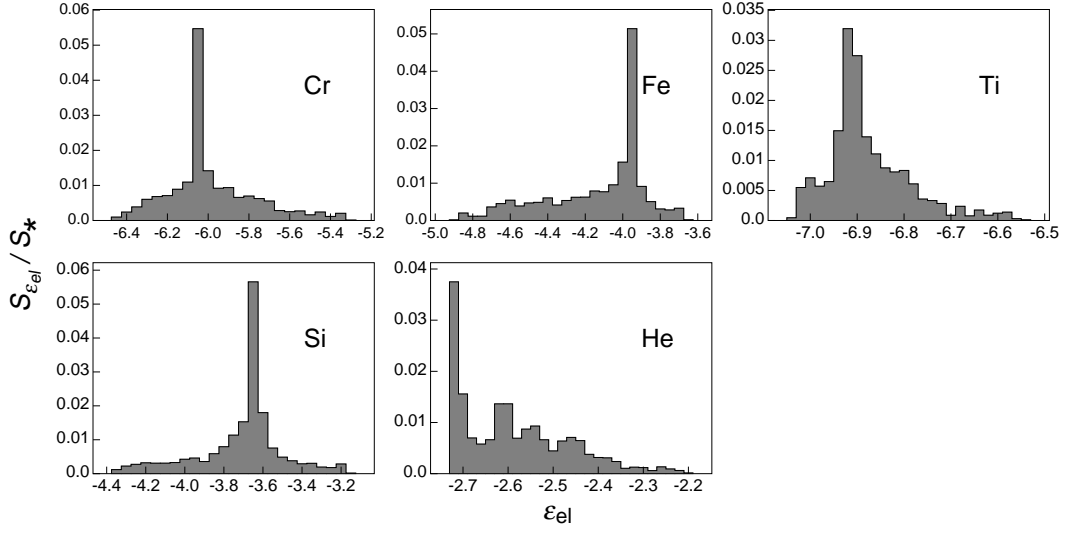


Figure 4.5: Histograms showing abundance distribution of chromium, iron, silicon, helium and titanium on the surface of φ Draconis (source of the abundance maps: Kuschnig 1998).

Table 4.2: Abundances used for model atmospheres.

Element	Abundances ϵ_{el}			
He	-2.56			
Si	-4.60	-4.10	-3.60	-3.10
Ti	-6.85			
Cr	-6.70	-6.20	-5.70	-5.20
Fe	-5.10	-4.60	-4.10	-3.60

very low abundance of helium and the low abundance and low variation of titanium, we decided to not take into account their surface distribution and only use a single fixed value for the model. This helped us reduce the total computation costs immensely, leaving us with only 64 model atmospheres to be computed. We used the TLUSTY code (Lanz & Hubeny 2007) to compute the models. For all the models we assumed LTE, because the approximation is adequate for modeling the photometric variability of CP stars (Krtićka et al. 2012). Also, a constant value of effective temperature and surface gravity was assumed for the entire surface of the star. For each model in the grid a synthetic spectrum was created using the SYNSPEC code. The atomic data used for the computation are adopted from Lanz & Hubeny (2007), Mendoza et al. (1995), Butler et al. (1993), Kurucz (1994), Nahar (1996, 1997), Bautista (1996), and Bautista & Pradhan (1997). The result is a set of angle-dependent specific intensities for a wavelength range of about 800–8000 Å. By numerically integrating the intensity passing through a simulated passband n over all wavelengths, we obtain intensities in various spectral regions for 20 equidistantly spaced values of $\mu = \cos \theta$:

$$I_n(\mu) = \sum_{\lambda_i} I(\lambda_i, \mu) \frac{\lambda_{i+1} - \lambda_{i-1}}{2} f_n(\lambda_i), \quad (4.1)$$

where $f_n(\lambda)$ is a response function of the passband n . We chose to simulate some of the passbands of the ten-color photometric system (Schoeneich et al. 1976), because photometric data for the star are available in it. The response functions for the individual passbands were approximated by

Table 4.3: Parameters of the Gaussian functions used to approximate the transmissivity of the filters of the used passbands of the ten-color photometric system.

Band	Central wavelength [Å]	Half-width [Å]
<i>U</i>	3450	200
<i>P</i>	3750	130
<i>X</i>	4050	110
<i>Y</i>	4620	130
<i>Z</i>	5160	105
<i>V</i>	5420	130
<i>HR</i>	6000	200
<i>S</i>	6470	50

Gaussian curves, the parameters of which are listed in Table 4.3. The value of the intensity at any point of the stellar surface can then be obtained by means of multilinear interpolation (and, in a few cases, extrapolation) between the nearest nodes within the grid. The total flux, observed by an astronomer on Earth at any rotational phase φ in a passband n can then be calculated by summing over the visible surface of the star (Mihalas 1978):

$$F_n(\varphi) = \sum_{i,j} I_{nij}(\mu_{ij}(\varphi)) \Delta l \Delta b \cos b_i \cos \mu_{ij}(\varphi) \frac{R_*^2}{D^2}, \quad [\mu_{ij}(\varphi) > 0], \quad (4.2)$$

where $I_{nij}(\mu_{ij}(\varphi))$ is the intensity in passband n for a local atmosphere at the surface element $[i, j]$, in the direction of the line of sight, $\mu_{ij}(\varphi)$ is the angle between the normal to the surface element $[i, j]$ and the line of sight at rotational phase φ , and l and b are the stellar longitude and latitude, respectively, R_* is the radius of the star, and D is the star's distance from Earth.

4.1.3 Influence of the chemical elements

The presence of heavier elements in the atmosphere of φ Draconis influences the structure of the atmosphere. The effects of the spectral energy redistribution can be seen in Fig. 4.6. The plot shows the effect of the individual elements on the temperature in the photosphere plotted against the Rosseland optical depth τ_{ross} . The upper plot shows the temperature in a model with roughly solar composition, while the lower plot represents the difference in temperature between the model atmosphere with enhanced abundance of each individual element and the reference model shown in the upper panel. It can be seen that iron has the greatest impact on the physical structure of the atmosphere.

Perhaps even more illustrative is the influence of the chemical composition on the radiation. The spectral energy redistribution for the case of φ Dra can be seen in Fig. 4.7. Here the upper plot shows the spectrum of flux emergent from a model atmosphere with solar chemical composition, whereas the lower plot displays the flux from model atmospheres with enhanced abundances of the individual elements. The spectra are smoothed by means of convolution with a Gaussian function with a dispersion of 10 Å. This removes the many spectral lines and thus makes the plot look less cluttered, increasing its readability.

The bound–bound transitions of iron, as well as bound–free transitions of silicon, absorb a significant portion of the spectral energy in the far-ultraviolet (far-UV) region of the spectrum,

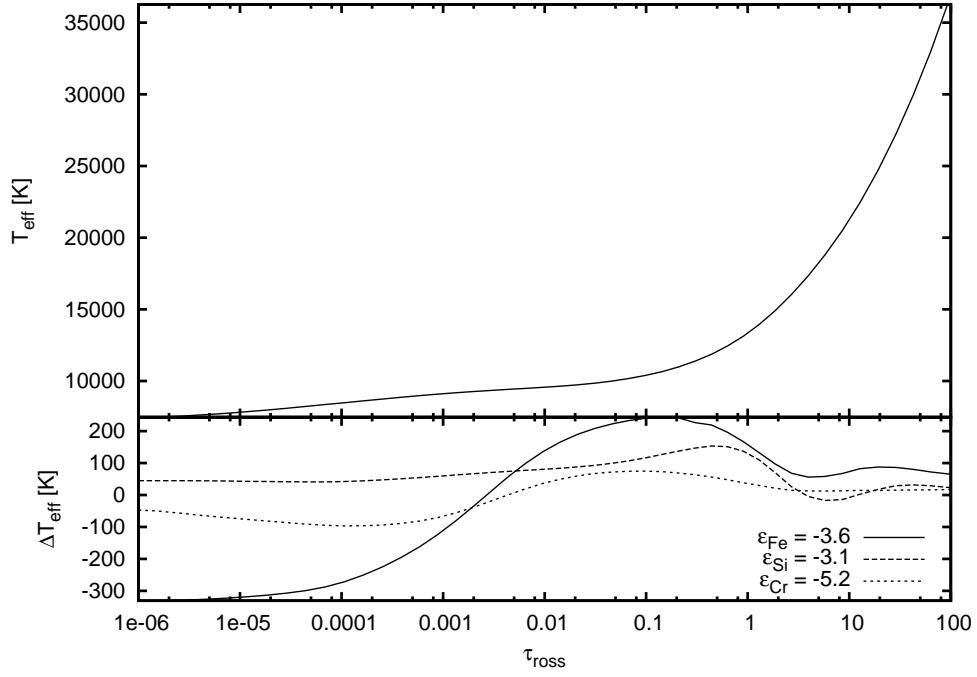


Figure 4.6: *Upper plot:* Temperature plotted against Rosseland optical depth τ_{ross} for a reference stellar atmosphere $\epsilon_{\text{Si}} = -4.6$, $\epsilon_{\text{Cr}} = -6.7$, and $\epsilon_{\text{Fe}} = -5.1$. *Lower plot:* Temperature in the model atmospheres with modified abundance of individual elements minus the temperature in the reference model.

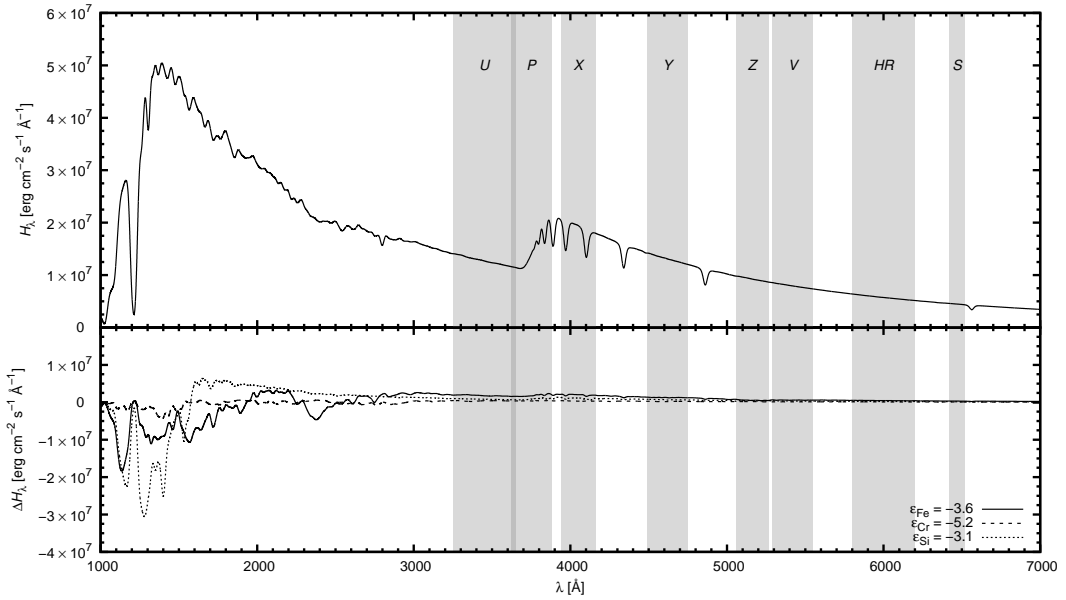


Figure 4.7: *Upper plot:* Emergent flux from a reference model atmosphere with $\epsilon_{\text{Si}} = -4.6$, $\epsilon_{\text{Cr}} = -6.7$, and $\epsilon_{\text{Fe}} = -5.1$. *Lower plot:* Emergent flux from the model atmospheres with modified abundance of individual elements minus the flux from the reference model. All fluxes were smoothed by a Gaussian filter with a dispersion of 10 \AA to show the changes in continuum, which are important for SED variability. The passbands of the ten-color photometric system are shown in the graph as grey areas. Image taken from Prvák et al. (2015).

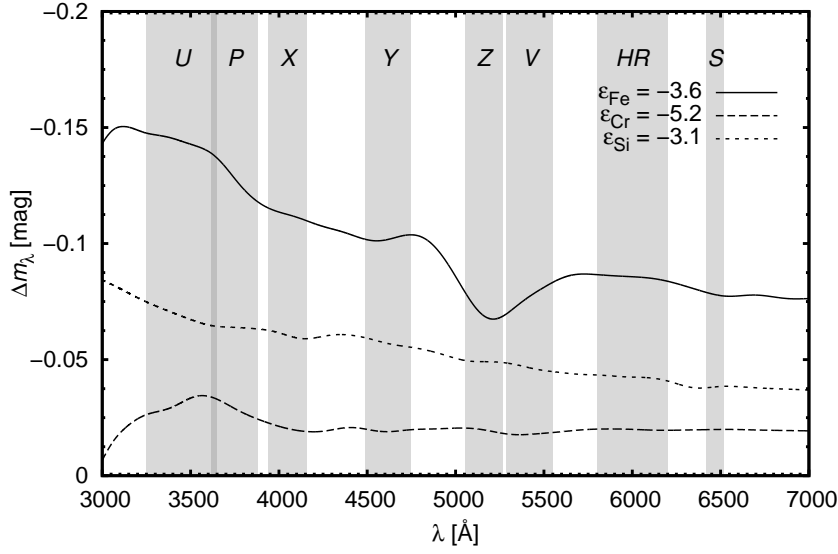


Figure 4.8: Magnitude of the emergent radiation from the model atmospheres with modified abundance of individual elements minus the reference model (see Fig. 4.7). All fluxes were smoothed by a Gaussian filter with a dispersion of 10 \AA to show the changes in continuum, which are important for SED variability. The passbands of the ten-color photometric system are shown in the graph as grey areas. Image was taken from Prvák et al. (2015).

especially at around $1100\text{--}1400 \text{ \AA}$. This is compensated by the increased emission in continuum, especially in the near-UV and in the visible parts of the spectrum. The influence of chromium is weak in comparison. The changes in the visible region are shown in more detail in Fig. 4.8, this time showing the difference in magnitude, rather than raw flux. Worth noting is the famous flux depression at about 5200 \AA caused by iron, the depth of which is commonly used as a measure of a star's chemical peculiarity (Kupka et al. 2004). This depression is also responsible for the decreased amplitude of photometric variability at this wavelength.

The emergent radiative flux from different parts of the visible stellar surface are displayed in Fig. 4.9. The star is portrayed as seen at four different rotational phases in three different passbands. The far-UV region at 1400 \AA displayed on the left panel is a region of strong absorption by both silicon and iron. Consequently, areas with overabundance of these elements appear as dark spots on the surface of the star. The middle panel, on the other hand, shows the surface of the star as viewed at a wavelength of approximately 2500 \AA . In this region significant absorption is caused by iron, but it is partially countered by increased continuum flux due to the influence of silicon. Areas overabundant in iron still show as dark here, but the areas with overabundance of silicon are bright. Because the distribution of the two elements across the stellar surface is different, the spots of iron and silicon partially overlap, the resulting flux depends on the relative ratio of their abundances at any given area of the stellar surface. The right panel shows the near-UV U passband of the ten-color photometric system. Both silicon and iron cause an increase of the continuum flux here, and the spots of their increased abundance both appear as bright areas (see Fig. 4.7).

4.1.4 Variability of φ Dra

The rotation of the star with photometric spots leads to apparent periodic light variability as seen by a static observer. Computing the emerged flux from the star at all rotational phases will yield a light curve describing this variability. Fig. 4.10 shows the amplitude of the light variation and

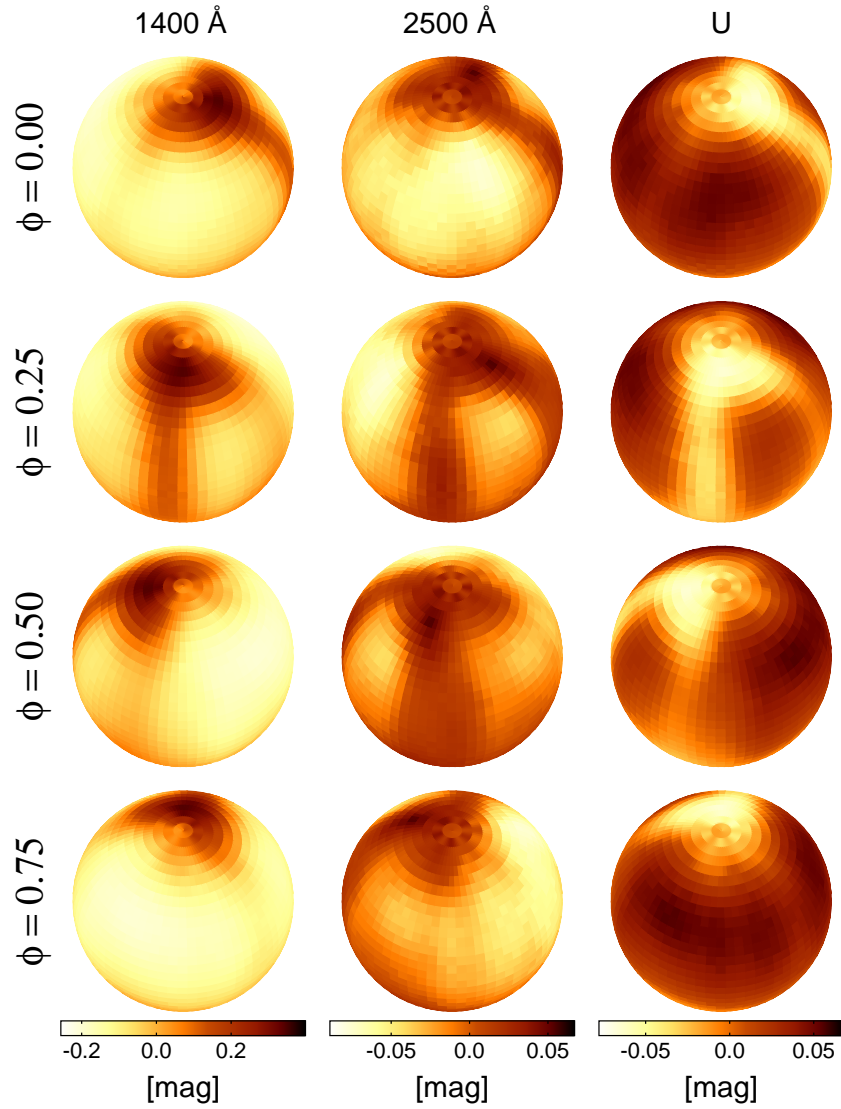


Figure 4.9: Emergent intensity from the surface of ϕ Dra across the visible stellar surface at different rotational phases passing through Gaussian passbands centered at 1400 Å (left panel), 2500 Å (middle panel), and the U band of the ten-color system (right panel). The intensities are expressed as $-2.5 \log(I/I_0)$, where I_0 is suitably chosen so that the resulting intensity averaged over the entire rotational period is zero. Figure data were taken from Prvák et al. (2015).

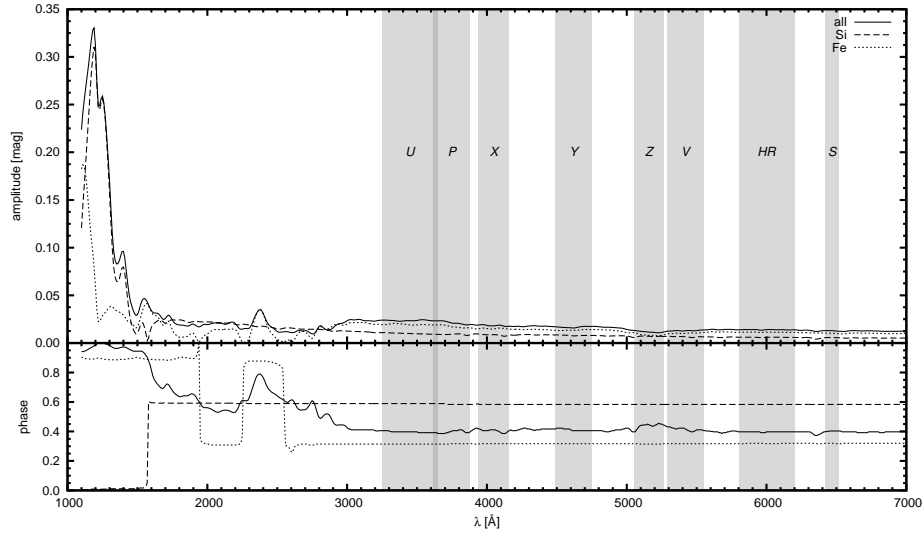


Figure 4.10: *Upper plot:* The dependence of the amplitude of light variation of φ Dra on wavelength. The amplitude here is defined as half of the difference between maximum and minimum magnitude of the star. *Lower plot:* The phase in which the light variations of φ Dra reach minimum. The image was taken from Prvák et al. (2015).

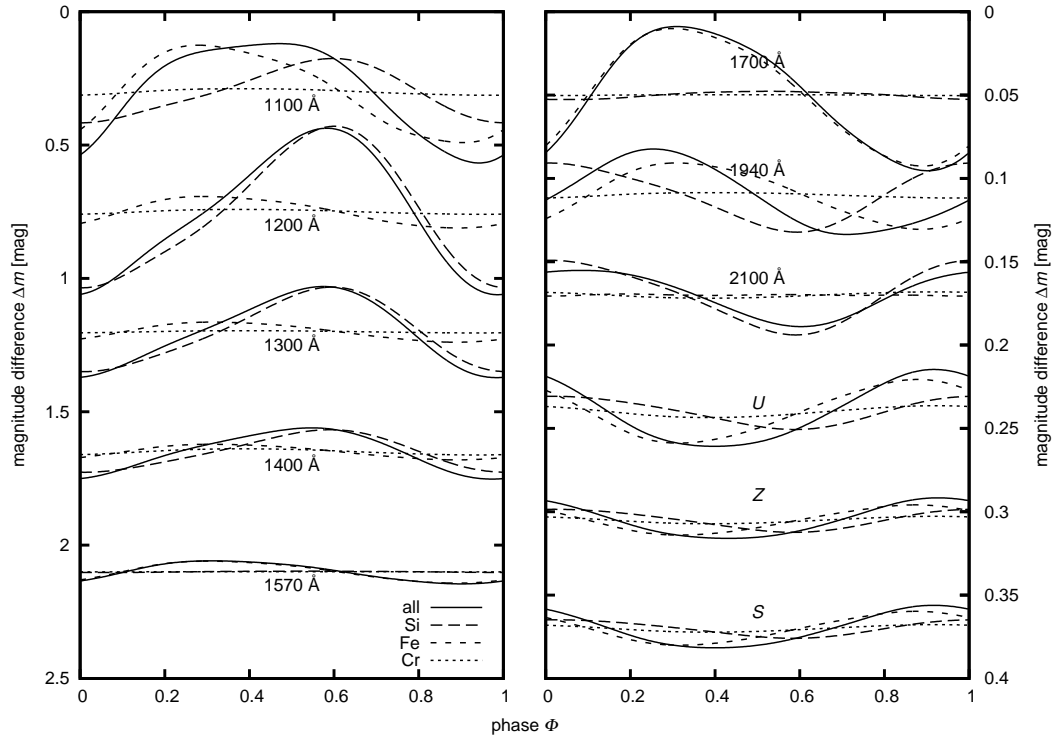


Figure 4.11: Light curves of φ Dra synthesized taking into account the abundance maps of the individual chemical elements separately, compared to the overall light variability (solid line) in several Gaussian passbands with the dispersion of 20 \AA in the UV and the U , Z , and S passbands of the ten-color photometric system. The light curves have been shifted vertically to better demonstrate the variability. The image was taken from Prvák et al. (2015).

Table 4.4: The list of φ Dra photometry used for the improvement of the ephemeris (see Eq. 4.5). N is the number of measurements in each set

Years	Type	N	$O-C_{\text{new}}$	Source
1974–5	10 col.	375	0.00095(55)	Musielok et al. (1980)
1991–2	Hp	104	-0.005(9)	ESA (1997)
1993	<i>BVRI</i>	194	0.006(14)	Prvák et al. (2015)

the position of the photometric minimum plotted against wavelength. Solid line in the plots describes the overall variability, whereas the dashed and dotted lines represent the variability of the star computed only taking into account the surface distribution of silicon and iron, respectively. In the lower plot we immediately notice the striking simplicity of the dependence for the chemical elements separately. The minimum of variability stays in the same place for extensive regions of the spectra, with only a few sudden "transitions" by 0.5 in phase, clearly separating the "absorbing" and "emitting" regions of the spectrum for the given element, where the corresponding light curves are in mutual antiphase. The simplicity of the light curves plotted for each chemical element in isolation contrasts strongly with the very complex shape of the composite curve representing the variability computed taking into account the influence of all the chemical elements simultaneously, which is governed by the actual ratio between the amplitudes of variability of the individual elements. The changes in the position of minimum are most significant in the ultraviolet part of the spectrum. In the visible region it varies only marginally. Chromium is not discussed here, since its contribution to the light variability is insignificant compared with that of silicon or iron.

The dependence of amplitudes is also interesting. Some authors have suggested existence of a so-called "null-wavelength region", between the "absorbing" and "emitting" parts of the spectrum, where the amplitude of the observed light variations is zero (e.g., Jamar 1977). As seen in the upper plot of Fig. 4.10, this is indeed true for the variability caused by each single chemical element in isolation. However it does not hold for the composite light curve computed taking into account all elements. Silicon and iron both have their transition wavelengths at different points in the spectrum, so wherever silicon does not contribute to the variability, iron has non-zero variations and vice-versa. We may therefore generalize this information and conclude, that whenever the variability of a CP star is caused by more than one chemical element, and the elements are distributed differently across the surface of the star, the "null-wavelength region" claim is invalid.

The Fig. 4.11 shows the synthesized light curves of φ Dra in several different passbands. The total light variations of the star are compared with the variability decomposed into components corresponding to the influence of each of the chemical elements separately. Again, chromium only contributes to the variability marginally. Considering iron and silicon individually, we notice the shape of the light curve for the given element remains constant at all wavelengths, differing from the other passbands only by a constant factor. However, the shape of the light curves for the two elements is significantly different. The resulting composite light curve, however, varies strongly in shape with wavelength, especially in the UV.

4.1.5 Photometric observations

To test the results of our model, we want to compare our synthetic light curves with the observed photometry of the star. The photometry by Musielok et al. (1980) in the ten-color system is suitable for this task. However, the huge time gap between these observations and the spectroscopy used by Kuschnig to derive the abundance maps requires the ephemeris of the star to be known very exactly if we want to combine the two sets of data successfully. To achieve this, we conducted our

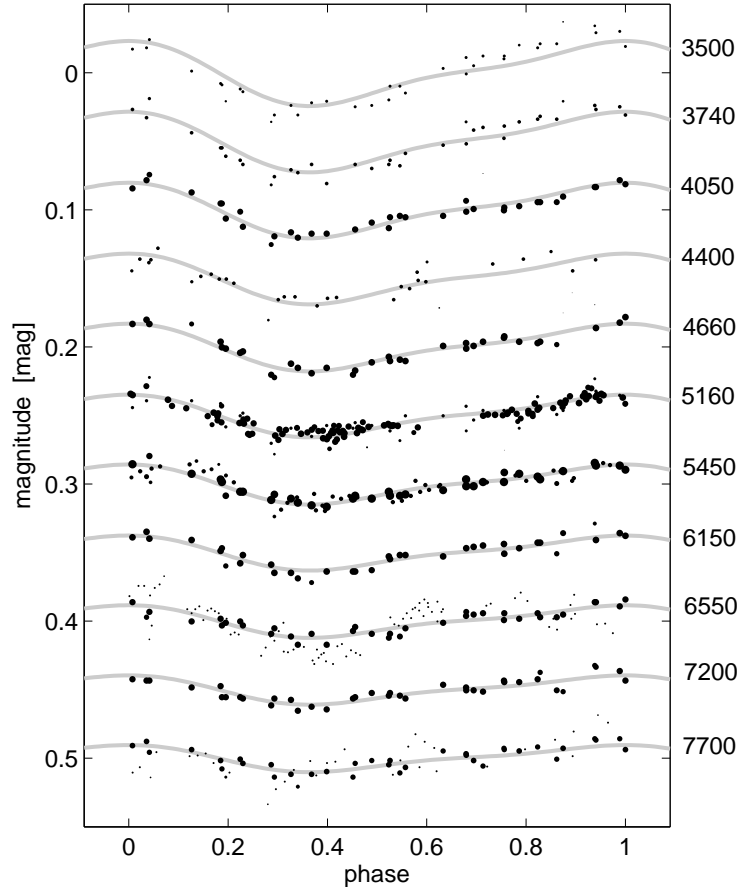


Figure 4.12: Light curves of φ Dra plotted in several photometric colors versus the new rotational period. The zero phase is put at the point of photometric maximum (Eq. 4.5). Gray full lines are the fits calculated using Eq. 4.3. Light curves are vertically shifted to better display the light variability. Area of the individual marks is proportional to the statistical weight of the corresponding data point. The numbers on the right-hand side of the plot indicate the central wavelengths (in Å) of the individual passbands for each light curve. The image was taken from Prvák et al. (2015).

own photometric observations of the star. The 194 measurements, somewhat complicated by the relatively high brightness of the target, were obtained at the Masaryk University Observatory and the Brno Observatory and Planetarium from May to July 2013 using a small refractor. In addition, we utilized photometry from the Hipparcos catalog (ESA 1997). Summary of all the observation sets, including the difference between the phases of the observed photometric minima and the photometric minima predicted using the assumed ephemeris ($O - C_{\text{new}}$) is given in Table 4.4.

Putting all the measurements together, we now have a solid base for period determination. We used a phenomenological function to fit the observations in the visible part of the spectrum:

$$m_j(t_i, \lambda_j) = \bar{m}_j + \left[A_1 + A_2 \left(\frac{545}{\lambda_j} - 1 \right) \right] F(\vartheta_i), \quad (4.3)$$

$$F(\vartheta, a_1, a_2) = \sqrt{1 - a_1^2 - a_2^2} \cos(2\pi\vartheta) + a_1 \cos(4\pi\vartheta) + \frac{2a_2}{\sqrt{5}} \left[\sin(2\pi\vartheta) - \frac{1}{2} \sin(4\pi\vartheta) \right], \quad (4.4)$$

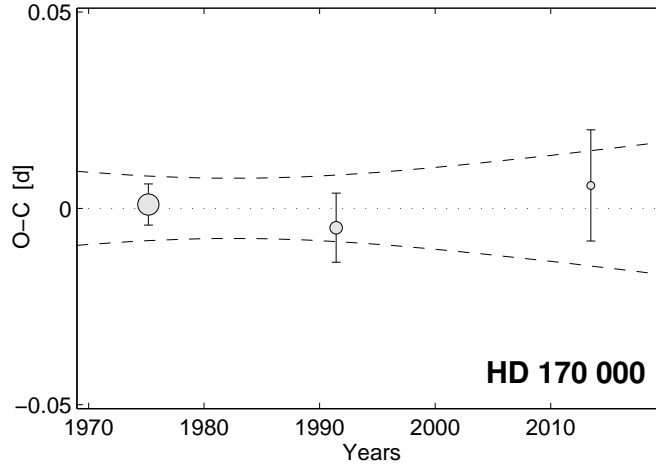


Figure 4.13: $O-C$ diagram for φ calculated versus a new linear ephemeris Eq. 4.5. Areas of the circles are proportional to the weight of the corresponding $O-C$ values. The dashed lines mark $1-\sigma$ uncertainty of a light curve maximum time prediction. The image was taken from Prvák et al. (2015).

where $m_j(\vartheta_i, \lambda_j)$ is a magnitude of the of the j -th data subset obtained in the photometric filter with the effective wavelength λ_j , t_i is JD_{hel} time of the i -th measurement, \bar{m}_j is the mean magnitude of the j -th data subset, A_1, A_2 are amplitudes expressed in magnitudes, ϑ is a phase function, $F(\vartheta, a_1, a_2)$ is a normalized second order harmonic polynomial with maximum at the phase $\varphi = \text{floor}(\vartheta) = 0$, a_1, a_2 , are the parameters, M_0 is the time of the basic extremum of the function $F(\vartheta)$, and P is the period. By means of the non-linear robust regression (see e.g. Mikulášek et al. 2003) we derived a new linear ephemeris for the star φ Dra:

$$JD_{\text{hel max}}(E) = 2445\,175.023(9) + 1.716500(2) \times E, \quad (4.5)$$

where E is an integer. The other model parameters are: $a_1 = 0.214(3)$, $a_2 = -0.477(3)$, $A_1 = -0.0134(3)$ mag, and $A_2 = -0.0149(3)$ mag. Fig. 4.12 shows the fit of the expression introduced in Eq. 4.3. The $O-C$ diagram with the new ephemeris in in Fig. 4.13.

4.1.6 Comparison of the synthetic light curves with observations

Now we can plot the modeled light curves together with the observations. Using the new ephemeris, the rotational phase of the model, based on the abundance maps, needs to be adjusted by a value of approximately 0.16. The plot is presented in Fig. 4.14. Now that the ephemeris has been fixed, the observations agree nicely in both shape and amplitude with the modeled variability of the star.

4.1.7 Discussion

There are several factors which may influence the accuracy of our results. The target is a component of a multiple system. Due to the individual stars' orbital motions, their distance from the solar system changes. This means light needs a different amount of time to reach us, distorting the observation times. This is usually referred to as the light-time effect (LiTE). Based on the analysis of the φ Dra system performed by Liška (2016), we determined the LiTE amplitude for the inner pair Aab to be about 104 s. This value is too small to significantly affect our results. The orbital

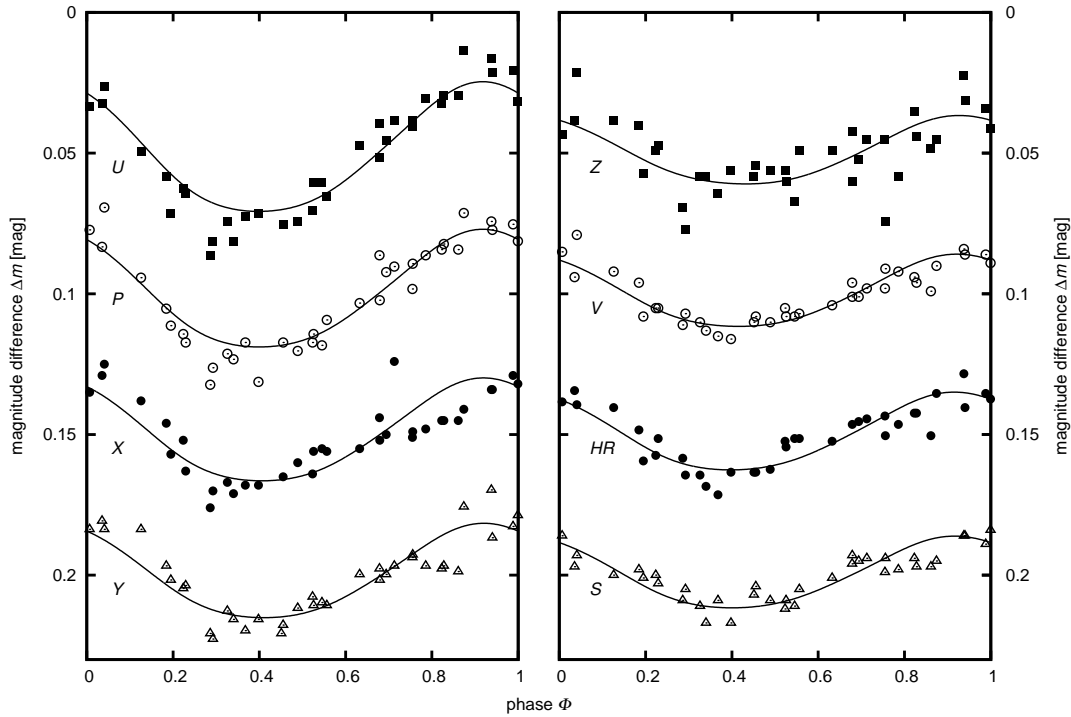


Figure 4.14: Light curves of ϕ Dra in the passbands *U*, *P*, *X*, *Y*, *Z*, *V*, *HR*, and *S* of the ten-color photometric system. Modeled curves (solid lines) are plotted together with the observational data taken from (Musielok et al. 1980). The light curves have been vertically shifted to better demonstrate the light variability. The image was taken from Prvák et al. (2015).

motion of the outer system AB presents LiTE amplitude of approximately 0.2 days, which is not negligible, but as the orbital period is 307 years, this is not a serious concern for observations on a time scale of just a few decades.

The B component's angular distance from the A pair is relatively low (about 1''), making it difficult to separate the objects during observation. For this reason, the B component may contribute to the total observed flux, affecting the accuracy of the photometry. The HIPPARCOS and Tycho catalogs (ESA 1997) indicate the B component is fainter than the A component by 1.445(10) mag in H_p , 1.50(1) mag in B_T , and by 1.42(1) mag in V_T . From this, we can estimate that about 21–23 % of the total observed flux comes from the B component. This makes us underestimate the amplitude of the variability, but it is probably partially compensated by the B component's effect on the line strengths and the derived chemical abundances.

Additionally, to reduce computational costs, the abundance mapping program only uses a mean stellar atmosphere for the entire surface of the star. While the synthetic spectra are modified based on the varying abundances of the individual elements and the line depths and profile shapes are updated to reflect the local chemical composition, the model atmosphere itself is not recomputed, and consequently the effect the modified abundance might have on the physical structure of the atmosphere is not taken into account. Some authors (e.g., Stift et al. 2012) have expressed concern about the relevance of abundance analyses performed in this way. As a result, the mapping techniques have been tested thoroughly (e.g., Kochukhov et al. 2012), with the conclusion that, with the exception of a few rare cases with extreme overabundances of heavier elements, the approximation is adequate and the results of the Doppler imaging are sufficiently accurate. The good agreement of our results with the observations also support this conclusion.

Table 4.5: Parameters and abundance ranges expressed as $\log(N/N_{\text{H}})$ of the star φ Phe adopted from Korhonen et al. (2013). Solar abundance for each element taken from Grevesse & Sauval (1998) is given in parentheses.

Effective temperature T_{eff}	10600 K
Surface gravity $\log g$ [cgs]	3.79
Rotational period P	9.531 d
Rotational velocity projection $v \sin i$	13.5 km s ⁻¹
inclination i	53°
Titanium abundance	$-6.8 < \varepsilon_{\text{Ti}} < -6.3$ (-6.98)
Chromium abundance	$-6.1 < \varepsilon_{\text{Ti}} < -5.8$ (-6.33)
Strontium abundance	$-7.6 < \varepsilon_{\text{Ti}} < -6.6$ (-9.06)
Yttrium abundance	$-8.5 < \varepsilon_{\text{Y}} < -6.3$ (-9.78)

4.2 φ Phoenicis

Another object suitable for analysis is the HgMn star φ Phe (HD 11753, HR 558). This kind of CP stars typically suffer from strong overabundance of chemical elements such as Hg, Ga, Mn, Y, Sr, Cr, and others (see e.g., Castelli & Hubrig 2004; Monier et al. 2015). What differentiates them from the other categories of spotted CP stars is the absence of a strong and stable global magnetic field (e.g., Hubrig et al. 2012; Kochukhov et al. 2013; Catanzaro et al. 2016). The exact mechanism, creating and maintaining the chemical abnormalities in the atmospheres of these stars, is still not entirely understood. It is suspected to be the result of slow rotation, the relative stability of the surface layers due to the lack of a subsurface convective zone, and atomic diffusion (Michaud et al. 1976). More often than other types of stars, the HgMn stars are found in binary systems (Budaj 1996; Schöller et al. 2010).

These stars often exhibit line profile variations that are usually explained by the oblique rotator model and Doppler imaging is employed to derive abundance maps (Briquet et al. 2010; Makaganiuk et al. 2011). However, observational evidence of photometric variability is extremely rare, as the amplitude of such variations is expected to be extremely weak (Paunzen et al. 2018). However, there's been evidence of secular evolution of the abundance structures on the surface of HgMn stars (Kochukhov et al. 2007; Hubrig et al. 2010).

The parameters of the star φ Phe are listed in Table 4.5. Compared to φ Dra, its surface temperature is lower and the rotational period is considerably longer. There is a strong overabundance of strontium and yttrium, both increased by more than 3 dex compared to the solar composition. The star is a component of a binary system (Pourbaix et al. 2013). We intend to analyze the photometric variability of this star using the same method as in the case of φ Dra. We also want to study how the secular evolution of the surface abundance structures affects the variability. The work has been presented in Prvák et al. (2018).

4.2.1 Abundance maps

The series of abundance maps we used for light curve synthesis are taken from Korhonen et al. (2013) and Briquet et al. (2010). The data consists of four sets, derived from spectroscopy using the CORALIE spectrograph in October 2000, December 2000, August 2009, and January 2010, respectively. Each set contains maps of chromium, titanium, strontium, and yttrium. The maps are displayed in Fig. 4.15. The spatial resolution of the maps is 80 points in longitude and 40 points in latitude. Differences between the individual sets are easily visible for each element. Fig. 4.16

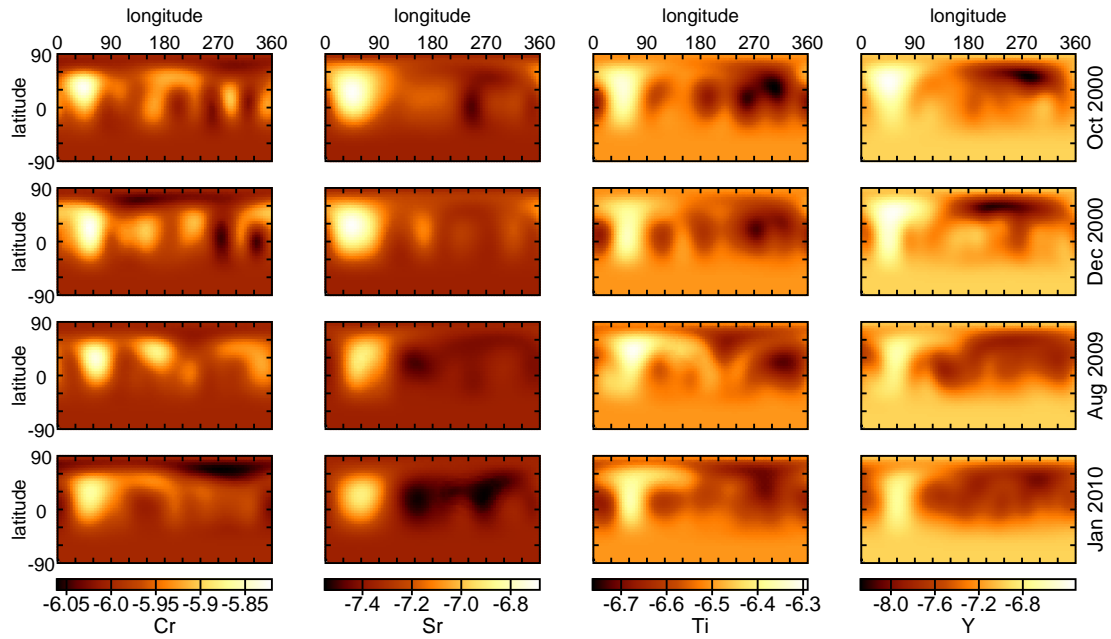


Figure 4.15: Maps showing the titanium, chromium, strontium and yttrium abundance in the photosphere of the star φ Phoenicis in the individual observing epochs (source of abundance maps: Korhonen et al. 2013).

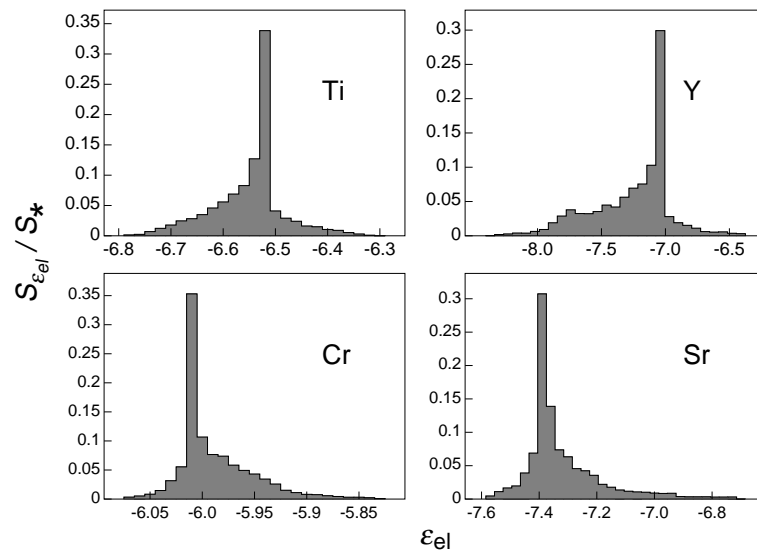


Figure 4.16: Histograms showing abundance distribution of chromium, titanium, strontium and yttrium on the surface of φ Phoenicis (source of abundance maps: Korhonen et al. (2013)).

Table 4.6: Abundances used for the grid of model atmospheres of φ Phe.

Element	Abundances ε_{el}				
Cr	-6.1	-5.8			
Ti	-6.8	-6.3			
Sr	-7.6	-7.1	-6.6		
Y	-8.3	-7.8	-7.3	-6.8	-6.3

shows histograms of the distribution of the four chemical elements across the surface of the star averaged for all sets.

4.2.2 The model

We used the same technique as in the case of φ Dra. In order to model the photometric variability of the star, we generated a grid of model atmospheres. Because the effective temperature is lower this time, we used the ATLAS12 code (Kurucz 1996; Castelli 2005). The full list of the grid abundances used for all the mapped elements is given in Table 4.6. This time we needed to compute 60 model atmospheres. The atomic data used for the models come partially from Lanz & Hubeny (2007), and partially – in the case of strontium and yttrium lines – from the Kurucz website¹. Because the SYNSPEC program is compatible with model atmospheres produced by ATLAS, we used it to synthesize corresponding spectra in the same format as for φ Dra. Using the Equation 4.1, we obtained angle-dependent intensities in the selected passbands. Integrating over entire visible disc, as indicated by Equation 4.2, yields the total flux observed by a static distant observer at any rotational phase. Doing so separately for each one of the four sets of observations, and for different rotational phases, we obtain the light curves.

4.2.3 Effect of chemical composition

The model atmospheres we computed allow us to evaluate the influence of the enhanced chemical abundances on the structure of the atmosphere. This is well visible in Fig. 4.17, which displays the temperature in a model atmosphere with chemical composition corresponding to the lower limits of the abundances at the surface of the star. The bottom part of the plot shows the relative difference in temperature of the model atmospheres computed with the chemical abundance of the individual elements significantly increased, corresponding to the composition of the most abundant spots observed in the star. The influence of titanium, chromium, and yttrium here is comparable, strontium affects the physical properties of the atmosphere very weakly. Still, the deviation from the structure of an atmosphere with solar composition is much smaller than in the case of φ Dra (see Fig. 4.6).

Fig. 4.18 shows the changes of the spectral energy distribution (SED) in the atmosphere of φ Phe. The lower part of the plot shows the difference in the emergent flux caused by the presence of titanium, chromium, strontium and yttrium relative to the reference model shown at the top. Strong absorption in lines of the four elements causes significant decrease of the emergent flux in the far-UV region. Chromium also causes absorption in the region between 2600 Å and 3000 Å, and an increase in the continuum in the near-UV and in the visible part of the spectrum, especially between 3500 Å and 4500 Å, where it is partially countered by absorption in lines of yttrium and, to a lesser degree, titanium. The significance of strontium is again negligible.

¹<http://kurucz.harvard.edu>

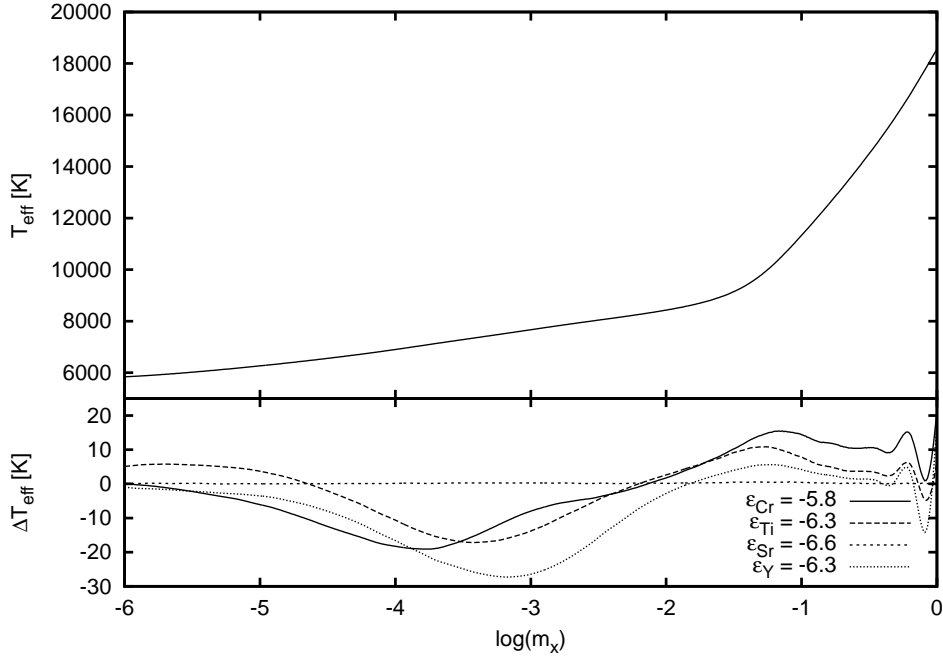


Figure 4.17: *Upper plot:* Temperature versus column mass density $m_x = \int_x^\infty \rho dx'$ for a reference stellar atmosphere with $\varepsilon_{\text{Cr}} = -6.1$, $\varepsilon_{\text{Ti}} = -6.8$, $\varepsilon_{\text{Sr}} = -7.6$, and $\varepsilon_{\text{Y}} = -8.3$. *Lower plot:* Temperature in the model atmospheres with modified abundance of individual elements minus the temperature in the reference model.

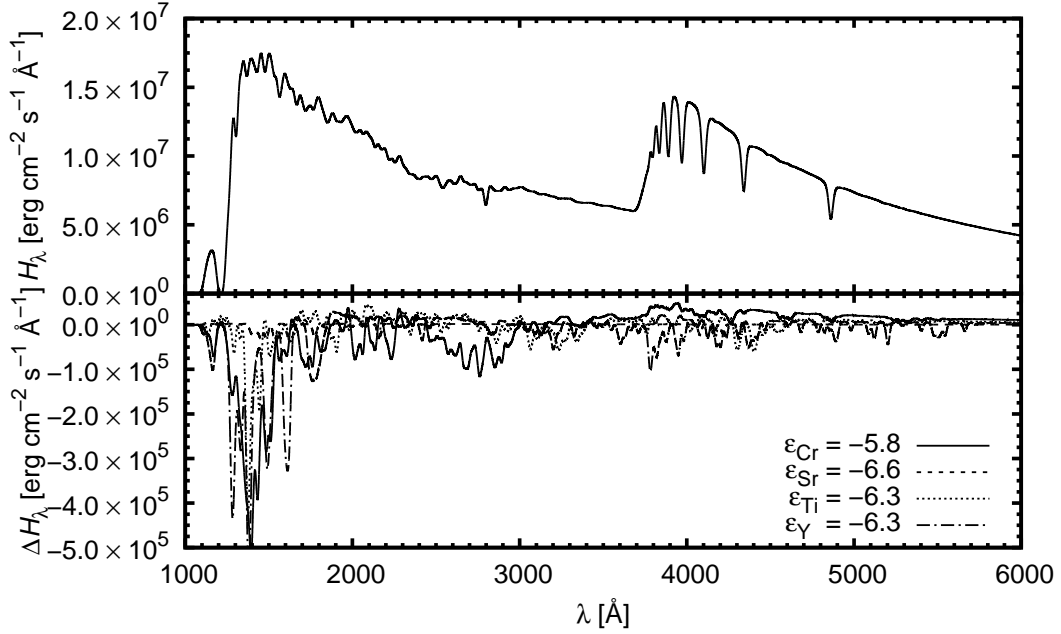


Figure 4.18: *Upper plot:* Emergent intensity from a reference model atmosphere for a model stellar atmosphere with $\varepsilon_{\text{Cr}} = -6.1$, $\varepsilon_{\text{Ti}} = -6.8$, $\varepsilon_{\text{Sr}} = -7.6$, and $\varepsilon_{\text{Y}} = -8.3$. *Lower plot:* Emergent intensity from the model atmospheres with modified abundance of individual elements minus the flux from the reference model. All fluxes were smoothed by a Gaussian filter with a dispersion of 10 \AA to show the changes in continuum, which are important for SED variability.

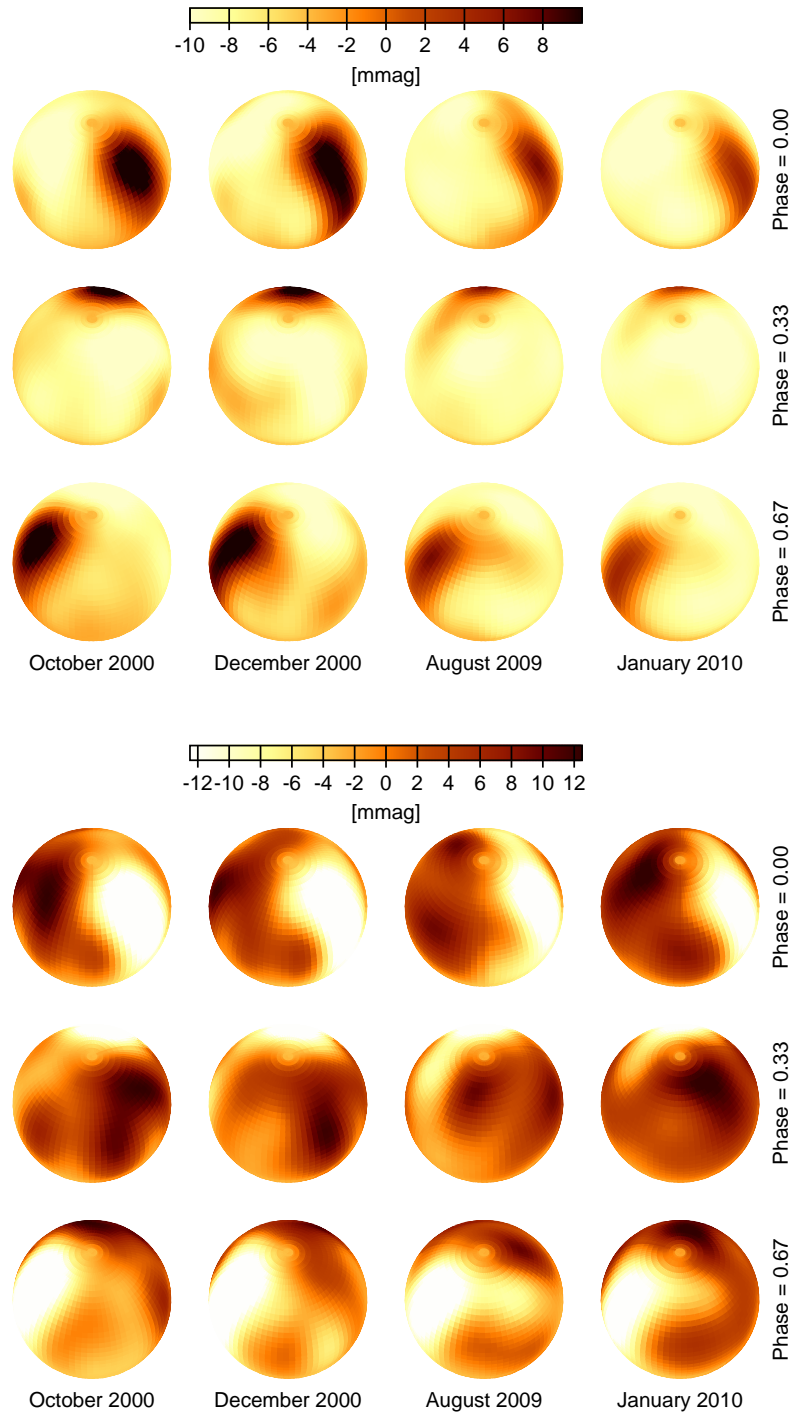


Figure 4.19: *Upper panel:* Emergent intensity from the surface of ϕ Phe across the visible stellar surface at different rotational phases and based on the individual sets of maps passing through a Gaussian passband centered at 1300 \AA . *Lower panel:* The same as the upper panel, but for a passband centered at a wavelength of 4050 \AA . The intensities are expressed as $-2.5 \log(I/I_0)$, where I_0 is suitably chosen so that the resulting intensity averaged over the entire rotational period is zero.

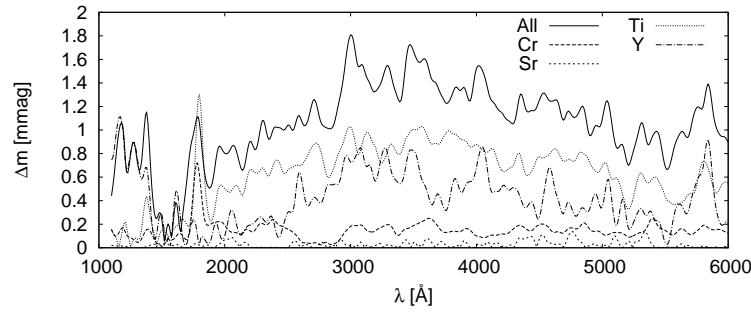


Figure 4.20: The dependence of the amplitude of light variation of φ Phe on wavelength. The amplitude here is defined as half of the difference between the maximum and minimum magnitude of the star.

The total emergent flux observed at two different wavelengths, 1400 Å and 4050 Å, and different rotational phases is displayed in Fig. 4.19. The spots with increased abundances are visible as dark areas in the UV spectrum due to absorption in lines, whereas the same spots are bright in the visible range due to the increased continuum flux. Slight changes in the flux distribution are noticeable between the individual datasets, corresponding to the secular evolution of the abundance structures.

4.2.4 Light variations of φ Phe

Integrating the intensity over the visible stellar disc at different rotational phases we obtain light curves of the star. Fig. 4.20 shows the dependence of the total amplitude of the light variations on wavelength, as well as the amplitude components related to the contribution of the individual chemical elements. As the absorption by the elements considered in this case occurs mainly in lines, which are scattered across the entire spectrum, the variability depends very strongly on wavelength, especially in narrow-band passbands. The amplitude is largest in the visible part of the spectrum, especially between 3000 Å and 4000 Å. Titanium and yttrium have the most significant impact on the light. The influence of chromium is only noticeable in the region around 1800 Å, effect of strontium is negligible at all wavelengths.

The actual light curves can be seen in Fig. 4.21, depicting both the total light variability and the variability decomposed by the individual chemical elements, all based on the maps from January 2010. The light curves in the far-UV are in anti-phase to those in the near-UV and in the visible. The shape of the light curves remains roughly the same throughout the visible range of the spectrum, owing to the quite similar distribution of both titanium and yttrium across the surface of the star.

Fig. 4.22 shows the light curves computed using different sets of abundance maps. The differences between the curves reflect the secular evolution of abundance spots during the time from October 2000 to January 2010. These changes in the distribution of chemical elements result in a visible change in the light variability. This includes a change of the position of the light maximum, which in visible region ranges between 0.77 and 0.83 in phase, as well as a change in the total amplitude, which varies by about 10–50 % in all parts of the UV and optical spectrum. The amplitude of photometric variability was largest in December 2000, whereas the lowest amplitude occurred in August 2009. The largest changes in amplitude are observed at 1700 Å and at 6450 Å. The shape of the curve also changes significantly. The changes of the shape of the light curve are caused mainly by changes in the abundance structures of titanium.

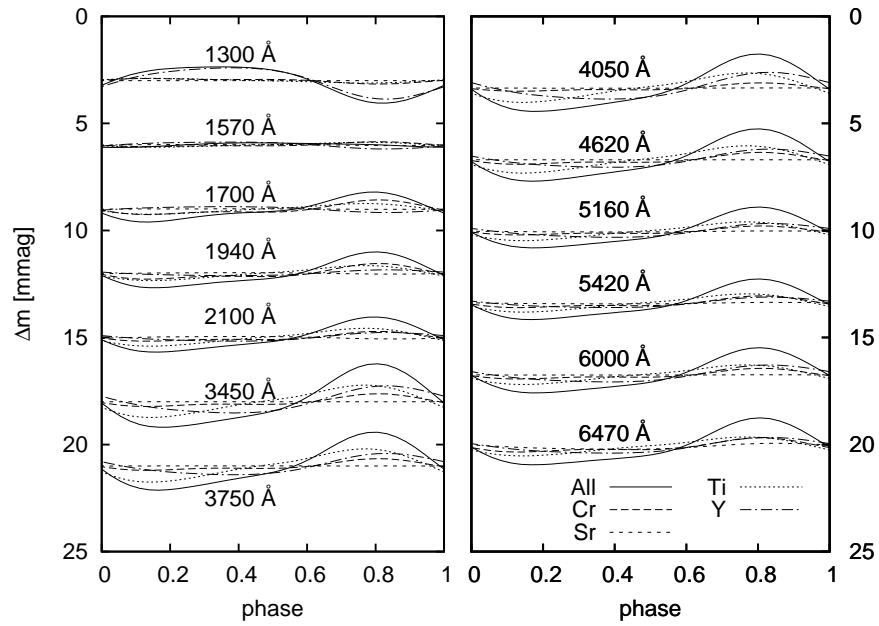


Figure 4.21: Light curves of ϕ Phe synthesized taking into account the abundance maps of the individual chemical elements separately, compared to the overall light variability (solid line) in several Gaussian passbands with the dispersion of 20 Å in the UV and selected passbands of the ten-color photometric system (see Table 4.3). The light curves have been shifted vertically to better demonstrate the variability.

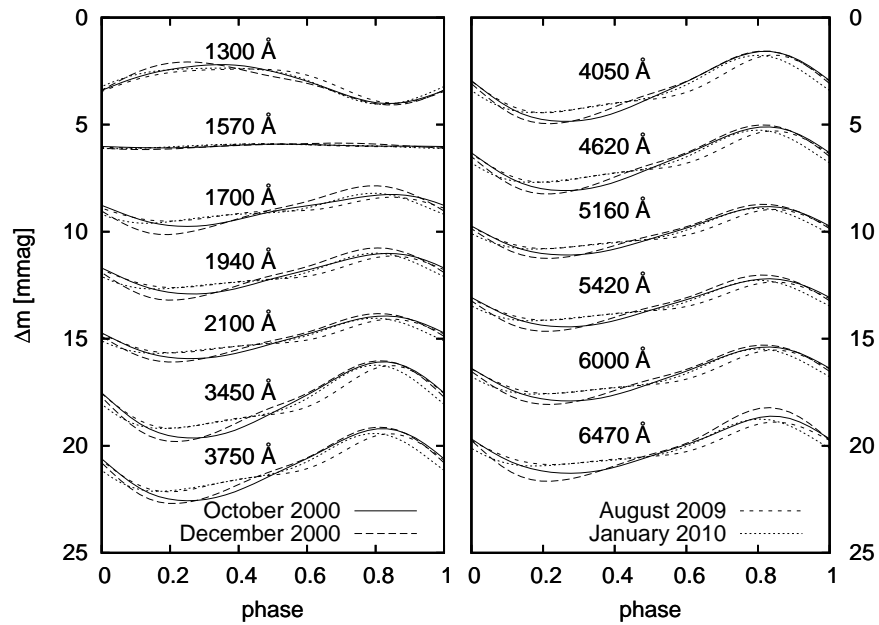


Figure 4.22: Light curves of ϕ Phe at different times corresponding to the individual sets of abundance maps in several Gaussian passbands with the dispersion of 20 Å in the UV and selected passbands of the ten-color photometric system (see Table 4.3). The light curves have been shifted vertically to better demonstrate the variability.

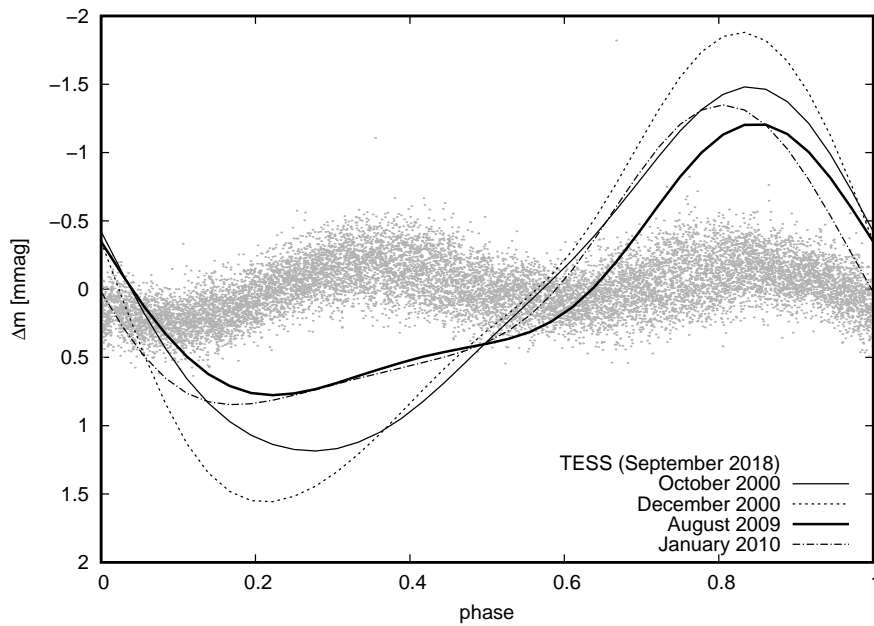


Figure 4.23: Light curve of φ Phe in the S passband (6470 \AA) of the ten-color photometric system at different times corresponding to the individual sets of abundance maps (lines) compared with the photometric variability observed by TESS (grey dots).

4.2.5 Comparison with observations

Once we obtain the theoretical light curve of a star, it is highly desirable to compare the results with observations. This, however, is not simple in the case of HgMn stars such as φ Phe, because the relative changes in the brightness are very small. If we conduct the observations with ground-based instruments, the unpredictable small motion of air within the Earth's atmosphere will make it very difficult for us to reach sufficient precision to reliably detect such weak photometric variability. While space-borne instruments, on the other hand, are not limited in precision by the atmosphere, the sensitivity of their detectors prohibits us from observing such bright targets. So, we could then only observe faint targets, but then we wouldn't be able to obtain the abundance maps, because the surface abundance analysis requires high-resolution, high signal-to-noise spectra, which can only be obtained for relatively bright targets.

Fortunately for us, the *Transiting Exoplanet Survey Satellite* (TESS) (Ricker et al. 2015) has recently provided us the opportunity to obtain space-borne photometry of φ Phe, precise enough to uncover the light variation we predicted. Fig. 4.23 compares our models with the TESS observations. The photometry was obtained in September 2018, during an observing run spanning over a total period of about 30 days, of which 21 days of usable photometry was left after reduction and detrending. These are plotted against the modeled variability based on the individual data sets in the S band of the ten-color system. The TESS observations, on the other hand, are conducted in a much wider passband, spanning far into the infrared part of the spectrum, although the S band lies within the wavelength range of the TESS passband. Also, there are no abundance maps available for the same epoch, so the comparison with the photometry is only qualitative. The amplitude of the photometric variations is smaller than the models predicted, but the difference is comparable to the difference between the individual sets of maps.

4.2.6 Discussion

The variability predicted by our work does not very precisely match the observed variability of the star. This can be caused by several factors. First, the photometric passband S of the ten-color system, which we used for comparison, differs somewhat from the TESS photometric band. It is likely that, in the TESS's significantly wider passband positioned farther in the red and infrared region, the observed amplitude of the light variation would be lower.

Also, the predicted changes in the variability of the star are comparable with the discrepancy between the model and the observations. This discrepancy could therefore also be (partially) explained by the ongoing secular evolution of the spots between the years 2010 and 2018. Additionally, apart from the four elements considered in our models, there can be others contributing to the photometric variability of the star, the abundance maps of which are not available.

The star φ Phe is a part of a binary system. This could also have influenced the accuracy of the models and photometry. However, considering the very long orbital period of the system – 1126.11 days (Korhonen et al. 2013), the short observation runs couldn't have been seriously affected.

Our models indicate that the phase of photometric minimum / maximum is changing. However, the rotational period of the star has never been established with certainty (see e.g., Korhonen et al. 2013). The incorrectly determined period wouldn't have affected the very short observation runs for each of the data sets or the observation by TESS. It could introduce a phase shift between the individual datasets, making a false impression of the phase of the maximum and minimum changing with the secular evolution of the spots. Conversely, if the phase of the extrema is actually changing, this may complicate the determination of the rotational period.

The light variability of the star is caused mainly by the increased abundance of yttrium. This element is not usually considered in the model atmospheres and the corresponding atomic data have therefore not received much attention. The low accuracy and incompleteness of the atomic data may also affect the comparison of the model and the observations.

4.3 Conclusions

We have used Doppler abundance maps to predict photometric variability of two stars: a silicon Ap star φ Dra and the HgMn star φ Phe. We have determined new linear ephemeris for φ Dra. There are no signs of a change of the rotational period.

We showed the variability of both stars can be explained by the model of the oblique rotator. The inhomogeneous horizontal distribution of heavier elements in the surface layers of the stars causes spectral energy redistribution, which together with the rotation of the star leads to periodic changes in the observed flux. In the case of φ Dra, the SED changes are caused by bound–free transitions of silicon and bound–bound transitions of iron, whereas absorption in lines of yttrium and titanium is responsible for the variability of φ Phe.

We have shown how the shape of the light curve and the position of the photometric minimum depends on wavelength, especially in the case of φ Dra. This is the consequence of superposition of multiple components of the variability, each of them caused by presence of a different chemical element, with different physical properties and different distribution over the stellar surface.

The resulting light curves were compared with photometric observations. The good agreement in the case of φ Dra can serve as a verification of the fundamental concepts of abundance analysis and spectroscopy. It helps prove the reliability of the atomic data of silicon and iron, the theory of stellar atmospheres. It also shows that the LTE approximation is sufficient for modeling of the variability of Ap stars. Unfortunately, the lack of photometric data in the UV region prevents us from verifying the correctness of our model and studying the variability in the part of spectrum, where

the most interesting processes take place, and where the largest amplitude of the light variations is expected.

In the case of φ Phe, we have also studied the secular evolution of the abundance structures, and their influence on the light variability of the star. We have shown that the change in the shape of the spots causes changes in the shape and amplitude of the light curves in all passbands in the ultraviolet and the visible parts of the spectrum. Unfortunately, the large time gap between the photometry and the abundance maps do not allow an objective comparison; the predicted variability is larger compared with the photometric measurements. This could be a result of the secular evolution, or the inaccuracy of the atomic data. Therefore, the results can serve as a motivation for further studies and improvements of the line transition data of yttrium and other less common chemical elements.

Chapter 5

Obtaining brightness maps from photometry

In some cases it may be useful to be able to tell something about the distribution of heavier elements across the surface of a star, even if the detailed spectroscopy is not available. This may be needed in cases where the star in question is just too faint, or when we're trying to spot possible candidates for Doppler mapping in a large sets of light curves. Not having the convenience of studying the line profile variations, can we still derive some information about the surface abundance structures?

A difference from the Doppler mapping, using the line profile variation, is that in the method we are going to use here, the light curves are typically observed in photometrical passbands much broader than a typical width of a spectral line; often we only have observations in one passband. This means practically no spectral resolution. In other words, we can make no (or very little) conclusions about the chemical composition of the stellar atmosphere. Unlike the Doppler imaging, which seeks the relation between the chemical properties of the local atmospheres and the observed spectral line variations solving a physical and a geometrical problem at the same time, here we can only find the connection between the distribution of the local emergent flux and the observed light variability. This means we separate the two problems and only solve the question of geometry, without concerning ourselves (or being able to tell) which physical processes are responsible for the variation of the emergent flux.

Let us define the problem in the following way: given an observed light variability, can we find such a distribution of emergent flux across the surface of the star that, integrated over the visible phases at each rotational phase, will yield a light curve matching the observed light variations?

Subdividing the surface of the star with radius R_* into small surface elements of size Δb in latitude and Δl in longitude (see Fig. 5.2), each such element contributes a flux $\Delta H(l, b, \varphi)$ through a given passband observed at distance D during the rotational period of the star equal to

$$\Delta H(l, b, \varphi) = \begin{cases} I(l, b) \Delta b \Delta l \cos b \mu(l, b, \varphi) \lambda_D(\mu) R_*^2 / D^2, & \text{where } \mu(l, b, \varphi) > 0; \\ 0 & \text{otherwise} \end{cases} \quad (5.1)$$

where $I(l, b)$ is the emergent intensity from the surface element in the direction of the normal to this surface element, $\mu(l, b, \varphi) = \cos b \cos(l + 2\pi\varphi) \sin i - \sin b \cos i$ is the cosine of the angle between the normal to the surface at position (l, b) at rotational phase φ and the line of sight, $\lambda_D(\mu)$ is the limb darkening function, and i is the inclination of the star. The total observed emergent flux from the star at any rotational phase can then be expressed as a sum of contributions of all the surface elements:

$$\Delta H(\varphi) = \sum_{l, b} H(l, b, \varphi). \quad (5.2)$$

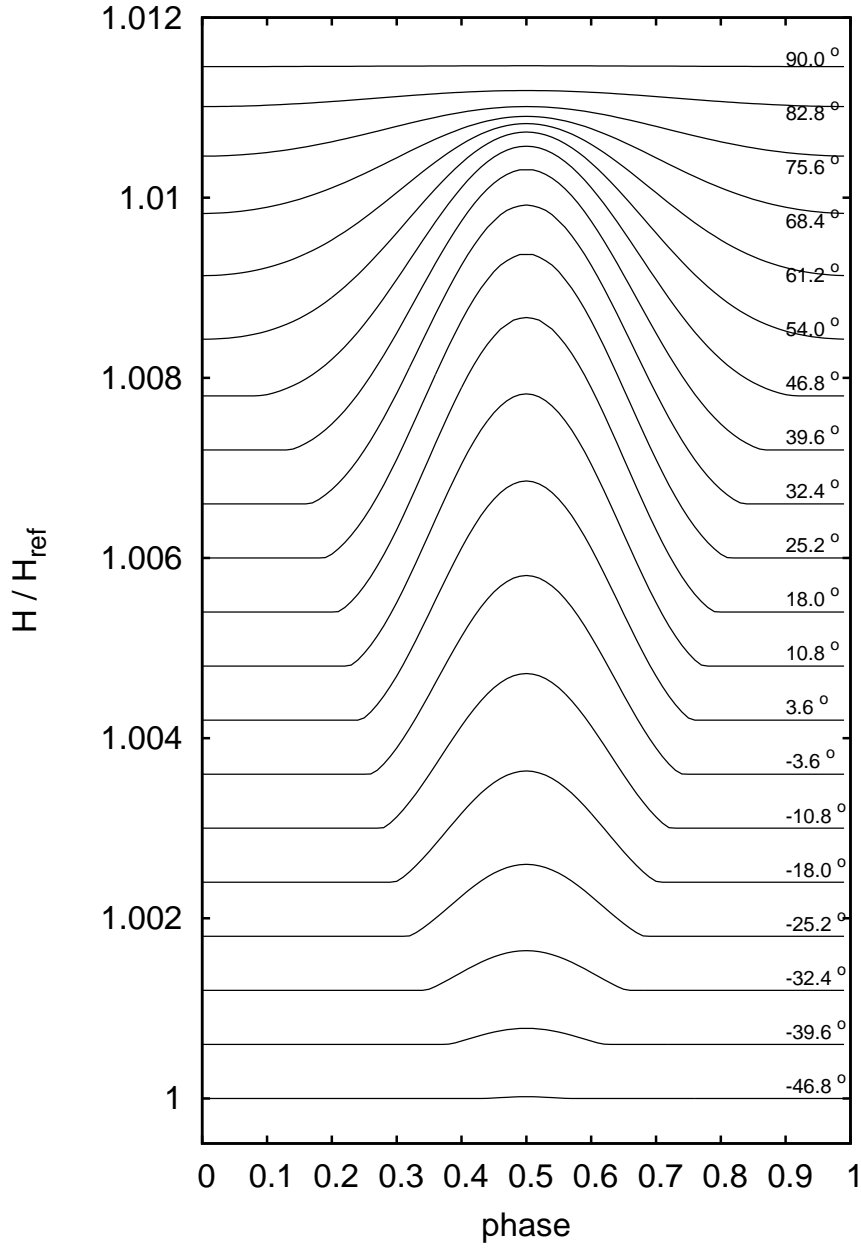


Figure 5.1: Light curves of an artificial star with inclination $i = 50^\circ$ and a single bright spot of size $\Delta b \times \Delta l$. The individual curves show the cases of the spot being positioned at different stellar latitudes. The corresponding latitudes of the geometric center of the spot for each curve is shown on the right-hand side of the plot. The limb darkening was computed using the Eq. 5.4 assuming the values $c_1 = 0.724, c_2 = 0.062$. The curves have been vertically shifted for better readability.

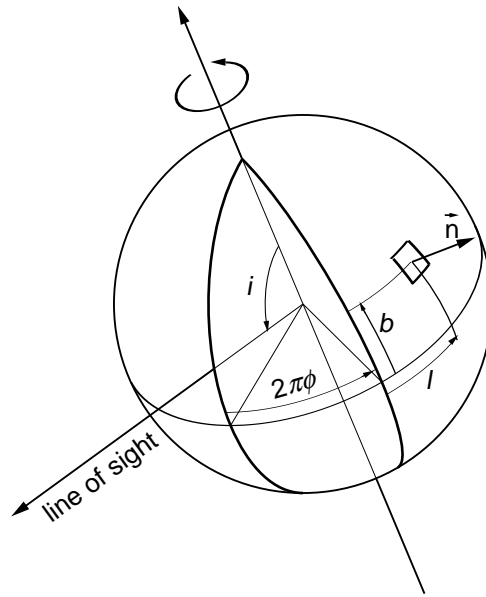
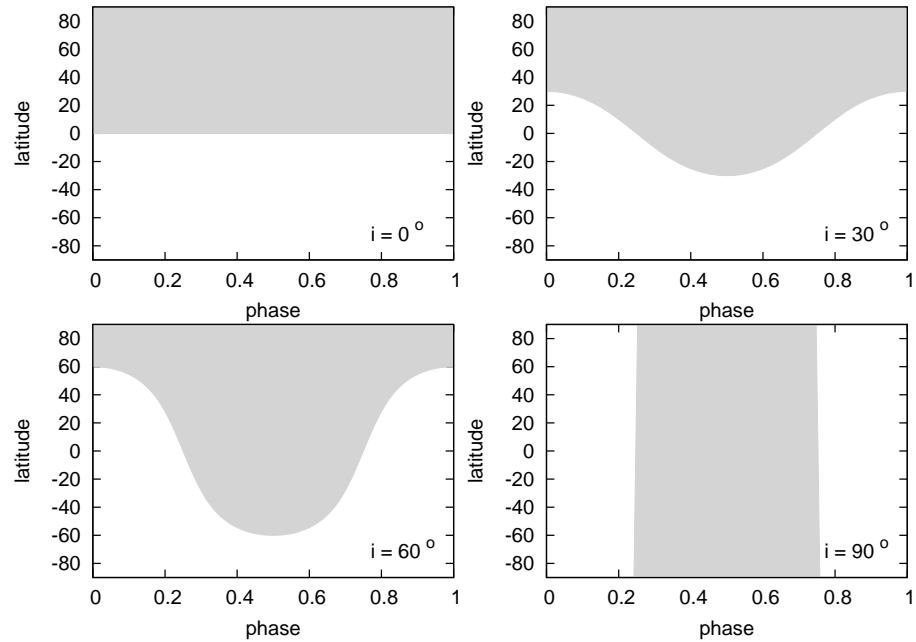


Figure 5.2: Geometrical description of the stellar surface.

Figure 5.3: Visibility of a spot with longitude $l = 180^\circ$ during a rotational period for different inclinations (0° , 30° , 60° , and 90°) plotted against the stellar latitudes. Gray areas mark the phases during which the spot is visible.

We may consider an artificial star with the emergent flux being constant everywhere over its surface except for a single surface element positioned at stellar latitude b and longitude l . Theoretical light curves of such a star for $l = 180^\circ$ and different values of b are shown in Fig. 5.1. All such light curves are of the form

$$\Delta H(b, l, \varphi) = a \cos b \mu(b, l, \varphi) I_D(\mu(b, l, \varphi)), \quad (5.3)$$

where a is a constant. Elements with latitudes $b > 90^\circ - i$ are always visible. Conversely, the elements with latitudes $b < i^\circ$ are never visible. Obviously the change of longitude of the spot will cause a phase shift of the resulting curve.

The curves produced assuming different latitudes of the spot differ significantly in shape. For the spots near the northern pole the contribution to the amplitude of the light variability is small due to low variation of the position of the spot relative to the observer, as well as the small area of the element. The produced brightness variation profile is very wide. Moving the spot towards the south we get increasing amplitude, while the width of the profile will gradually decrease, as the spot with lower latitude will remain in the visible part of the stellar disc for a shorter duration. The elements on the southern hemisphere, especially those near $b = i^\circ$, are only visible for a very short part of the rotational period. Therefore their signature on the light curve is very narrow and the corresponding amplitude of variability will be very small, because their path over the visible stellar disc will keep them near the very edge of the visible part of the star, resulting in significantly reduced area projection and strong limb darkening.

The visibility of a surface element during the rotation of the star is shown in Fig. 5.3. In the extreme case of inclination $i = 90^\circ$ the shape of the light curve depends only very weakly on the spot latitude (through the limb darkening) and we have no way to determine the distribution of the intensity in latitude. The other extreme case, $i = 0^\circ$, is also undesirable, because then we can observe no variability at all. For this reason the stars with inclination in the middle between the two extremes are most suitable for analysis.

These properties of the variability are important for our analysis. If we could assume the variability of the star is caused by a single spot of infinitesimal size on the surface of the star, and if we also knew the inclination of this star, we would be able to tell the position of such spot on the stellar surface with precision limited only by the accuracy of the photometric measurements. Of course, in the real universe the surface of a star is a two-dimensional space with arbitrary distribution of emergent flux. The light curve components related to the individual surface elements are not linearly independent, i.e. there exist non-trivial linear combinations of these light curve components that produce no variability. The only information we have about the star – the light curve – is one-dimensional. This leaves us with infinitely many solutions to the Eq. 5.2.

For example, any distribution of flux that is only a function of the latitude (i.e. does not depend on longitude) will cause no variability whatsoever. We may therefore find infinitely many functions $f(b)$ which, added to any surface intensity map, will not change the resulting light curve.

Or, if we consider an infinitesimal surface element e_1 of the size $db \times dl$ at coordinates (b_0, l_0) , the light curve profile caused by this element can not be exactly matched (with the exception of the extreme cases of inclination discussed above) by any other single surface element. We could, however, find a linear combination $f(l)$ of the relatively narrower light curve profiles of the surface elements forming an infinitesimal stripe of size $db \times 2\Delta l$ at latitude $(b_0 - \varepsilon)$ and longitudes $(l_0 - \Delta l; l_0 + \Delta l)$ south of the element e_1 , such that

$$\int_{l_0 - \Delta l}^{l_0 + \Delta l} f(l) dH(b_0 - \varepsilon, l, \varphi) dl = dH(b_0, l_0, \varphi),$$

that is the sum of these contributions will match the variability profile of the surface element e_1 . Here ΔI corresponds to the difference of the half-widths of the light curve profiles of infinitesimal surface elements at latitudes l_0 and $l_0 - \varepsilon$ (see Fig. 5.3).

5.1 Numeric solution

As shown above, mathematically there is an infinite number of solutions to the problem. From the physical perspective, we will, however, impose some constraints on the solution. The emergent flux at any point of the stellar surface is, for obvious reasons, a positive number. Also, for the visible region of the light spectrum, we will assume bright spots on a dark background, i.e. the emergent intensity $I(b, l) = I_0 + \Delta I(b, l)$, $\Delta I(b, l) > 0$. We will also limit the maximum brightness of the spots, because we wouldn't be able to physically justify huge variations in brightness on the surface of a star. For the same reason we will also prefer continuous, smooth, and simple solutions over unnecessarily complex surface structures. These assumption will strongly reduce the amount of possible solutions, but we are still not able to tell with certainty that the solution we found is the correct one.

To find a solution to the problem discussed above, we wrote a simple program. It is a quick implementation of rather naive “*genetic*” algorithm, based on trial and error (see Goldberg 1989, for an overview of genetic algorithms). The method can be described in the following way:

- Input: a desired (observed) light curve
- Start with a set of empty maps (i.e. constant intensity, no spots).
- Repeat until sufficient agreement with the observed light curve has been reached:
 - Synthesize light curves for all the maps in the set.
 - Evaluate all maps based on some pre-defined criteria (see below).
 - Create a new empty set of maps.
 - Push the N_1 best candidates from the previous iteration to the new set.
 - Generate N_2 new maps derived from the best N_1 candidates of the previous iterations by making *a single minor random change* to the map.
 - Generate N_3 new maps derived from the best N_1 candidates of the previous iterations by making *a single major random change* to the map. The difference between the minor and major changes is in the amplitude of the change of the modified quantity.
 - Generate N_4 new maps derived from the best N_1 candidates of the previous iterations by making *two major random changes* to the map.
 - Generate N_5 new maps derived from the best N_1 candidates of the previous iterations by making *three major random changes* to the map.
 - Add N_6 new completely random maps of complexity comparable to the maps in the current iteration.

For our computations, we adopted the values $N_1 = 5$, $N_2 = N_3 = N_4 = N_5 = N_6 = 15$.

- Output: the resulting intensity map which achieved the best match to the evaluation criteria.

The map is defined as a two dimensional grid of $n_b \times n_l$ elements. All of them are initially assumed to have the same default emergent intensity (in the direction of the normal to the element) I_0 . To

these maps we can add “spots”. By spots in the context of our computation, we will mean any single surface element with coordinate indices b_i and l_j the emergent intensity of which is increased by a positive value $\Delta I(i, j)$. The observed light curves are normalized in such a way that the median of the intensities is equal to one. Intensities in the maps are expressed as $(I_0 + \Delta I)/I_0$.

We synthesize the light curve by summing the intensities over the entire visible surface of the star for n_φ rotational phases using the equations 5.1 and 5.2. For the limb darkening function, we use

$$l_D(\mu) = 1 - c_1(1.0 - \mu) - c_2\mu \log \mu, \quad (5.4)$$

where c_1 and c_2 are empirical constants appropriate for a given spectral class (van Hamme 1993) and are assumed to be constant over the stellar surface. We subdivide each surface element into $n_s \times n_s$ subelements (we used $n_s = 2$ for our computations) for flux summation to achieve a smoother and more accurate light curve.

Each map is then tested against some criteria. The way we formulate them are very important for the behavior of the code and the qualities of the resulting maps. The most obvious and important one is that the light curve obtained from the given map should be as close to the input light curve as possible. Therefore we want to minimize the sum of squares of differences between the observed emergent flux $H_{\text{obs}}(\varphi_i)$ and the modelled emergent flux $H_{\text{mod}}(\varphi_i)$ at each rotational phase φ_i

$$S = \sum_{i=1}^{n_\varphi} (H_{\text{obs}}(\varphi_i) - H_{\text{mod}}(\varphi_i))^2. \quad (5.5)$$

Also, we want to favour smooth continuous distributions of flux, so we added an expression to penalize sharp edges, analogically to the way regularization is used in Doppler imaging (see e.g., Narayan & Nityananda 1986, for a detailed discussion of regularization):

$$R = \sum_{i=1}^{n_b-1} \sum_{j=1}^{n_l} \left[(H(b_{i+1}, l_j) - H(b_i, l_j))^2 + (H(b_i, l_{j+1}) - H(b_i, l_j))^2 / \cos^2(b_i) \right], \quad (5.6)$$

where $H(b_i, n_l + 1) = H(b_i, 1)$. The cosine of the latitude in the second term helps preventing sharp variations of the emergent flux around the northern pole of the star. Each map then gets a final “score”.

$$m_s = S + a_R R, \quad (5.7)$$

where a_R is a regularization parameter controlling the smoothness of the maps.

At each iteration we then generate a new set of maps. The best candidates from the previous iteration are left unchanged, so that they are not lost in case the current iteration fails to produce better candidates. Most of the maps, however, are derived from these maps by introducing one or more random changes. These changes include:

- introducing a new spot (weight: 10),
- changing latitude of an existing spot (weight: 50),
- changing longitude of an existing spot (weight: 50),
- changing intensity of an existing spot (weight: 400),
- grow an existing spot (i.e. create a new spot adjacent to an existing spot, weight: 500).

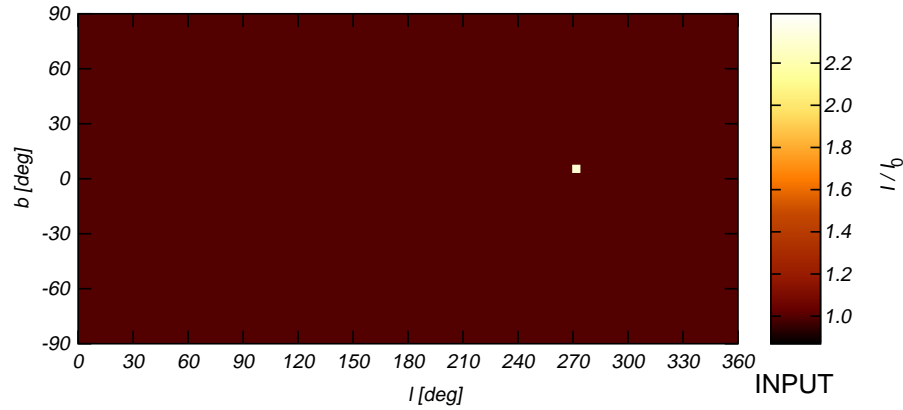


Figure 5.4: An intensity map with a single spot used as input for testing the code. The emergent intensity from the spot is about $2.3 \times I_0$.

These changes all have a statistical weight associated with them to make some of them more likely to happen than others. The probability of adding a new spot, for instance, is set to a low value to make the code search for the best positions and intensities of the existing spots before introducing a new one. As the number of spots on a map increases, the number of possible changes to a map grows rapidly and the rate of convergence decreases. The amplitude of the random changes decreases proportionally to m_S . We also add a few completely randomized maps to the set. This helps to prevent the computation from getting stuck in a local minimum of m_S .

5.2 Testing the code

We may test our code by computing flux maps of artificial stars, the flux distribution of which we already know. We simply make up a flux map, then synthesize the corresponding light curve, and finally let the code derive the map and then we check whether we get back the map we started with. Let's start with a simple task: a flux map with a single small bright spot ($I_{\max}/I_0 = 1.3$). The map is shown in Fig. 5.4.

Let us first investigate the effect of the regularization parameter a_R . Fig. 5.5 shows the intensity maps computed with different values of the regularization parameter and the fits of the light curves based on these maps. Setting $a_R = 0$ results in rather sharply defined structures. Since the maximum intensity the code was allowed to use was significantly lower than the intensity of the input map, the code had to compensate by creating a larger spot. In order to not widen the light curve profile, the code used the elements to the south of the original spot location, where the narrower light curve signatures of the surface elements allowed it to use a wider range of longitudes to fill in the intensity required to fit the desired light curve. This results in a triangular structure that can be seen on the top panel of the figure. Such structures in the maps usually indicate that the constrain put on the maximum intensity has been set too low.

With increasing value of a_R the result becomes much smoother. However, if we set a_R too high, smoothness of the map becomes a priority at the cost of good agreement with the input light curve. This can be seen on the two bottom panels. We can also see that the high value of the regularization parameter naturally limits the maximum intensity used in the maps, due to the fact that increasing intensity at any given surface element to a value significantly higher than that of the adjacent surface elements increases the resulting term R of the Eq. 5.6 so much that it can no longer be compensated by the decrease of the term S resulting from the better fit of the light curve.

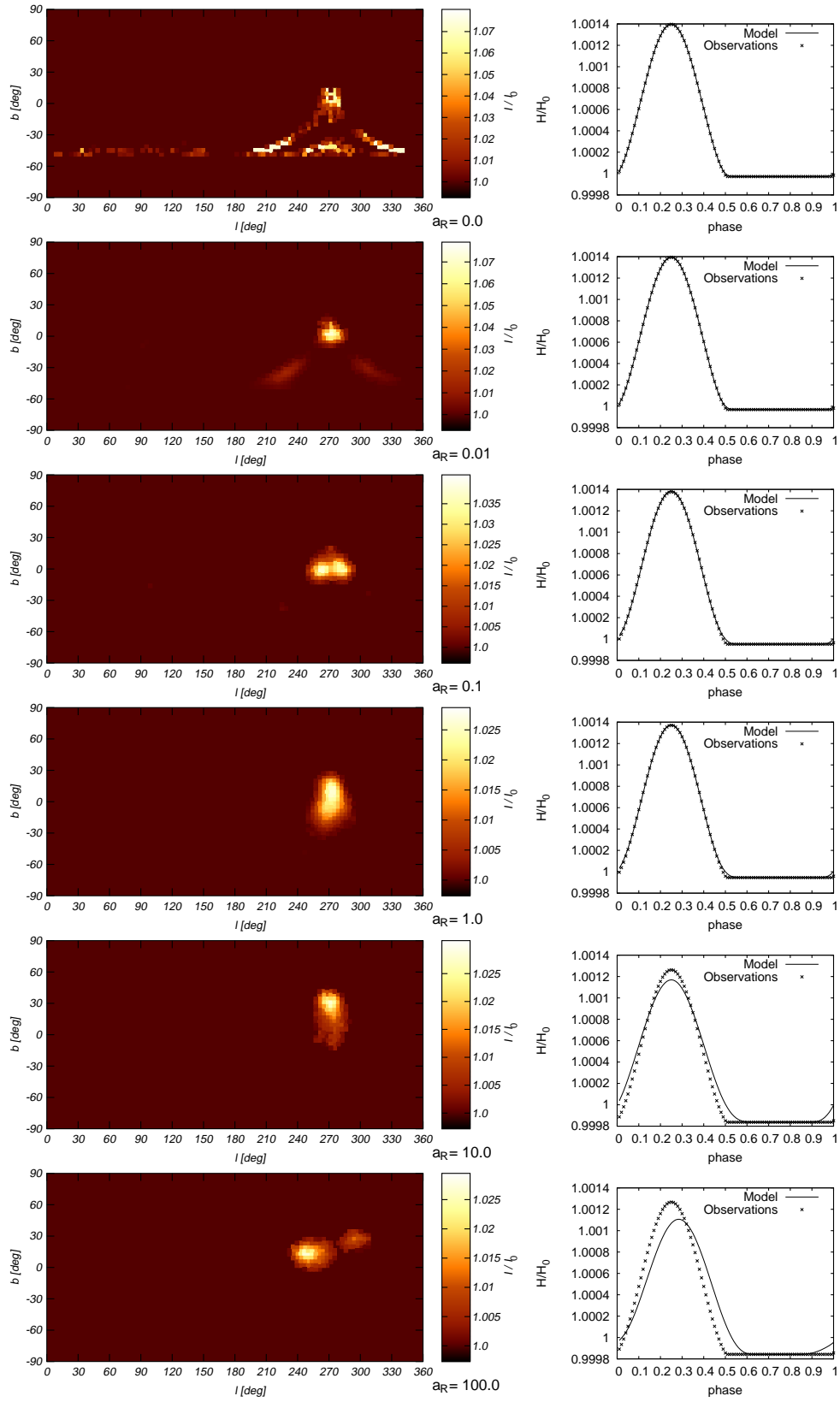


Figure 5.5: A set of intensity maps generated with inclination $i = 50^\circ$, maximum intensity $\Delta I_{\max}/I_0 = 0.1$, and different values of the regularization parameter a_R (left panel) and the corresponding light curve fit (right panel). The solid line shows the light curve resulting from the flux distribution of the derived map. The points denote the input light curve. H_0 is the median of the flux values in the observed light curve.

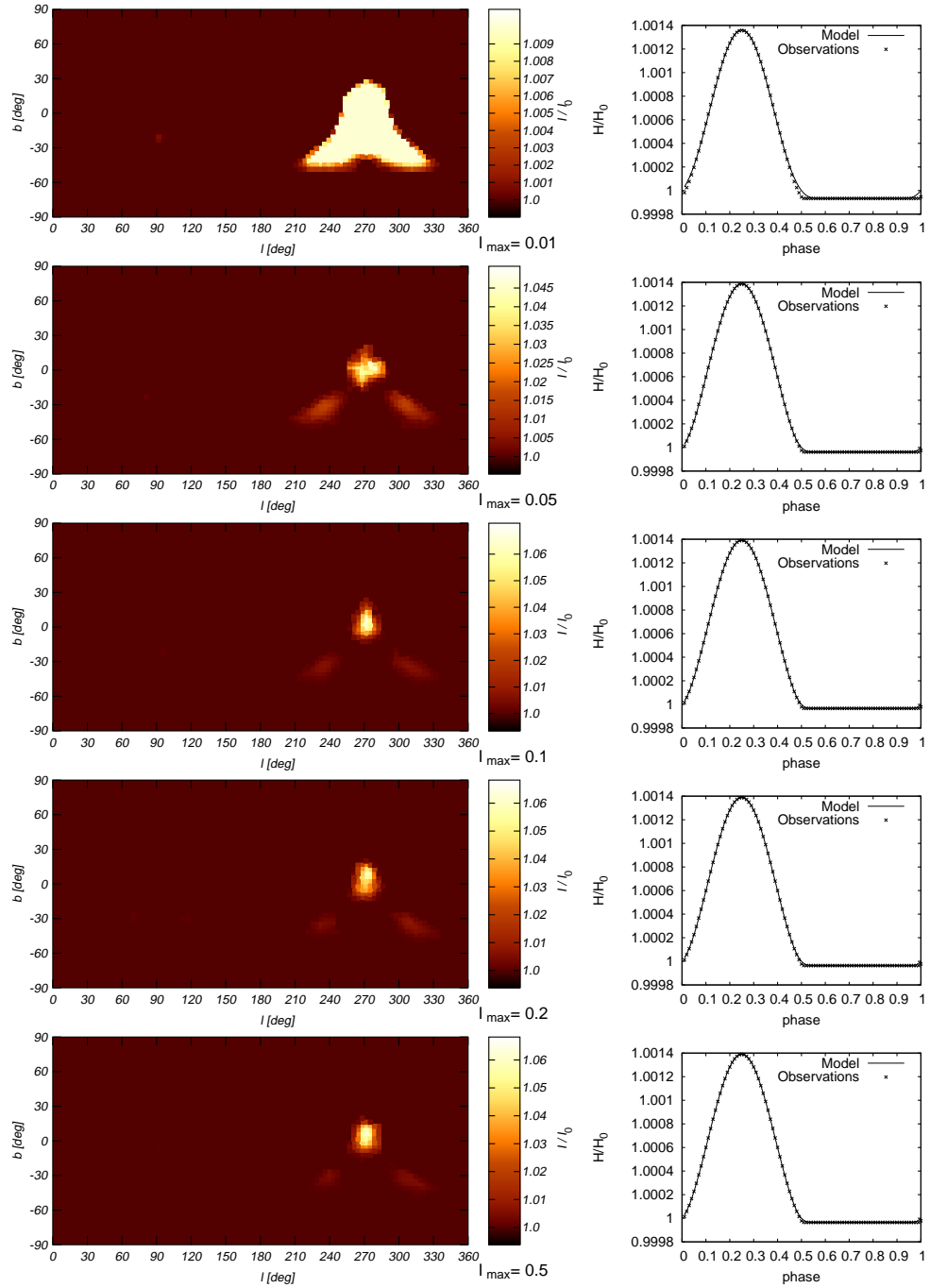


Figure 5.6: A set of intensity maps generated with the regularization parameter $a_R = 0.02$, inclination $i = 50^\circ$ and different values of the maximum spot intensity $\Delta I_{\max}/I_0$ (left panel) and the corresponding light curve fit (right panel). The solid line shows the light curve resulting from the flux distribution of the derived map, and the points denote the input light curve. H_0 is the median of the flux values in the observed light curve.

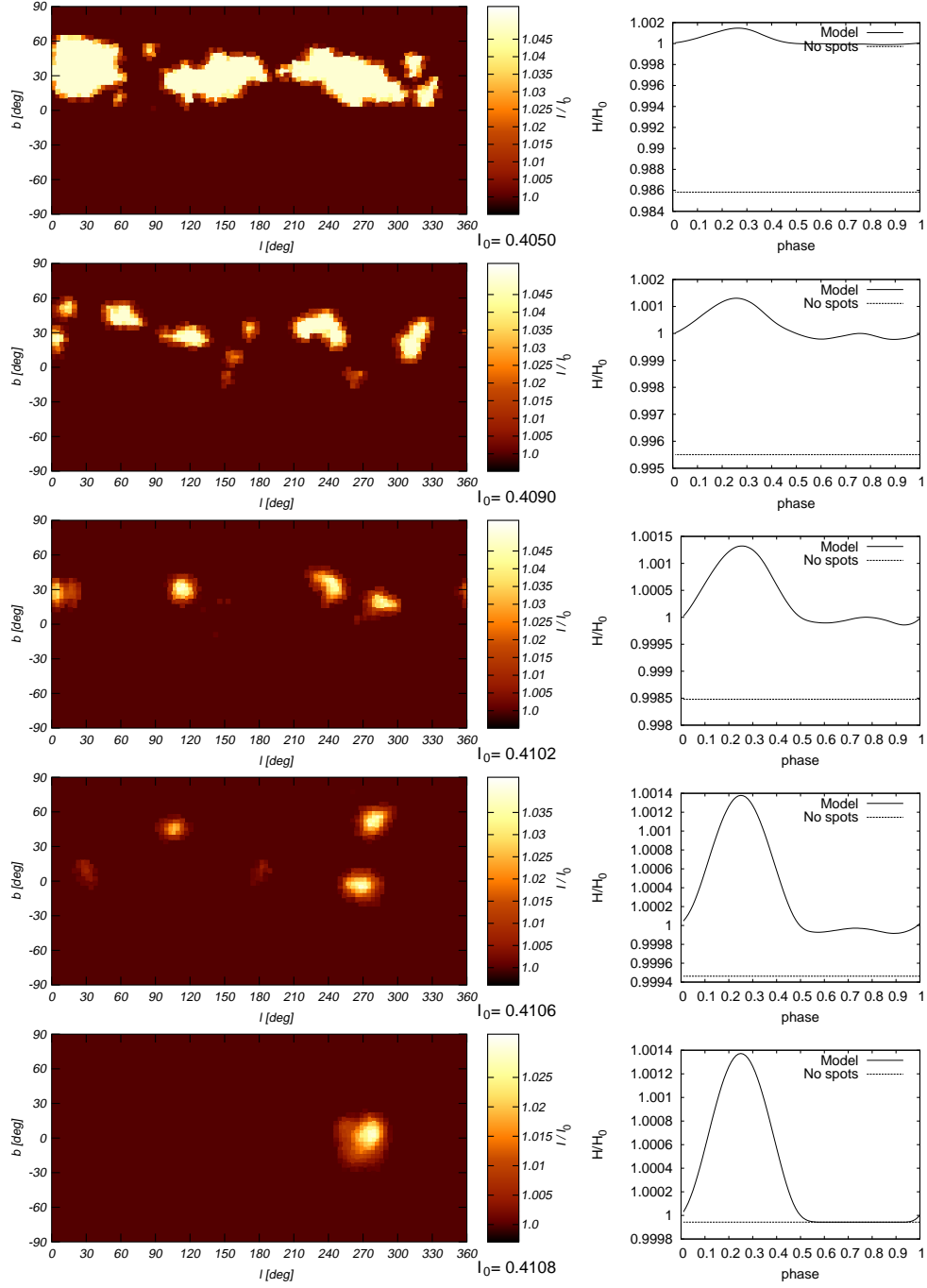


Figure 5.7: A set of intensity maps generated with regularization parameter $a_R = 0.1$, inclination $i = 50^\circ$, the maximum spot intensity $\Delta I_{\max}/I_0 = 0.05$, and different values of the background intensity I_0 emergent from a stellar atmosphere outside of bright spots (left panel) and the corresponding light curve fit (right panel). The solid line shows the light curve resulting from the flux distribution of the derived maps, dashed line shows the light curve of the initial spotless map, and the points denote the input light curve. H_0 is the median of the flux values in the observed light curve.

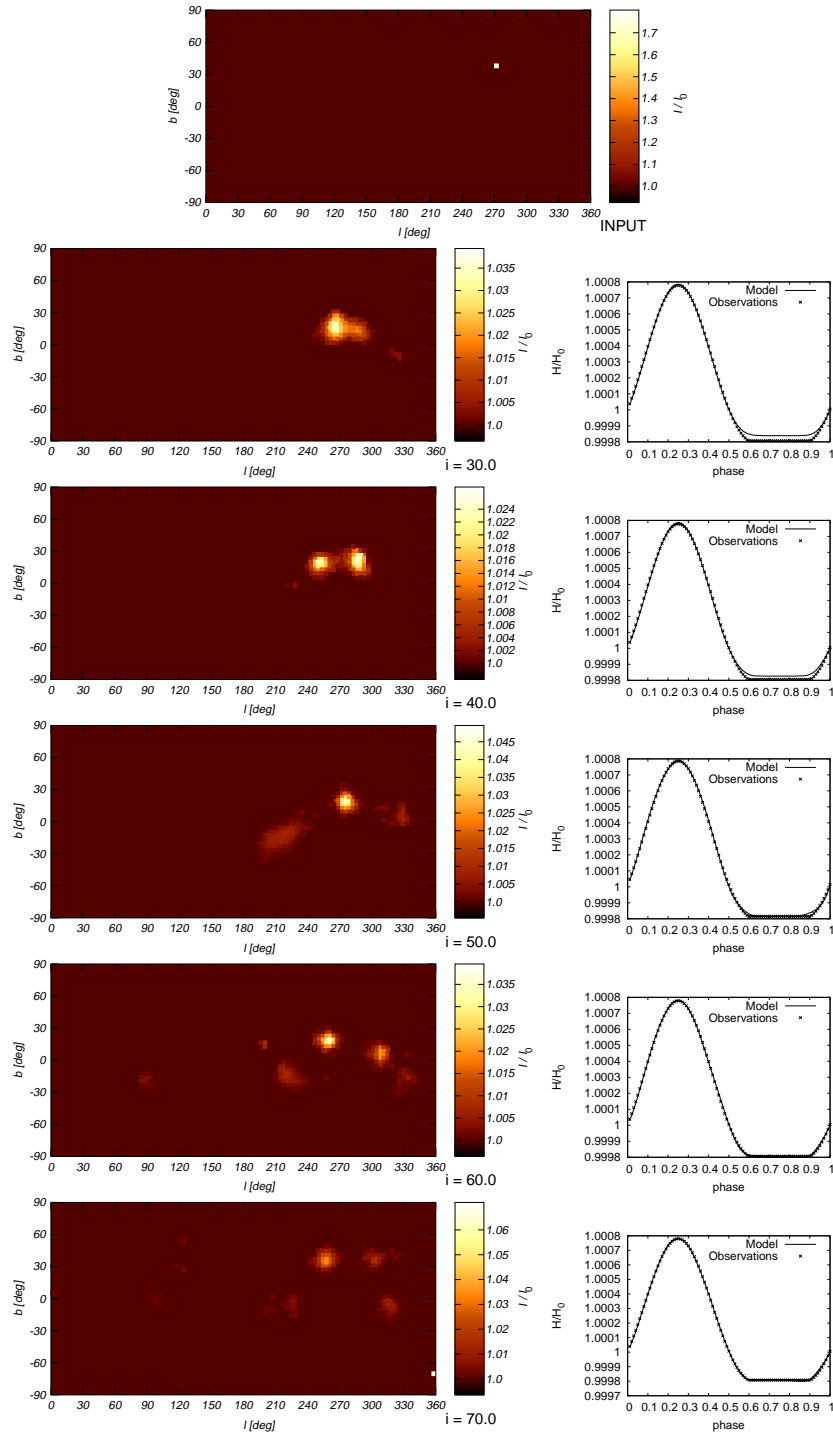


Figure 5.8: A set of intensity maps generated with regularization parameter $a_R = 0.2$, the maximum spot intensity $\Delta I_{\max}/I_0 = 0.2$, and different values of the assumed inclination i (the real inclination of the artificial star is 50°) emergent from a stellar atmosphere outside of bright spots (left panel) and the corresponding light curve fit (right panel). The solid line shows the light curve resulting from the flux distribution of the derived map, whereas the points denote the input light curve. H_0 is the median of the flux values in the observed light curve.

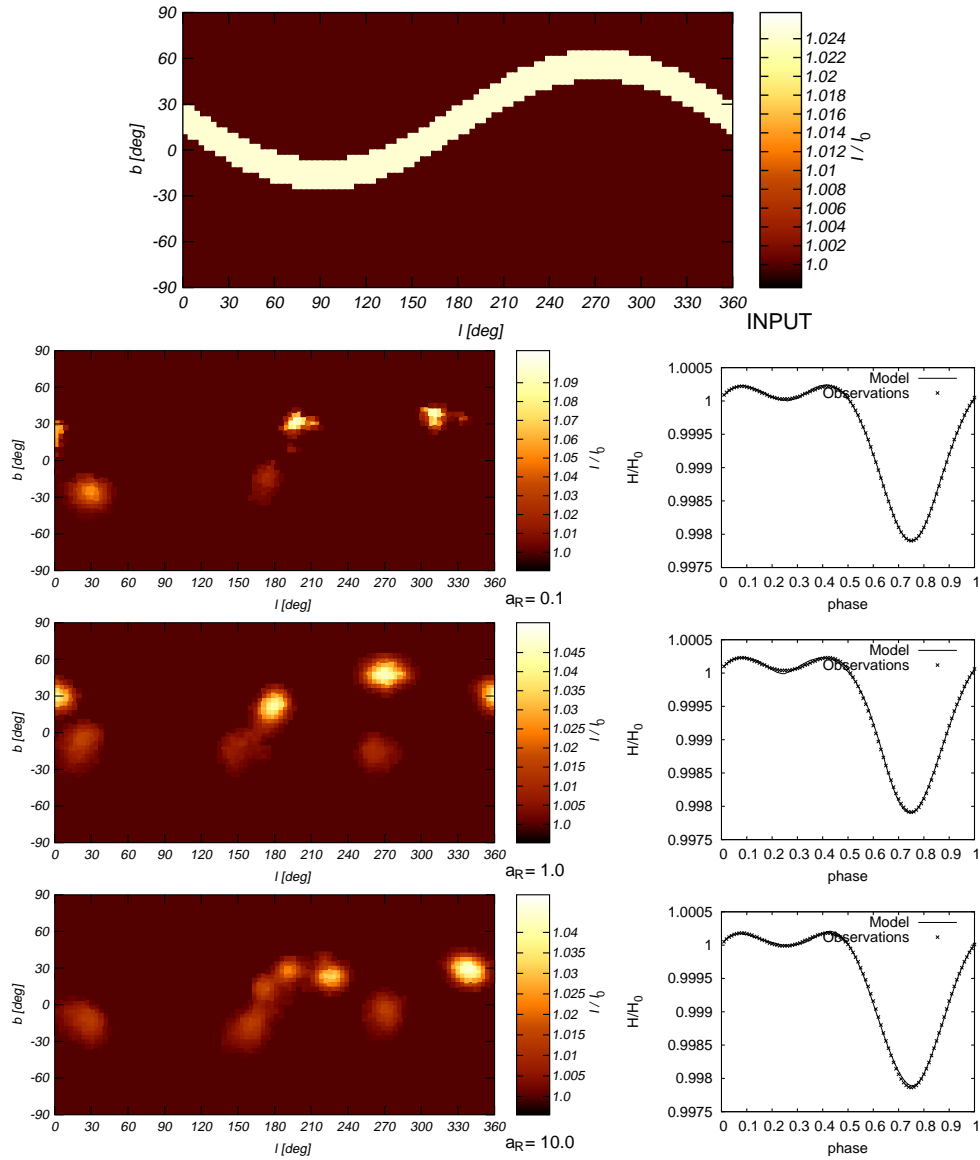


Figure 5.9: *Top panel:* Artificial intensity map with a bright oblique ring used for code testing. *Below:* Maps derived from the light curve computed from the artificial map using the values of the regularization parameter $a_R = 0.1, 1.0$, and 10.0 , respectively.

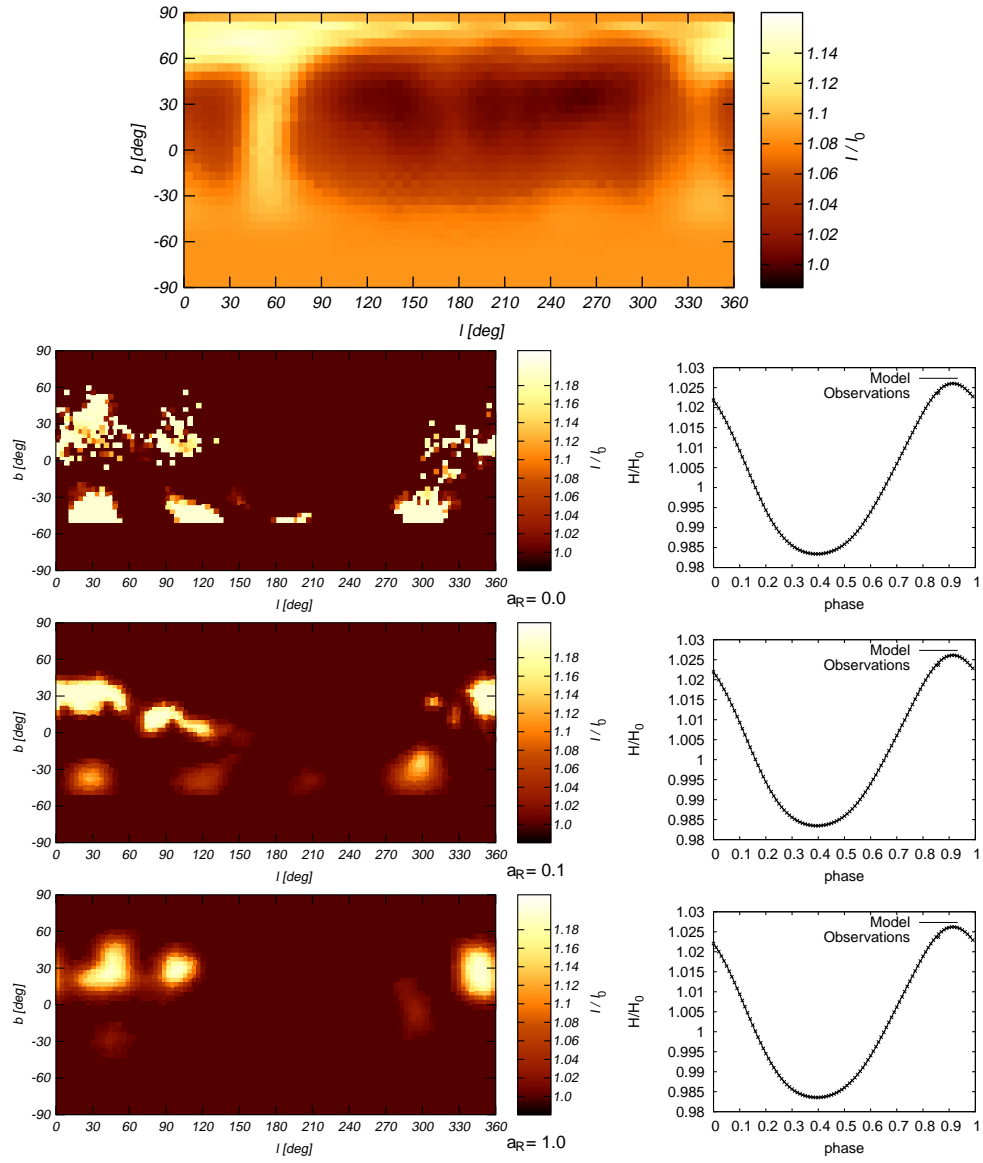


Figure 5.10: *Top*: Intensity map of φ Draconis (see Section 4.1) used for code testing. *Below*: Maps derived from the light curve computed from the map of φ Dra using the values of the regularization parameter $a_R = 0.0, 0.1$, and 1.0 , respectively and assuming inclination $i = 60^\circ$, allowing maximum brightness of the spot $\Delta I/I_0 = 0.2$.

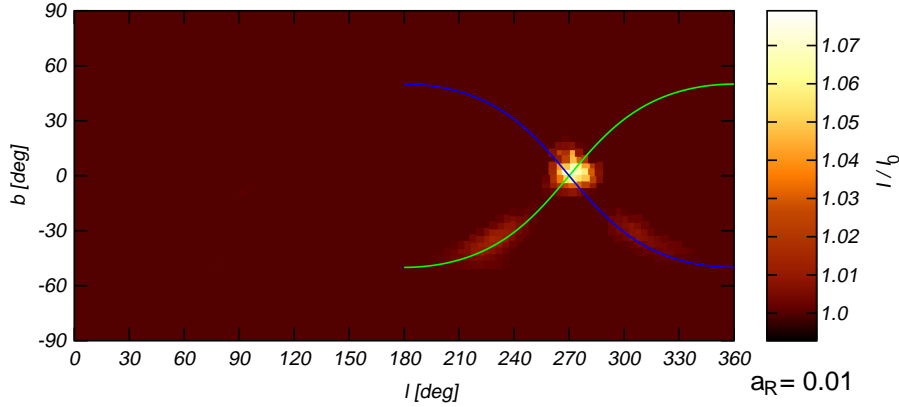


Figure 5.11: Intensity map for one-spot model with $a_R = 0.01$ (the same as in Fig. 5.5). The blue line indicates all points at the surface of the map that appear on the visible disc at the same rotational phase. The green line connects the points that disappear from the visible disc at the same rotational phase.

The values of a_R in the range of (0.1; 1.0) seem to give the best result here, although the appropriate value might depend on each individual case.

Limiting the maximum emergent intensity ΔI_{\max} forces the program to create larger spots, as can be seen in Fig. 5.6. Setting the maximum intensity too low can prevent the code from reaching the desired amplitude of the light variability. However, even if ΔI_{\max} is set to a high value, the range of the intensities used might be still limited by regularization, as the two maps at the bottom of the figure demonstrate.

The value of the background intensity I_0 is also important for the computations, as shown in Fig. 5.7. A set of maps has been computed with different values of I_0 . The parameter I_0 corresponds to the constant brightness of the stellar surface without the bright spots and constitutes a major portion of the emergent flux. The rest of the flux has to be filled in by the spots. If I_0 is set too low, the code has to fill in the missing flux by adding a number of randomly placed large spots as seen on the top panels of the figure.

We can also test how the value of the inclination that we assume for the computation, affects the result. This is shown in Fig. 5.8. We start with a simple map containing a single bright spot, but unlike the previously discussed cases, this time the spot is located at a higher latitude, approximately 40° . The inclination of the artificial star is 50° . When we try to fit the variability of this star with a model with a lower inclination, the code will have to increase the brightness of the spot, either by increasing the emergent intensity or by increasing the size of the spot (see Eq. 5.3).

Another artificial map with an oblique bright ring, inspired by abundance maps derived by Bohlender (1988), is shown in Fig. 5.9 together with the solutions computed by our code for three different values of the regularization parameter. In all cases the program solved the problem by a group of separate spots, rather than forming a contiguous ring. The layout of the spots resembles the form of the ring placed on the input map, even though they do not match the latitude precisely. All solutions produce light curves that are in a very good agreement with the input light curve.

Fig. 5.10 shows the intensity maps computed from the light curve of the star φ Dra in the near-UV U passband of the ten-color photometric system based on our synthesis in Section 4.1 compared with the intensity map derived from Doppler imaging. Here we allowed brightness variation of 20 %, corresponding to the range of emergent intensities of the input map. The resulting map differs significantly from the input map. While the distribution of intensities in longitude is relatively good, the layout of the bright spots in latitude is not satisfactory. The code apparently

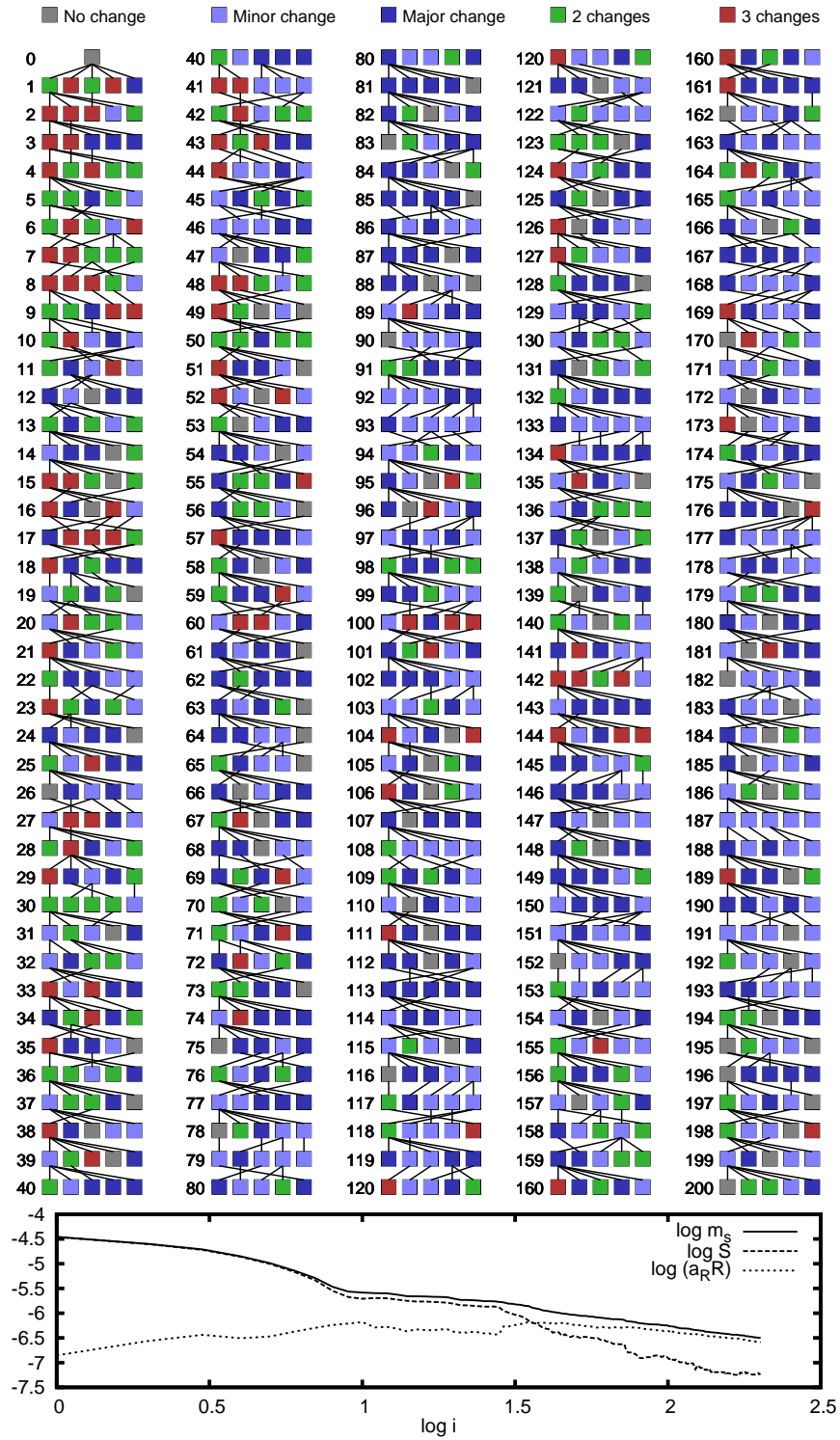


Figure 5.12: The first 200 iterations of an example run of the code deriving the map from Fig. 5.5 for $a_R = 1.0$. *Top panel:* The best five specimen of each generation are shown in each group, sorted left-to-right in the order of decreasing fitness $f = 1/m_s$. The lines connect each map with its parent in the previous generation. The generation number is displayed on the left side of each group. The color of each individual map indicates the number of changes made to derive the map from its parent. *Bottom panel:* The logarithms of the map score, the sum of squares, and the regularization penalty plotted versus logarithm of the iteration number.

avoids placing spots near the pole. This is likely the result of the regularization which penalizes brightness changes at high latitude.

The spots on the maps often have lengthy diagonal or triangular shapes, or feature diagonal south-facing “wings”. A typical example is the spot on the second map ($a_R = 0.01$) of Fig. 5.5. If the code tries to fit a maximum of the light variability, it creates a spot at the corresponding longitude and latitude so that the modelled and observed maximum agree in width and phase. It aims to eventually match the amplitude of the peak by modifying the intensity of the spot. If it can not, however, reach sufficient intensity, either because the maximum intensity constrain does not allow it or because the regularization makes further increase of the intensity too expensive, it has to use adjacent surface elements to increase the amplitude. Using the elements to the north, east or west of the spot would widen the light curve profile, so it is undesirable. Fig. 5.11 shows the spot from Fig. 5.5. The blue curve here connects all the point at the surface of the star that appear on the visible disc at the same rotational phase as the spot in question. Analogically, the green curve shows all the points that disappear from the visible part of the disc at the same rotational phase as the spot. Therefore, the surface elements located below both the green curve and the blue curve are visible when the main spot is visible and can be used to augment the brightness of the star modelled by the main spot without widening the profile of the photometric maximum. It can be seen in the figure that the “wings” of the spot follow the green and blue lines very closely. The same principle can be used to model asymmetric light curves. If we create a spot that follows the blue line, we get a photometric maximum consisting of a fast increase in brightness followed by a slow decline. If we create a lengthy spot following the green line, a slow onset of the maximum will be followed by a fast drop in brightness.

Fig. 5.12 shows an example run of the program. Five best maps of each iteration are represented by squares, with lines connecting the maps with their respective parents and children. The colors of the boxes represent the number of changes that were made to derive the map from its parent. The plot indicates that in many cases even the maps that are not the best in their iteration can produce children that become the best in the following iteration. At the bottom of the figure the convergence of the code is shown. At first, the map contains no spots and the regularization penalty R is equal to zero. The code then starts to add spots to the map to decrease the discrepancy S between the observed and modelled light curves, at the cost of increasing R . Eventually, the regularization term R becomes the dominant component of m_s and the code is forced to smooth out the intensity distribution.

It is obvious that the choice of the initial parameters of the model is important for the result of the computation. The wrong choice of these values might easily lead to incorrect intensity distribution maps. However, even with the appropriate values the map is not guaranteed to show the correct distribution of brightness on the surface of the studied star. There is a large uncertainty in latitudes. Additionally, the code is to some extent dependent on a random factor, so individual runs of the program started with identical parameters might produce different solutions. The good agreement between the observed and the modelled light curves even for intensity maps very different from the real distribution clearly indicates that the solution to the problem is not unique. The surface analysis using this method should therefore not be regarded as a way to obtain reliable intensity maps of stars, but rather just a test of applicability of the oblique rotator model for describing an observed light variability. If the results indicate an acceptable solution exists for a given star, a more sophisticated method such as the Doppler imaging, using the detailed spectroscopy, should be employed to derive the surface distribution of the emergent intensity or chemical abundances.

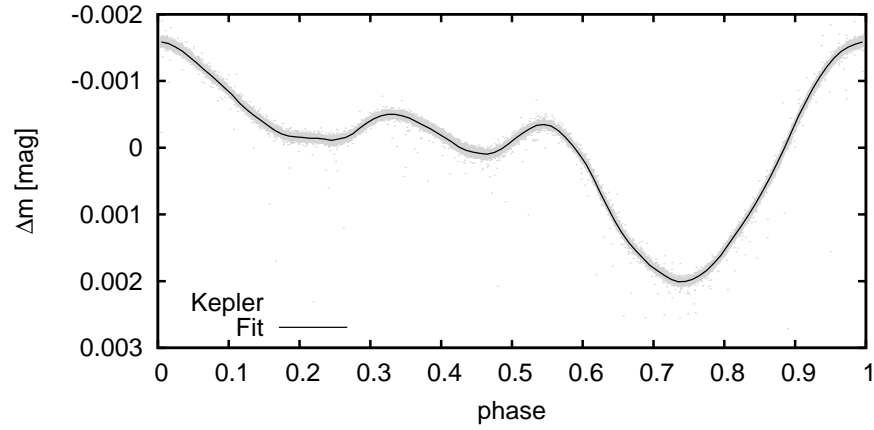


Figure 5.13: Light curve of KIC 11560273 based on Kepler photometry (dots) and the mean curve (solid line).

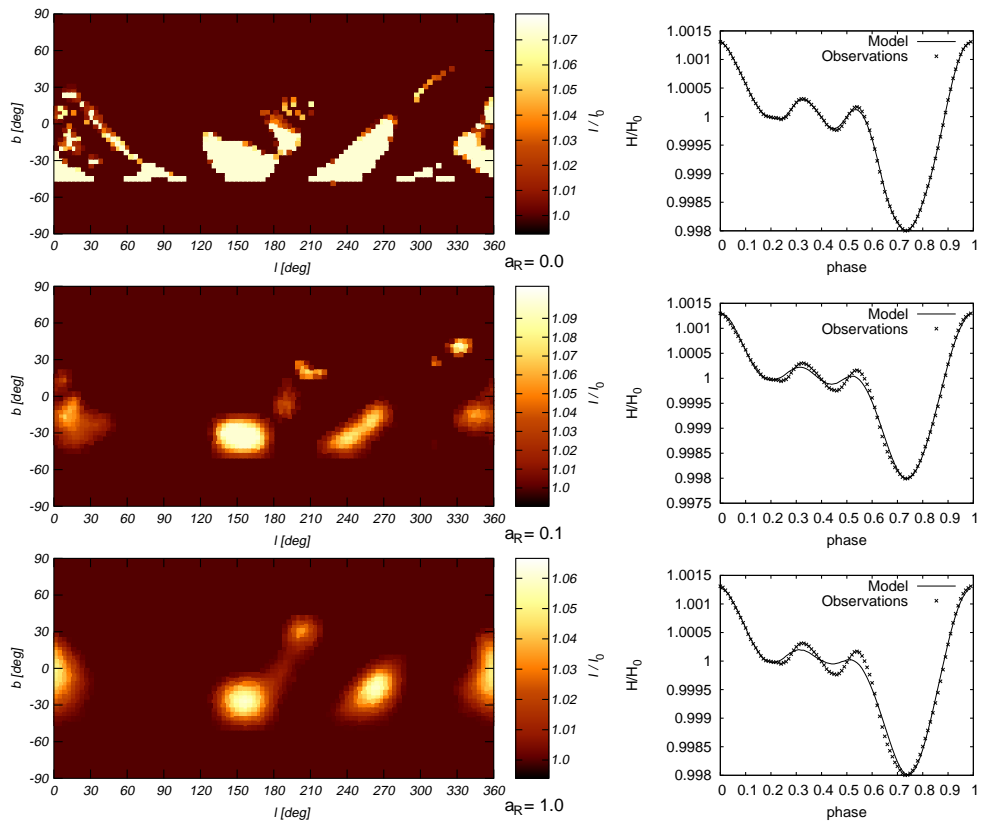


Figure 5.14: Intensity map of KIC 11560273 (left) derived from the light curve using $a_R = 0.0$ (top), $a_R = 0.1$ (middle), and $a_R = 1.0$ (bottom), and the corresponding fit of the light curve (right). Inclination i is assumed to be equal to 50° .

5.3 KIC 11560273

We shall now use the method to analyse the light curve of the star KIC 11560273 (= HD 184007 = HIP 95869). The object is a primary component of a binary star of the spectral class A0V (Murphy 1969) with the ephemeris for the maximum of the light variability $MJD = 55686.343 + 1.82746769(9)E$ (Hümmerich et al. 2018). The light curve of the star observed by Kepler is shown in Fig. 5.13 together with a simplified fit. Each of the points in the fit was obtained by averaging the emergent intensities for all datapoints in the interval of rotational phases ($\varphi_0 - 0.005; \varphi_0 + 0.005$). The light curve has the primary maximum at phase 0 and minimum approximately at phase 0.75. There is a fast variation of brightness between phases 0.2 and 0.6 that is not common in spotty CP stars. For this reason we want to use our code to see if this variability can be explained by a bright spot model.

Fig. 5.14 shows our attempt to solve the surface distribution of the emergent intensity. We do not know the inclination of the star, so we assume $i = 50^\circ$. The code has serious difficulties fitting the fast brightness variation between the phases 0.2 and 0.6. Not surprisingly, the fit of the light curve gets better with increasing the intensity limit, but even with the regularization turned off and allowing for brightness variation as high as 10 %, the agreement with the observation is not ideal. In addition, to achieve this fit, the code had to create spots of very complex and irregular nature. In order to obtain a satisfactory fit of the light curve using reasonable number of spots, we would have to increase the maximum allowed intensity even further. This indicates that the variability of KIC 11560273 can not be fully explained by the oblique rotator model and photometric abundance spots at the surface of the star. It is likely that other mechanisms contribute to the variability of the star.

5.4 GALEX J014636+323615

Another candidate for intensity mapping is the white dwarf GALEX J014636+323615. Part of this work has been published in Reindl et al. (2019). The star belongs to a class of very hot ($T_{\text{eff}} > 60000 \text{ K}$) white dwarfs exhibiting ultra-high excitation absorption lines, showing periodic equivalent width variations. These lines are assumed to originate in the hot circumstellar matter, forming an optically thick torus confined within the stellar magnetosphere and corotating with the star (Werner et al. 1995). The exact mechanism responsible for this phenomenon is still unknown. The star is also photometrically variable with ephemeris of the maxima $HJD = 2456595.98922 + 0.242035(1)E$. These variations could be explained by uneven distribution of the emergent intensity on the surface of the star. The lightcurve of the star is shown in Fig. 5.15.

Compared to the previous example, the light curve is less complex in shape. However, the amplitude of the variability is much greater. In order to explain it, we have to allow significantly larger range of surface intensities. The result of the computation is in Fig. 5.16. The maps for $a_R = 0.0, 0.1$, and 1.0 were derived. The light variability was matched with a set of three large bright spots. The synthesized light curves nicely agree with the observations. This suggests that the oblique rotator model can explain the photometric variability of the star.

5.5 HD 144941

The last example for our light curve analysis is the subdwarf HD 144941. MacConnell et al. (1970) noticed very high abundance of helium and quite low abundance of hydrogen in the atmosphere of this star. With an effective temperature $T_{\text{eff}} = 21\,500 \text{ K}$, and surface gravity $\log g = 3.5$, the star is considerably underluminous (Hunger & Kaufmann 1973). Despite the fact that it lies within the

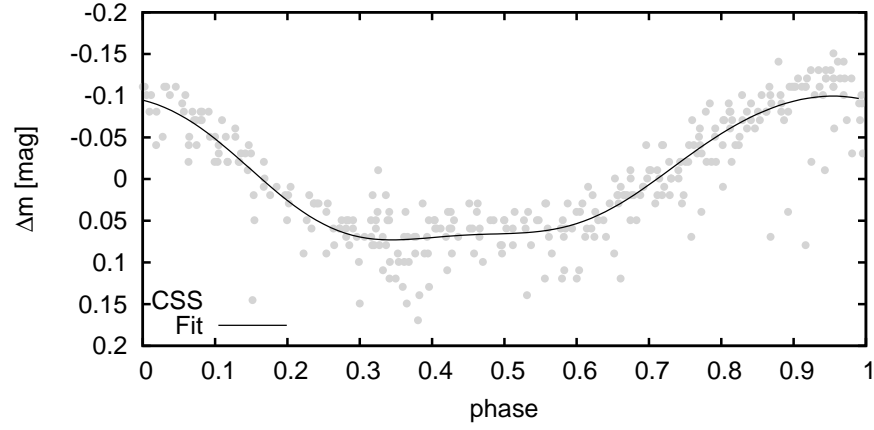


Figure 5.15: Light curve of GALEX J014636+323615 based on Catalina Sky Survey photometry (dots) and the mean curve (solid line).

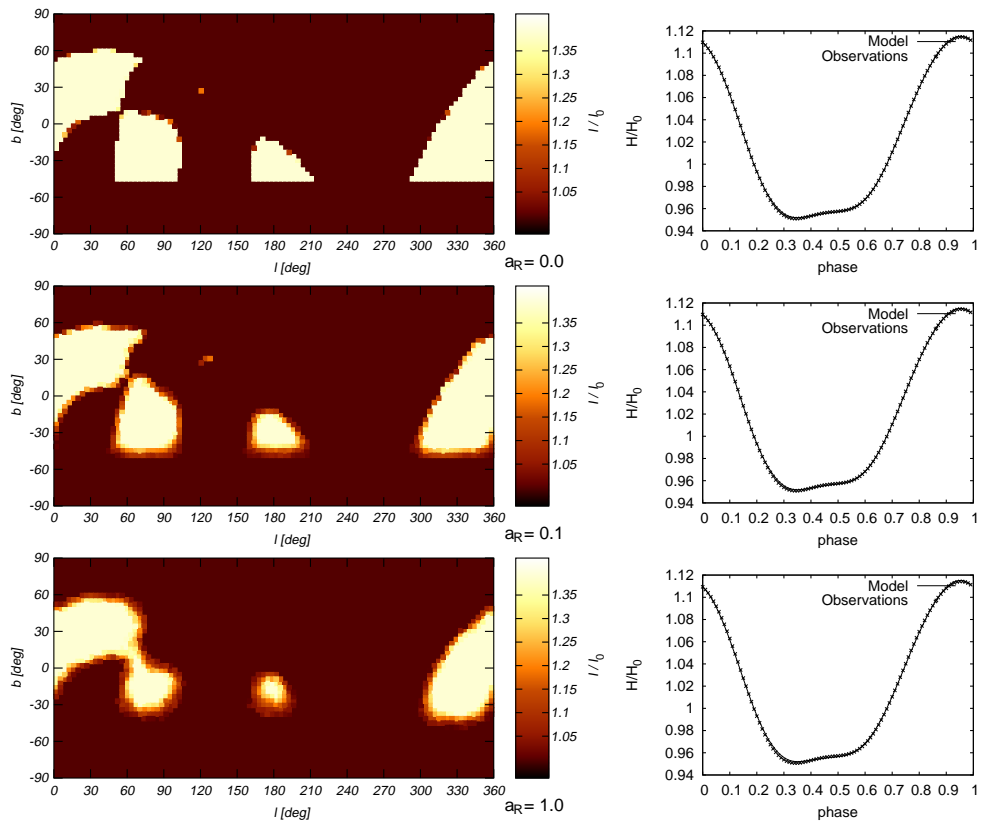


Figure 5.16: Intensity map of GALEX J014636+323615 (left) derived from the light curve using $a_R = 0.0$ (top), $a_R = 0.1$ (middle), and $a_R = 1.0$ (bottom), and the corresponding fit of the light curve (right).

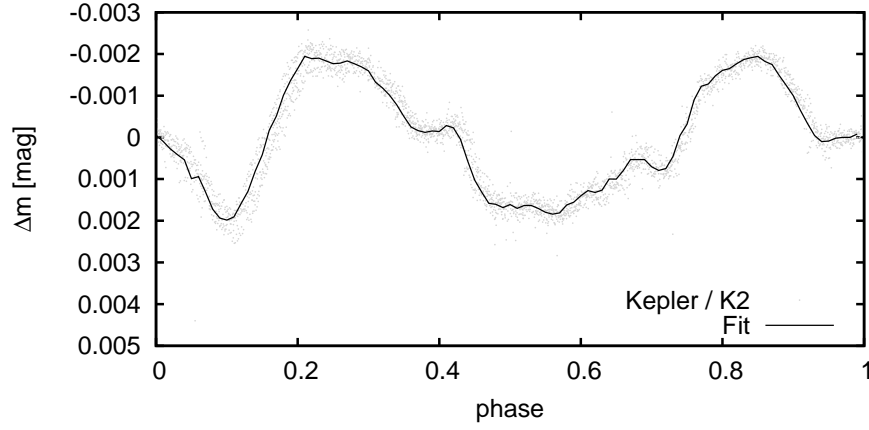


Figure 5.17: Light curve of HD 144941 based on Kepler / K2 photometry (dots) and the mean curve (solid line).

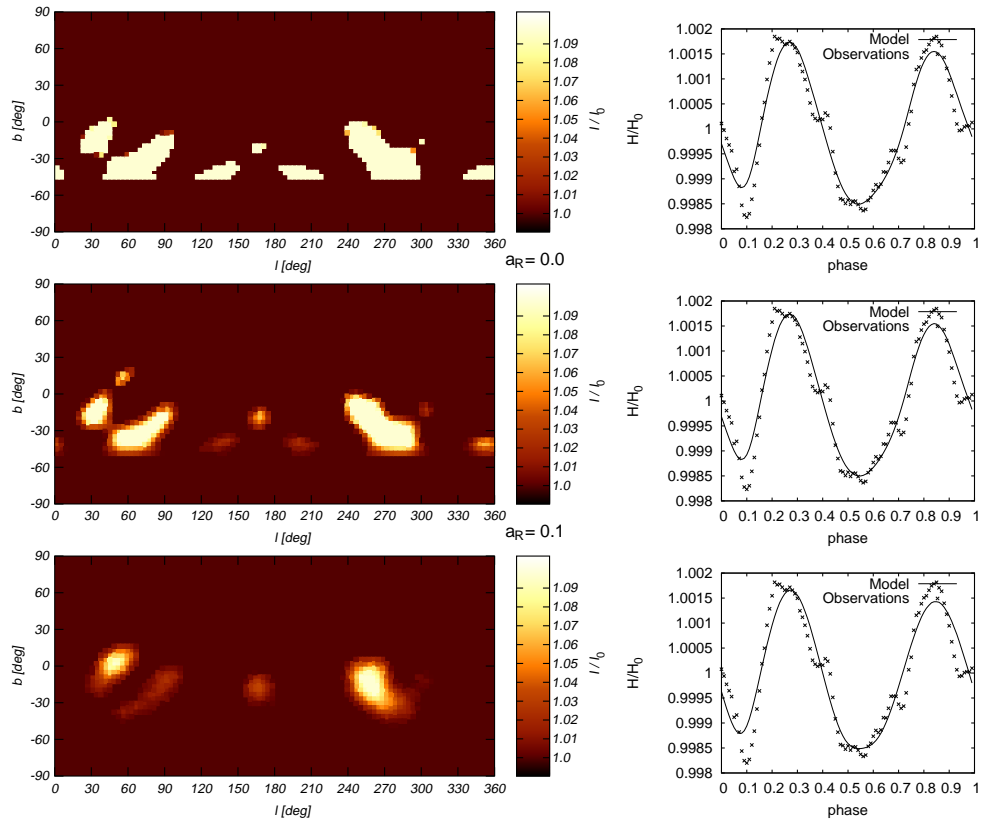


Figure 5.18: Intensity map of HD 144941 (left) derived from the light curve using $a_R = 0.0$ (top), $a_R = 0.1$ (middle), and $a_R = 1.0$ (bottom), and the corresponding fit of the light curve (right).

instability strip, no variability related to possible pulsations has been found (Jeffery & Hill 1996). Kepler / K2 photometry has been obtained from Jeffery & Ramsay (2018). The light curve, shown in Fig. 5.17, has a double-wave form, plus three extra “bumps” at phases 0.4, 0.7, and 0.95. The magnitude of the light variability is approximately 2 millimagnitudes. The zero phase is determined using the ephemeris $MJD = 4084.31 + 13.93 E$.

Fig. 5.18 displays the output of the synthesis. The code was again run with three different values of the regularization parameter. The model fits the basic features of the observed variability, although none of the variants managed to cope with the three bumps, indicating these short-term variations of emergent flux result from a source other than the photometric spots on the surface of an oblique rotator.

5.6 Conclusions

In this chapter we have discussed the possibility of deriving the surface brightness distribution from light curves. It is obvious from the geometric description of the problem that the solution is not unique. Therefore we imposed several criteria on the result. We were looking for intensity maps containing only bright spots of limited intensity compared with the emergent intensity of the rest of the surface. We introduced regularization to prefer solutions that are continuous, smooth and not overly complex.

We created our own code to derive the emergent intensity maps. The tests of the program performed by analyzing the lightcurves of artificial stars, whose surface brightness distributions were known, indicate that the solution can vary significantly depending on the input parameters. The size of spots depends on the maximum allowed spot intensity as well as the regularization used. Inadequate values of the input parameters often introduce undesirable spot structures in the resulting maps. Such maps often provide mathematically good solutions to the problem and result in good agreement with the observed variability of the star. Therefore, great care must be taken to correctly interpret the results obtained using this technique.

We have also used the program to derive intensity maps of three very different variable stars. The program managed to model the basic features of the light curves, but in the case of the Ap star KIC 11560273 and the helium subdwarf HD 144941 the model could not explain fast light variations in some parts of the light curve. It is therefore possible that the variability of these stars is not caused by bright abundance spots on the stellar surface, or that these spots are not the only source of the variability. The photometric variations of the white dwarf GALEX J014636+323615 were, on the other hand, sufficiently explained by the oblique rotator model, even though we have to allow quite high variation in brightness to match the high amplitude.

Our method is purely geometrical, which means the results tell us very little about the chemical composition or the physical structure of the stellar atmosphere, but it also means that they are not affected by inaccuracy of atomic data or the model atmospheres. Other methods have also been used to derive the surface intensity distribution of stars, such as the Bayesian method (see e.g., Lüftinger et al. 2010a). These methods usually assume a small number of circular spots to explain the photometric variability of the star. Our code, on the other hand, does not have this limitation.

Overall, the code seems to be a very useful tool for testing the usability of the oblique rotator model to explain photometric variability of stars, and to help pick (or exclude) candidates for Doppler imaging. While the reliability of the resulting maps is questionable, and is unlikely, due to the intrinsic mathematical limitations of the problem, to improve in the future, we believe that further development and works in this area are welcome and will contribute to our understanding of the photometric variability of stars.

Summary and conclusions

We have discussed the topic of chemically peculiar stars, their surface abundance anomalies, and various forms of their variability. We have shown that line profile variations can be used to derive the distribution of surface abundance structures. Using the Doppler imaging method, we derived abundance maps of several chemical elements of the star V824 Cen. While this is still a work in progress, and the obtained abundance maps should by no means be regarded as final results, the example is sufficient to illustrate the specifics and capabilities of the technique. Our results indicate a highly inhomogeneous surface distribution of iron, magnesium, and silicon. We have also discussed the individual input parameters of the model and the effect their choice has on the resulting abundance maps.

We have also shown that the knowledge of the surface abundance structures allows us to predict the photometric variability of CP stars. From abundance maps obtained from other authors, we managed to reconstruct the light variations of two CP stars. In the case of the first one, the Ap star φ Dra, our results indicate photometric variability mainly due to absorption in lines of iron as well as absorption in the continuum by silicon. The predicted light curve is in a good agreement with the observed light variations of the star.

In the case of the non-magnetic HgMn star φ Phe, the predicted variations are caused by bound-bound transitions of titanium and yttrium. The amplitude is much smaller compared to φ Dra. Comparing the synthetic light curves computed from abundance maps based on spectroscopy obtained at four distinct times, we have shown that secular changes of the surface abundance structures result in gradual changes of the shape of the light curve of the star. The computed light curves qualitatively agree with the photometric variability of the star observed by the TESS satellite, but an exact comparison is not possible due to the large time gap between the map sets and the TESS observations.

We have developed a simple code to estimate light intensity distribution from photometry. The code is based on naive trial and error method and is, of course, inferior to the Doppler imaging in terms of reliability of the obtained maps. It may, however, still prove to be a useful tool for stars that are too faint for high-dispersion spectroscopy, or to narrow down a list of potential CP star candidates, eliminating stars whose variability is inconsistent with the oblique rotator model. We tested the code on several artificial stars, and we also used it to explain the observed photometric variability of a few variable stars. We were able to describe the light variations of the white dwarf GALEX J014636+323615, in the case of the probable subdwarf HD 144941 and the main-sequence star KIC 11560273 the model of photospheric spots is not sufficient to explain all the details of the observed light variations.

There is still much work to do in the field. There is room for improvement in the area of the atomic data, and the accuracy of the model atmospheres. With the constant growth of the available computing power, the codes used in astrophysical simulations are expected to improve. We can already explain the basic features of the variability of most of the CP stars, but many questions remain unanswered. The explanation of the origin of the surface abundance peculiarities given

by the theory of radiative diffusion (Michaud 1970) is still at best qualitative. The reason for the lack of correlation between the geometry of the magnetic fields and the surface distribution of chemical abundances observed in some cases remains to be found. Some minor features seen in the light curves (such as the case of KIC 11560273) cannot be explained by photospheric spots. However, these changes occur consistently with the period equal to the rotational period of the star, so there is no doubt that they are related to the rotation. It may well be worth investigating whether the variability of these stars can be explained by a combination of the oblique rotator with photospheric spots and the rigidly rotating magnetosphere.

References

- Abt, H. A. & Morrell, N. I. 1995, *ApJS*, 99, 135
- Alecian, E., Catala, C., Wade, G. A., et al. 2009, in *EAS Publications Series*, Vol. 39, *EAS Publications Series*, ed. C. Neiner & J.-P. Zahn, 121–132
- Alecian, E., Neiner, C., Mathis, S., et al. 2013, *A&A*, 549, L8
- Alecian, G. & Stift, M. J. 2019, *MNRAS*, 482, 4519
- Alecian, G., Stift, M. J., & Dorfi, E. A. 2011, *MNRAS*, 418, 986
- Aurière, M., Wade, G. A., Silvester, J., et al. 2007, *A&A*, 475, 1053
- Babcock, H. W. 1947, *ApJ*, 105, 105
- Babcock, H. W. 1958, *ApJS*, 3, 141
- Bailey, J. D., Grunhut, J., & Landstreet, J. D. 2015, *A&A*, 575, A115
- Bailey, J. D., Landstreet, J. D., & Bagnulo, S. 2014, *A&A*, 561, A147
- Bautista, M. A. 1996, *A&AS*, 119, 105
- Bautista, M. A. & Pradhan, A. K. 1997, *A&AS*, 126, 365
- Belopolsky, A. 1913, *Astronomische Nachrichten*, 196, 1
- Blazère, A., Neiner, C., & Petit, P. 2016a, *MNRAS*, 459, L81
- Blazère, A., Petit, P., Lignières, F., et al. 2016b, *A&A*, 586, A97
- Bohlender, D. A. 1988, PhD thesis, The University of Western Ontario (Canada).
- Bonsack, W. K. 1974, *PASP*, 86, 408
- Braithwaite, J. 2014, in *IAU Symposium*, Vol. 302, *Magnetic Fields throughout Stellar Evolution*, ed. P. Petit, M. Jardine, & H. C. Spruit, 255–264
- Braithwaite, J. & Spruit, H. C. 2004, *Nature*, 431, 819
- Briquet, M., Korhonen, H., González, J. F., Hubrig, S., & Hackman, T. 2010, *A&A*, 511, A71
- Budaj, J. 1996, *A&A*, 313, 523
- Burbidge, E. M. & Burbidge, G. R. 1955, *ApJ*, 122, 396

- Butler, K., Mendoza, C., & Zeippen, C. J. 1993, *Journal of Physics B Atomic Molecular Physics*, 26, 4409
- Bychkov, V. D., Bychkova, L. V., & Madej, J. 2013, *AJ*, 146, 74
- Castelli, F. 2005, *Memorie della Societa Astronomica Italiana Supplementi*, 8, 25
- Castelli, F. & Hubrig, S. 2004, *A&A*, 425, 263
- Catalano, F. A. & Leone, F. 1993, *A&AS*, 97, 501
- Catanzaro, G., Giarrusso, M., Leone, F., et al. 2016, *MNRAS*, 460, 1999
- Ciatti, F., Bernacca, P. L., & D’Innocenzo, A. 1978, *A&A*, 69, 171
- Cox, A. N. 2000, *Allen’s astrophysical quantities*
- Deutsch, A. J. 1958, in *IAU Symposium, Vol. 6, Electromagnetic Phenomena in Cosmical Physics*, ed. B. Lehnert, 209
- Deutsch, A. J. 1970, *ApJ*, 159, 985
- Drake, S. A., Abbott, D. C., Bastian, T. S., et al. 1987, *ApJ*, 322, 902
- ESA, ed. 1997, *ESA Special Publication, Vol. 1200, The HIPPARCOS and TYCHO catalogues. Astrometric and photometric star catalogues derived from the ESA HIPPARCOS Space Astrometry Mission*
- Falk, A. E. & Wehlau, W. H. 1974, *ApJ*, 192, 409
- Ferrario, L., Pringle, J. E., Tout, C. A., & Wickramasinghe, D. T. 2009, *MNRAS*, 400, L71
- Fossati, L., Castro, N., Morel, T., et al. 2015, *A&A*, 574, A20
- Fossati, L., Schneider, F. R. N., Castro, N., et al. 2016, *A&A*, 592, A84
- Fowler, W. A., Burbidge, E. M., Burbidge, G. R., & Hoyle, F. 1965, *ApJ*, 142, 423
- Fowler, W. A., Burbidge, G. R., & Burbidge, E. M. 1955, *ApJS*, 2, 167
- George, S. J. & Stevens, I. R. 2012, *Bulletin of the Astronomical Society of India*, 40, 105
- Goldberg, D. E. 1989, *Genetic Algorithms in Search, Optimization and Machine Learning*
- Goncharskii, A. V., Stepanov, V. V., Khokhlova, V. L., & Yagola, A. G. 1982, *Soviet Ast.*, 26, 690
- Goncharskii, A. V., Stepanov, V. V., Kokhlova, V. L., & Yagola, A. G. 1977, *Soviet Astronomy Letters*, 3, 147
- Gräfener, G., Koesterke, L., & Hamann, W.-R. 2002, *A&A*, 387, 244
- Gray, R. O. 1988, *AJ*, 95, 220
- Greenstein, J. L. & Wallerstein, G. 1958, *ApJ*, 127, 237
- Grevesse, N. & Sauval, A. J. 1998, *Space Sci. Rev.*, 85, 161

- Guthnick, P. & Prager, R. 1914, Photoelektrische untersuchungen an spektroskopischen Doppelsternen und an Planeten
- Guthrie, B. N. G. 1967, Publications of the Royal Observatory of Edinburgh, 6, 145
- Hardorp, J. & Scholz, M. 1971, A&A, 13, 353
- Hubeny, I. & Mihalas, D. 2014, Theory of Stellar Atmospheres
- Hubrig, S., González, J. F., Ilyin, I., et al. 2012, A&A, 547, A90
- Hubrig, S., Savanov, I., Ilyin, I., et al. 2010, MNRAS, 408, L61
- Hümmerich, S., Mikulášek, Z., Paunzen, E., et al. 2018, A&A, 619, A98
- Hunger, K. & Kaufmann, J. P. 1973, A&A, 25, 261
- Jagelka, M., Mikulášek, Z., Hümmerich, S., & Paunzen, E. 2019, A&A, 622, A199
- Jamar, C. 1977, A&A, 56, 413
- Jaschek, M. & Jaschek, C. 1958, ZAp, 45, 35
- Jaschek, M. & Jaschek, C. 1959, PASP, 71, 48
- Jaschek, M., Jaschek, C., & Arnal, M. 1969, PASP, 81, 650
- Jefferies, J. T. 1968, Spectral line formation
- Jeffery, C. S. & Hill, P. W. 1996, The Observatory, 116, 156
- Jeffery, C. S. & Ramsay, G. 2018, MNRAS, 475, L122
- Kamp, I. & Paunzen, E. 2002, MNRAS, 335, L45
- Kemp, J. C., Swedlund, J. B., Landstreet, J. D., & Angel, J. R. P. 1970, ApJ, 161, L77
- Khalack, V. R. & LeBlanc, F. 2015, Advances in Astronomy and Space Physics, 5, 3
- Khan, S. A. & Shulyak, D. V. 2006, A&A, 454, 933
- Khan, S. A. & Shulyak, D. V. 2007, A&A, 469, 307
- Khokhlova, V. L., Vasilchenko, D. V., Stepanov, V. V., & Romanyuk, I. I. 2000, Astronomy Letters, 26, 177
- Kochukhov, O. 2017, A&A, 597, A58
- Kochukhov, O., Adelman, S. J., Gulliver, A. F., & Piskunov, N. 2007, Nature Physics, 3, 526
- Kochukhov, O. & Bagnulo, S. 2006, A&A, 450, 763
- Kochukhov, O., Drake, N. A., Piskunov, N., & de la Reza, R. 2004, A&A, 424, 935
- Kochukhov, O., Khan, S., & Shulyak, D. 2005, A&A, 433, 671
- Kochukhov, O., Lundin, A., Romanyuk, I., & Kudryavtsev, D. 2011, ApJ, 726, 24

- Kochukhov, O., Makaganiuk, V., Piskunov, N., et al. 2013, *A&A*, 554, A61
- Kochukhov, O., Wade, G. A., & Shulyak, D. 2012, *MNRAS*, 421, 3004
- Kochukhov, O. P. 2007, in *Physics of Magnetic Stars*, ed. I. I. Romanyuk, D. O. Kudryavtsev, O. M. Neizvestnaya, & V. M. Shapoval, 109–118
- Kodaira, K. 1969, *ApJ*, 157, L59
- Korhonen, H., González, J. F., Briquet, M., et al. 2013, *A&A*, 553, A27
- Krivoseina, A. A., Ryabchikova, T. A., & Khokhlova, V. L. 1980, *Nauchnye Informatsii*, 43, 70
- Krtićka, J., Mikulášek, Z., Henry, G. W., et al. 2009, *A&A*, 499, 567
- Krtićka, J., Mikulášek, Z., Lüftinger, T., et al. 2012, *A&A*, 537, A14
- Krtićka, J., Mikulášek, Z., Zverko, J., & Žižňovský, J. 2007, *A&A*, 470, 1089
- Kubát, J. 2003, in *Astronomical Society of the Pacific Conference Series*, Vol. 288, *Stellar Atmosphere Modeling*, ed. I. Hubeny, D. Mihalas, & K. Werner, 87
- Kupka, F., Paunzen, E., Iliev, I. K., & Maitzen, H. M. 2004, *MNRAS*, 352, 863
- Kupka, F., Piskunov, N., Ryabchikova, T. A., Stempels, H. C., & Weiss, W. W. 1999, *A&AS*, 138, 119
- Kupka, F. G., Ryabchikova, T. A., Piskunov, N. E., Stempels, H. C., & Weiss, W. W. 2000, *Baltic Astronomy*, 9, 590
- Kurtz, D. W. 1982, *MNRAS*, 200, 807
- Kurtz, D. W. & Martinez, P. 2000, *Baltic Astronomy*, 9, 253
- Kurucz, R. 1994, *Atomic Data for Fe and Ni*. Kurucz CD-ROM No. 22. Cambridge, Mass.: Smithsonian Astrophysical Observatory, 1994., 22
- Kurucz, R. L. 1996, in *Astronomical Society of the Pacific Conference Series*, Vol. 108, *M.A.S.S., Model Atmospheres and Spectrum Synthesis*, ed. S. J. Adelman, F. Kupka, & W. W. Weiss, 160
- Kuschnig, R. 1998, PhD thesis, Univ. of Vienna
- Kuschnig, R., Ryabchikova, T. A., Piskunov, N. E., Weiss, W. W., & Gelbmann, M. J. 1999, *A&A*, 348, 924
- Landstreet, J. D. 1982, *ApJ*, 258, 639
- Landstreet, J. D. & Borra, E. F. 1977, *ApJ*, 212, L43
- Landstreet, J. D. & Borra, E. F. 1978, *ApJ*, 224, L5
- Landstreet, J. D., Dolez, N., & Vauclair, S. 1998, *A&A*, 333, 977
- Lanz, T., Artru, M.-C., Le Dourneuf, M., & Hubeny, I. 1996, *A&A*, 309, 218
- Lanz, T. & Hubeny, I. 2007, *ApJS*, 169, 83

- Lehmann, G., Lorenz, J., Buzzi, L., et al. 2007, *Minor Planet Electronic Circulars*
- Leto, P., Trigilio, C., Oskinova, L., et al. 2017a, *MNRAS*, 467, 2820
- Leto, P., Trigilio, C., Oskinova, L., et al. 2017b, *MNRAS*, 467, 2820
- Leto, P., Trigilio, C., Oskinova, L. M., et al. 2018, *MNRAS*, 476, 562
- Liebert, J., Ferrario, L., Wickramasinghe, D. T., & Smith, P. S. 2015, *ApJ*, 804, 93
- Liebert, J., Wickramasinghe, D. T., Schmidt, G. D., et al. 2005, *AJ*, 129, 2376
- Lignières, F., Petit, P., Böhm, T., & Aurière, M. 2009, *A&A*, 500, L41
- Liška, J. 2016, *MNRAS*, 461, 939
- Lüftinger, T., Fröhlich, H.-E., Weiss, W. W., et al. 2010a, *A&A*, 509, A43
- Lüftinger, T., Kochukhov, O., Ryabchikova, T., et al. 2010b, *A&A*, 509, A71
- Lüftinger, T., Kochukhov, O., Ryabchikova, T., Weiss, W. W., & Ilyin, I. 2007, *Communications in Asteroseismology*, 150, 85
- Lüftinger, T., Kuschnig, R., Piskunov, N. E., & Weiss, W. W. 2003, *A&A*, 406, 1033
- MacConnell, D. J., Frye, R. L., & Bidelman, W. P. 1970, *PASP*, 82, 730
- Maitzen, H. M. 1976, *A&A*, 51, 223
- Maitzen, H. M. 1984, *A&A*, 138, 493
- Makaganiuk, V., Kochukhov, O., Piskunov, N., et al. 2011, *A&A*, 529, A160
- Manfroid, J. & Renson, P. 1983, *A&AS*, 51, 267
- Mathys, G., Romanyuk, I. I., Hubrig, S., et al. 2019, *A&A*, 624, A32
- Mathys, G., Romanyuk, I. I., Kudryavtsev, D. O., et al. 2016, *A&A*, 586, A85
- Maury, A. C. & Pickering, E. C. 1897, *Annals of Harvard College Observatory*, 28, 1
- Mendoza, C., Eissner, W., LeDourneuf, M., & Zeppen, C. J. 1995, *Journal of Physics B Atomic Molecular Physics*, 28, 3485
- Mestel, L. 1966, *MNRAS*, 133, 265
- Mestel, L. 2003, in *Astronomical Society of the Pacific Conference Series*, Vol. 305, *Magnetic Fields in O, B and A Stars: Origin and Connection to Pulsation, Rotation and Mass Loss*, ed. L. A. Balona, H. F. Henrichs, & R. Medupe, 3
- Michaud, G. 1970, *ApJ*, 160, 641
- Michaud, G., Charland, Y., Vauclair, S., & Vauclair, G. 1976, *ApJ*, 210, 447
- Michaud, G., Richer, J., & Vick, M. 2011, *A&A*, 534, A18
- Mihalas, D. 1978, *Stellar atmospheres /2nd edition/*

- Mikulášek, Z., Gráf, T., Krtička, J., Zverko, J., & Žižňovský, J. 2008a, *Contributions of the Astronomical Observatory Skalnaté Pleso*, 38, 363
- Mikulášek, Z., Krtička, J., Henry, G. W., et al. 2011, *A&A*, 534, L5
- Mikulášek, Z., Krtička, J., Henry, G. W., et al. 2008b, *A&A*, 485, 585
- Mikulášek, Z., Žižňovský, J., Zverko, J., & Polosukhina, N. S. 2003, *Contributions of the Astronomical Observatory Skalnaté Pleso*, 33, 29
- Minnaert, M. 1935, *ZAp*, 10, 40
- Molnar, M. R. 1972, *ApJ*, 175, 453
- Molnar, M. R. 1973, *ApJ*, 179, 527
- Mon, M., Hirata, R., & Sadakane, K. 1981, *PASJ*, 33, 413
- Monier, R., Gebran, M., & Royer, F. 2015, *A&A*, 577, A96
- Morgan, W. W. 1933, *ApJ*, 77, 330
- Morgan, W. W., Keenan, P. C., & Kellman, E. 1943, *An atlas of stellar spectra, with an outline of spectral classification*
- Moss, D. 2001, in *Astronomical Society of the Pacific Conference Series*, Vol. 248, *Magnetic Fields Across the Hertzsprung-Russell Diagram*, ed. G. Mathys, S. K. Solanki, & D. T. Wickramasinghe, 305
- Murphy, R. E. 1969, *AJ*, 74, 1082
- Musielok, B., Lange, D., Schoneich, W., et al. 1980, *Astronomische Nachrichten*, 301, 71
- Nahar, S. N. 1996, *Phys. Rev. A*, 53, 1545
- Nahar, S. N. 1997, *Phys. Rev. A*, 55, 1980
- Nakajima, R. 1985, *Ap&SS*, 116, 285
- Narayan, R. & Nityananda, R. 1986, *ARA&A*, 24, 127
- Ndiaye, M. L., LeBlanc, F., & Khalack, V. 2018, *MNRAS*, 477, 3390
- Neiner, C., Wade, G. A., & Sikora, J. 2017, *MNRAS*, 468, L46
- Nesvacil, N., Shulyak, D., Ryabchikova, T. A., et al. 2013, *A&A*, 552, A28
- Netopil, M., Fossati, L., Paunzen, E., et al. 2014, *MNRAS*, 442, 3761
- North, P. 1993, in *Astronomical Society of the Pacific Conference Series*, Vol. 44, *IAU Colloq. 138: Peculiar versus Normal Phenomena in A-type and Related Stars*, ed. M. M. Dworetzky, F. Castelli, & R. Faraggiana, 577
- Oksala, M. E., Kochukhov, O., Krtička, J., et al. 2015, *MNRAS*, 451, 2015
- Oksala, M. E., Wade, G. A., Townsend, R. H. D., et al. 2012, *MNRAS*, 419, 959

- Osawa, K. 1965, *Annals of the Tokyo Astronomical Observatory*, 9
- Osmer, P. S. & Peterson, D. M. 1974, *ApJ*, 187, 117
- Paunzen, E., Florian, J., Gütl-Wallner, A., et al. 2018, *Astronomische Nachrichten*, 339, 672
- Peterson, D. M. 1970, *ApJ*, 161, 685
- Petit, P., Lignières, F., Aurière, M., et al. 2011, *A&A*, 532, L13
- Piskunov, N. & Kochukhov, O. 2002, *A&A*, 381, 736
- Piskunov, N. E. 1990, *Mem. Soc. Astron. Italiana*, 61, 577
- Piskunov, N. E., Kupka, F., Ryabchikova, T. A., Weiss, W. W., & Jeffery, C. S. 1995, *A&AS*, 112, 525
- Piskunov, N. E. & Rice, J. B. 1993, *PASP*, 105, 1415
- Potter, A. T. & Tout, C. A. 2010, *MNRAS*, 402, 1072
- Pourbaix, D., Boffin, H. M. J., Chini, R., & Dembsky, T. 2013, *A&A*, 556, A45
- Preston, G. W. 1974, *ARA&A*, 12, 257
- Prvák, M., Krtička, J., & Korhonen, H. 2018, *Contributions of the Astronomical Observatory Skalnaté Pleso*, 48, 93
- Prvák, M., Liška, J., Krtička, J., Mikulášek, Z., & Lüftinger, T. 2015, *A&A*, 584, A17
- Pyper, D. M. 1969, *ApJS*, 18, 347
- Pyper, D. M., Ryabchikova, T., Malanushenko, V., et al. 1998, *A&A*, 339, 822
- Reindl, N., Bainbridge, M., Przybilla, N., et al. 2019, *MNRAS*, 482, L93
- Rice, J. B. 1970, *A&A*, 9, 189
- Rice, J. B., Wehlau, W. H., & Khokhlova, V. L. 1989, *A&A*, 208, 179
- Ricker, G. R., Winn, J. N., Vanderspek, R., et al. 2015, *Journal of Astronomical Telescopes, Instruments, and Systems*, 1, 014003
- Robrade, J. 2016, *Advances in Space Research*, 58, 727
- Robrade, J., Oskinova, L. M., Schmitt, J. H. M. M., Leto, P., & Trigilio, C. 2018, *A&A*, 619, A33
- Rusomarov, N., Kochukhov, O., Ryabchikova, T., & Ilyin, I. 2016, *A&A*, 588, A138
- Ryabchikova, T. A., Piskunov, N. E., Kupka, F., & Weiss, W. W. 1997, *Baltic Astronomy*, 6, 244
- Sargent, W. L. W. & Searle, L. 1966, *The Observatory*, 86, 27
- Sargent, W. L. W. & Searle, L. 1967, *ApJ*, 150, L33
- Sargent, W. L. W. & Strittmatter, P. A. 1966, *ApJ*, 145, 938
- Schaller, G., Schaerer, D., Meynet, G., & Maeder, A. 1992, *A&AS*, 96, 269

- Schmidt, G. D., Harris, H. C., Liebert, J., et al. 2003, *ApJ*, 595, 1101
- Schoeneich, W., Hildebrandt, G., Musielok, B., & Zelwanowa, E. 1976, *Astronomische Nachrichten*, 297, 173
- Schöller, M., Correia, S., Hubrig, S., & Ageorges, N. 2010, *A&A*, 522, A85
- Schwarzschild, M. 1958, *Structure and evolution of the stars*.
- Seggewiss, W. 1993, in *Astronomical Society of the Pacific Conference Series*, Vol. 44, IAU Colloq. 138: Peculiar versus Normal Phenomena in A-type and Related Stars, ed. M. M. Dworetsky, F. Castelli, & R. Faraggiana, 137
- Shulyak, D., Krtićka, J., Mikulášek, Z., Kochukhov, O., & Lüftinger, T. 2010, *A&A*, 524, A66
- Shulyak, D., Tsymbal, V., Ryabchikova, T., Stütz, C., & Weiss, W. W. 2004, *A&A*, 428, 993
- Silvester, J., Kochukhov, O., & Wade, G. A. 2014, *MNRAS*, 444, 1442
- Smith, K. C. 1996, *Ap&SS*, 237, 77
- Smith, M. A. & Groote, D. 2001, *A&A*, 372, 208
- Stibbs, D. W. N. 1950, *MNRAS*, 110, 395
- Stift, M. J., Leone, F., & Cowley, C. R. 2012, *MNRAS*, 419, 2912
- Struve, O. 1945, *Popular Astronomy*, 53, 271
- Struve, O. 1951, *Astrophysics: A topical symposium, commemorating the fiftieth anniversary of the Yerkes Observatory and a half century of progress in astrophysics*
- Taylor, R. J. 1987, *MNRAS*, 227, 553
- Tikhonov, A. N. 1963, *Dokl. Akad. Nauk SSSR*, 151, 501
- Titus, J. & Morgan, W. W. 1940, *ApJ*, 92, 256
- Tokovinin, A. 2008, *MNRAS*, 389, 925
- Tout, C. A., Wickramasinghe, D. T., & Ferrario, L. 2004, *MNRAS*, 355, L13
- Tout, C. A., Wickramasinghe, D. T., Liebert, J., Ferrario, L., & Pringle, J. E. 2008, *MNRAS*, 387, 897
- Townsend, R. H. D., Oksala, M. E., Cohen, D. H., Owocki, S. P., & ud-Doula, A. 2010, *ApJ*, 714, L318
- Townsend, R. H. D. & Owocki, S. P. 2005, *MNRAS*, 357, 251
- Ud-Doula, A., Owocki, S. P., & Townsend, R. H. D. 2009, *MNRAS*, 392, 1022
- Unglaub, K. & Bues, I. 2001, *A&A*, 374, 570
- van Hamme, W. 1993, *AJ*, 106, 2096
- Vauclair, S., Dolez, N., & Gough, D. O. 1991, *A&A*, 252, 618

- Venn, K. A. & Lambert, D. L. 1990, *ApJ*, 363, 234
- Vilhu, O., Tuominen, I. V., & Boyarchuk, A. A. 1976, in *IAU Colloq. 32: Physics of Ap Stars*, ed. W. W. Weiss, H. Jenkner, & H. J. Wood, 563
- Vogt, S. S., Penrod, G. D., & Hatzes, A. P. 1987, *ApJ*, 321, 496
- Walborn, N. R. 1973, *IAU Circ.*, 2612
- Werner, K., Dreizler, S., Heber, U., et al. 1995, *A&A*, 293
- Wolff, S. C. & Preston, G. W. 1978, *ApJS*, 37, 371
- Wolff, S. C. & Wolff, R. J. 1974, *ApJ*, 194, 65
- Woltjer, L. 1960, *ApJ*, 131, 227

This work includes data collected by the Kepler mission. Funding for the Kepler mission is provided by the NASA Science Mission Directorate.

Some of the data presented in this work were obtained from the Mikulski Archive for Space Telescopes (MAST). STScI is operated by the Association of Universities for Research in Astronomy, Inc., under NASA contract NAS5-26555. Support for MAST for non-HST data is provided by the NASA Office of Space Science via grant NNX13AC07G and by other grants and contracts.

This work has made use of the VALD database, operated at Uppsala University, the Institute of Astronomy RAS in Moscow, and the University of Vienna.

This work has made use of observations obtained at European Southern Observatory (ESO programs 087.D-0099 and 089.D-0153), and at the South African Astronomical Observatory (SAAO).

List of publications

Refereed papers

- Prvák, M., Liška, J., Krtička, J., Mikulášek, Z., Lüftinger, T., *Modelling of variability of the chemically peculiar star φ Draconis*, 2015, A&A, 584, A17
MP computed the light curves of φ Dra and wrote the manuscript.
- Reindl, N., Bainbridge, M., Przybilla, N., Geier, S., Prvák, M., Krtička, J., Østensen, R. H., Telting, J., Werner, K., *Unravelling the baffling mystery of the ultrahot wind phenomenon in white dwarfs*, 2019, MNRAS, 482, L93
MP computed the possible distribution of light intensity in the white dwarf GALEX J014636+323615 and contributed to preparation of the manuscript and discussion of the results.
- Oksala, M. E., Kochukhov, O., Krtička, J., Townsend, R. H. D., Wade, G. A., Prvák, M., Mikulášek, Z., Silvester, J., Owocki, S. P., *Revisiting the rigidly rotating magnetosphere model for σ Ori E - II. Magnetic Doppler imaging, arbitrary field RRM, and light variability*, 2015, MNRAS, 451, 2015
MP processed IUE spectra and calculated UV light curve of σ Ori E and contributed to preparation of the manuscript and discussion of the results.
- Krtička, J., Janík, J., Marková, H., Mikulášek, Z., Zverko, J., Prvák, M., Skarka, M., *Ultraviolet and visual flux and line variations of one of the least variable Bp stars HD 64740*, 2013, A&A, 556, A18
MP derived UV light curve of HD 64730 from IUE spectra and contributed to preparation of the manuscript and discussion of the results.
- Krtička, J., Mikulášek, Z., Henry, G. W., Janík, J., Kochukhov, O., Pigulski, A., Leto, P., Trigilio, C., Krtíčková, I., Lüftinger, T., Prvák, M., Tichý, A., *HST/STIS analysis of the first main sequence pulsar CU Vir*, 2019, A&A, 625, A34
MP processed IUE spectra and contributed to preparation of the manuscript and discussion of the results.
- Janík, J., Krtička, J., Mikulášek, Z., Zverko, J., Pintado, O., Paunzen, E., Prvák, M., Skalický, J., Zejda, M., Adam, C., *A Binary Nature of the Marginal CP Star Sigma Sculptoris*, 2018, PASP, 130, 054203
MP participated in spectroscopic observations at La Silla, Chile and contributed to preparation of the manuscript and discussion of the results.

Conference proceedings

- Prvák, M., Krtička, J., Mikulášek, Z., Lüftinger, T., Liška, J., *Modelling the variability of the CP star φ Dra*, 2014, Putting A Stars into Context: Evolution, Environment, and Related Stars, 214
MP modeled the variability of φ Dra and prepared the conference poster.
- Prvák, M., Krtička, J., Korhonen, H., *The millimagnitude variability of the HgMn star φ Phe*, 2018, Contributions of the Astronomical Observatory Skalnaté Pleso, 48, 93
MP calculated theoretical light curves of φ Phe and presented a talk at the conference.
- Krtička, J., Huang, L., Lüftinger, T., Mikulášek, Z., Niemczura, E., Prvák, M., Silvester, J., Wade, G., Zverko, J., *Testing Opacities Using the SED Variability of Chemically Peculiar Stars*, 2018, Workshop on Astrophysical Opacities, 515, 195
MP processed the IUE spectra of a Cen and contributed to preparation of the manuscript and discussion of the results.
- Krtička, J., Huang, L., Jagelka, M., Lüftinger, T., Mikulášek, Z., Niemczura, E., Prvák, M., Silvester, J., Wade, G., *The nature of light variations in magnetic hot stars*, 2018, Contributions of the Astronomical Observatory Skalnaté Pleso, 48, 170
MP processed the IUE spectra of a Cen and contributed to preparation of the manuscript and discussion of the results.
- Kurfürst, P., Prvák, M., Krtička, J., Zejda, M., *Research of Hot Stars at Masaryk University*, 2017, Central European Astrophysical Bulletin, 41, 39
MP provided a plot of the SED and emergent flux maps of φ Dra and contributed to preparation of the manuscript and discussion of the results.
- Oksala, M. E., Kochukhov, O., Krtička, J., Prvák, M., Mikulášek, Z., *Unraveling the variability of σ Ori E*, 2015, New Windows on Massive Stars, 307, 348
MP provided UV light curves of σ Ori E and contributed to preparation of the manuscript and discussion of the results.
- Krtička, J., Mikulášek, Z., Zverko, J., Prvák, M., *The origin of light variability in Ap stars*, 2014, Putting A Stars into Context: Evolution, Environment, and Related Stars, 205
MP contributed to preparation of the manuscript and discussion of the results.

Appendix A

List of spectra used for abundance mapping of V824 Cen

File ID	Phase	Instrument	Observation Time	MJD	Exposure [s]
01	0.894488	FEROS	2011-08-01 23:49:04	55774.9924	300
02	0.917135	FEROS	2011-08-02 00:30:29	55775.0212	300
03	0.957474	FEROS	2011-08-02 01:44:20	55775.0725	300
04	0.966832	FEROS	2011-08-02 02:01:34	55775.0844	300
05	0.988692	FEROS	2011-08-02 02:41:37	55775.1122	300
06	0.682643	FEROS	2011-08-02 23:52:23	55775.9947	300
07	0.724005	FEROS	2011-08-03 01:08:10	55776.0473	300
08	0.734149	FEROS	2011-08-03 01:26:42	55776.0602	300
09	0.755931	FEROS	2011-08-03 02:06:31	55776.0879	300
10	0.782745	FEROS	2011-08-03 02:55:41	55776.1220	300
11	0.480391	FEROS	2011-08-04 00:13:18	55777.0092	600
12	0.513968	FEROS	2011-08-04 01:14:41	55777.0519	600
13	0.547860	FEROS	2011-08-04 02:16:44	55777.0950	600
14	0.231667	FEROS	2011-08-04 23:09:06	55777.9646	600
15	0.258009	FEROS	2011-08-04 23:57:18	55777.9981	600
16	0.291115	FEROS	2011-08-05 00:57:54	55778.0402	600
17	0.324141	FEROS	2011-08-05 01:58:23	55778.0822	600
18	0.337981	FEROS	2011-08-05 02:23:45	55778.0998	600
19	0.058431	FEROS	2011-08-06 00:23:05	55779.0160	600
20	0.085010	FEROS	2011-08-06 01:11:45	55779.0498	600
21	0.118272	FEROS	2011-08-06 02:12:41	55779.0921	600
22	0.145087	FEROS	2011-08-06 03:01:40	55779.1262	600
23	0.923630	FEROS	2012-08-14 23:56:08	56153.9973	600
24	0.936132	FEROS	2012-08-15 00:18:58	56154.0132	600
25	0.947613	FEROS	2012-08-15 00:40:05	56154.0278	600
26	0.965542	FEROS	2012-08-15 01:12:54	56154.0506	600
27	0.982841	FEROS	2012-08-15 01:44:34	56154.0726	600
28	0.113208	FEROS	2012-08-19 01:17:06	56158.0535	600
100	0.636360	GIRAFFE	2011-08-20 17:45:09	55793.7397	1199
101	0.655311	GIRAFFE	2011-08-20 18:19:53	55793.7638	1200
102	0.397944	GIRAFFE	2013-03-21 01:29:06	56372.0619	1200

File ID	Phase	Instrument	Observation Time	MJD	Exposure [s]
103	0.434195	GIRAFFE	2013-03-21 02:35:32	56372.1080	2400
104	0.410054	GIRAFFE	2013-03-21 01:51:23	56372.0773	2400
105	0.461324	GIRAFFE	2013-03-21 03:25:11	56372.1425	1199
106	0.039289	GIRAFFE	2013-03-21 21:03:38	56372.8775	2399
107	0.063115	GIRAFFE	2013-03-21 21:47:15	56372.9078	2400
108	0.646738	GIRAFFE	2013-03-23 22:07:19	56374.9217	1999
109	0.666475	GIRAFFE	2013-03-23 22:43:25	56374.9468	2000
110	0.686763	GIRAFFE	2013-03-23 23:20:33	56374.9726	2000
111	0.708545	GIRAFFE	2013-03-24 00:00:22	56375.0003	1999
112	0.728203	GIRAFFE	2013-03-24 00:36:30	56375.0253	2000
113	0.747941	GIRAFFE	2013-03-24 01:12:34	56375.0504	1738
114	0.388027	GIRAFFE	2013-03-24 20:44:47	56375.8644	2000
115	0.407764	GIRAFFE	2013-03-24 21:20:49	56375.8895	2000
116	0.791101	GIRAFFE	2013-03-27 22:05:24	56378.9204	1999
117	0.810681	GIRAFFE	2013-03-27 22:41:17	56378.9453	2000
118	0.830654	GIRAFFE	2013-03-27 23:17:47	56378.9707	2000
119	0.850313	GIRAFFE	2013-03-27 23:53:48	56378.9957	2000
120	0.925331	GIRAFFE	2013-03-28 02:11:09	56379.0911	1999
121	0.944989	GIRAFFE	2013-03-28 02:47:13	56379.1161	1501
122	0.527908	GIRAFFE	2013-03-28 20:34:39	56379.8574	1999
123	0.621876	GIRAFFE	2013-03-28 23:26:48	56379.9769	1952

